

DEVELOPMENT OF ATMOSPHERIC INFRARED EMISSION MODELS

**J.W. Duff
J.H. Gruninger
R.L. Sundberg
P.K. Acharya**

**S. M. Adler-Golden
A. Berk
L. S. Bernstein
D. C. Robertson**

**Spectral Sciences, Inc.
99 South Bedford Street, #7
Burlington, MA 01803-5169**

19 December 1997

**Final Technical Report
April 1991 - October 1997**


19980603 023

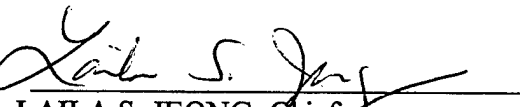
Approved for Public Release; Distribution Unlimited.

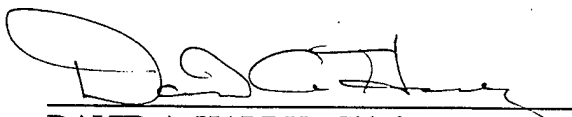


**AIR FORCE RESEARCH LABORATORY
Space Vehicles Directorate
AIR FORCE MATERIEL COMMAND
HANSCOM AFB, MA 01731-3010**

"This technical report has been reviewed and is approved for publication."


DEAN F. KIMBALL
Contract Manager
Background Clutter Mitigation Branch
Battlespace Environment Division


LAILA S. JEONG, Chief
Background Clutter Mitigation Branch
Battlespace Environment Division


DAVID A. HARDY, Chief
Battlespace Environment Division

This report has been reviewed by the ESC Public Affairs Office (PA) and is releasable to the National Technical Information Service (NTIS).

Qualified requestors may obtain additional copies from the Defense Technical Information Center (DTIC).

If your address has changed, if you wish to be removed from the mailing list, or if the addressee is no longer employed by your organization, please notify AFRL/VSOS-IM, 29 Randolph Road, Hanscom AFB, MA 01731-3010. This will assist us in maintaining a current mailing list.

Do not return copies of this report unless contractual obligations or notices on a specific document require that it be returned.

REPORT DOCUMENTATION PAGE

Form Approved
OMB No. 0704-0188

Public reporting burden for this collection of information is estimated to average 1 hour per response, including the time for reviewing instructions, searching existing data sources, gathering and maintaining the data needed, and completing and reviewing the collection of information. Send comments regarding this burden estimate or any other aspect of this collection of information, including suggestions for reducing this burden, to Washington Headquarters Services, Directorate for Information Operations and Reports, 1215 Jefferson Davis Highway, Suite 1204, Arlington, VA 22202-4302, and to the Office of Management and Budget, Paperwork Reduction Project (0704-0188), Washington, DC 20503.

1. AGENCY USE ONLY (Leave Blank)		2. REPORT DATE December 19, 1997	3. REPORT TYPE AND DATES COVERED Final Technical Report April 1991 - October 1997
4. TITLE AND SUBTITLE Development of Atmospheric Infrared Emission Models			5. FUNDING NUMBERS C - F19628-91-C-0083 PE - 63215C PR - S321 TA - 13 W - AA
6. AUTHOR(S) J.W. Duff, J. Gruninger, R.L. Sundberg, P.K. Acharya, S.M. Adler-Golden, A. Berk, L.S. Bernstein, and D.C. Robertson			
7. PERFORMING ORGANIZATION NAME(S) AND ADDRESS(ES) Spectral Sciences, Inc. 99 South Bedford Street, #7 Burlington, MA 01803-5169			8. PERFORMING ORGANIZATION REPORT NUMBER SSI-TR-304
9. SPONSORING/MONITORING AGENCY NAME(S) AND ADDRESS(ES) Air Force Research Laboratory 29 Randolph Road Hanscom AFB, MA 01731-3010 Contract Manager: Dean Kimball/VSBM			10. SPONSORING/MONITORING AGENCY REPORT NUMBER AFRL-VS-HA-TR-98-0002
11. SUPPLEMENTARY NOTES			
12a. DISTRIBUTION/AVAILABILITY STATEMENT Approved for public release; distribution unlimited.			12b. DISTRIBUTION CODE
13. ABSTRACT (Maximum 200 words) This report describes the development of atmospheric infrared (IR) radiance models to describe atmospheric NLTE radiation and structure in the IR spectral region for arbitrary diurnal conditions. Several of the models have been included into the suite of standard Air Force atmospheric radiation computer models. These models calculate the radiation from quiescent, auroral, and structured atmospheres in the 2-40 μm spectral region for arbitrary paths above 30 km under nighttime, terminator, and daytime conditions. In addition, a radiance model based on SHARC and MODTRAN has been developed which allows arbitrary viewing geometries from the ground to 300 km. In conjunction with the research into atmospheric radiance models, an atmospheric generator which uses empirical models to generate atmospheric profiles for the solar terminator and other systematic atmospheric variations has been developed. If further support of the atmospheric radiance model program, a detailed chemical kinetic model has been developed to describe O_3 emission in the mesosphere resulting from high-lying vibrational states. The predicted O_3 spectral radiances are in good agreement with the SPIRIT-1 and CIRRIS-1A data sets.			
14. SUBJECT TERMS Infrared Radiation Thermosphere Mesosphere Atmospheric Structure Atmospheric Radiance Terminator			15. NUMBER OF PAGES 80
			16. PRICE CODE
17. SECURITY CLASSIFICATION OF REPORT UNCLASSIFIED	18. SECURITY CLASSIFICATION OF THIS PAGE UNCLASSIFIED	19. SECURITY CLASSIFICATION OF ABSTRACT UNCLASSIFIED	20. LIMITATION OF ABSTRACT SAR

TABLE OF CONTENTS

1. INTRODUCTION	1
2. OVERVIEW OF SHARC	1
2.1 Quiescent Chemical Kinetics	3
2.2 Radiative Excitation from Atmospheric Layers	4
2.3 Auroral Chemical Kinetics	6
2.4 Line-of-Sight Spectral Radiance Model	7
2.4.1 Calculation for a Single Line	7
2.4.2 Illustrative Calculations	9
2.5 Data Comparisons	11
3. DEVELOPMENT OF AN INTERACTIVE ATMOSPHERE GENERATOR MODEL ...	13
3.1 Profile Computations	14
3.1.1 CO ₂	15
3.1.2 NO	16
3.1.3 O Atoms	17
3.1.4 O ₃	18
3.1.5 OH	20
3.1.6 H Atoms	20
3.1.7 CO and CH ₄	20
3.1.8 H ₂ O	20
3.1.9 Additional Species for SAMM	21
3.2 Temperature	21
4. DEVELOPMENT OF A TERMINATOR MODEL	21
4.1 Calculation Methods	22
4.2 Results and Comparisons	22
4.2.1 CO ₂ 4.3 μ m	22
4.2.1.1 CO ₂ Vibrational Temperatures	23
4.2.1.2 Radiance Profiles	23
4.2.2 O ₃ 9.6 μ m	24
4.2.2.1 An Improved O ₃ Chemical Kinetics Model	24
4.2.2.2 Overview of Ozone Models	24
4.2.2.3 SHARC-3 O ₃ Model Description	26
4.2.2.4 Terminator O ₃ Radiance	30
4.2.3 OH $\Delta V=1$	31
4.2.3.1 Terminator OH Radiance	31
5. DEVELOPMENT OF SAMM	32
5.1 Overview	32
5.1.1 Refractive Geometry	33
5.1.2 Column Densities	33
5.1.3 Radiative Transfer Model	34
5.2 Radiation Transport Algorithm	34
5.2.1 Line-of-Sight Radiance	34

TABLE OF CONTENTS (Continued)

5.3 Low Altitude Solar Attenuation	37
5.4 Representative Calculations	37
6. DEVELOPMENT OF AN ATMOSPHERIC STOCHASTIC STRUCTURE MODEL	39
6.1 Stochastic Structure Overview	40
6.2 Radiance Structure Calculation Technique	41
6.2.1 Vibrational State Temperature Fluctuations	42
6.2.2 Radiance Covariance	46
6.2.3 Image Synthesis	51
6.3 Limb and Nadir Radiance	51
6.4 Radiance Structure Statistics	55
6.4.1 Effects of Latitudinal and Diurnal Variations	55
6.4.1.1 Above the Horizon (ATH) Limb Viewing	55
6.4.1.2 Below the Horizon (BTH) Nadir Viewing	59
6.4.2 Variation of Temperature Statistical Parameters for ATH Limb Viewing	63
7. SUMMARY	64
8. ACKNOWLEDGEMENTS	65
9. REFERENCES	65

LIST OF FIGURES

1. Calculational Sequence for SHARC-4	2
2. Vibrational Temperature Profiles for Selected CO ₂ States	5
3. Prediction of the N ₂ (v) Production Efficiency for Several Mechanisms	7
4. Comparison of SHARC and FASCOD3 Calculations of CO ₂ Radiance for a 50 km Limb View	10
5. Comparison of SHARC Calculation (Top) and Observation (Bottom) of Quiescent Nighttime Emission in a Near-Limb View from an Altitude of 78 km	11
6. Comparison of SHARC Radiance Profile with SPIRE Data under Daytime and Nighttime Conditions	12
7. Calculated and Observed NO Spectrum for a 90 km Zenith View During a Class II Aurora	13
8. Comparison of Observed (Aladdin Mass Spectrometer), Calculated, ⁴⁰ and SAG Model CO ₂ /Ar Density Ratios	15

LIST OF FIGURES (Continued)

9. CO ₂ Concentration Profiles for Autumn, Mid-Latitude, Moderate-Activity Conditions . . .	16
10. Diurnal Dependence of NO Densities for Autumn, Moderate-Activity Conditions	17
11. Comparison of SAG Model and NRL Climatology Ozone Concentrations for Fall Equinox, 45° N, Moderate-Activity Conditions	19
12. Time-Dependence of Ozone Concentrations at the Dusk Terminator for Fall Equinox, 45° N, Moderate-Activity Conditions	19
13. Solar-Angle Dependence of the CO ₂ (00011) State Vibrational Temperature	23
14. SHARC Calculations of 80 km Limb Radiance From Ozone Using the SHARC Daytime "U.S. Standard" Model Atmosphere	25
15. Predicted and Observed (SPIRIT-1) Nighttime Cold Band (1000-1087 cm ⁻¹) and Hot Band (930-976 cm ⁻¹) Limb Radiance Profiles. Input Atmosphere is from the SHARC Atmosphere Generator	29
16. Calculated (SHARC-3) and Observed (CIRRIS-1A) O ₃ (v ₃) Limb Radiances at the Dusk Terminator	30
17. Calculated (SHARC-3) and Observed (CIRRIS-1A) OH(ΔV=1) Limb Radiances at the Dusk Terminator	31
18. Comparison of SAMM with SHARC-3 for an 80 km Limb Path at Night	38
19. Comparison of SAMM with MODTRAN for a 10 km Limb Path	39
20. Altitude Profile of the Atmospheric Kinetic Temperature and Vibrational Temperatures of Selected States of CO ₂ for Nighttime Conditions	43
21. Partial Derivatives of Vibrational Temperature with Respect to Kinetic Temperature as a Function of Altitude for Selected States of CO ₂ for Nighttime Conditions	44
22. Altitude Dependence of the Temperature Horizontal Correlation Length for the NSS Stochastic Model	44
23. Altitude Dependence of the Temperature Vertical Correlation Length for the NSS Stochastic Model	45
24. Altitude Dependence of the Temperature Relative Standard Deviation for the NSS Stochastic Model	45
25. Schematic of Sensor Image Plane, Optics, and Two LOS Extending into the Atmosphere .	47

LIST OF FIGURES (Continued)

26. Effect of Latitude on the Altitude Dependence of the Variance Distribution Function for a 100 km Limb Under Nighttime Conditions in the MWIR Spectral Region	50
27. Diurnal Variation of the Altitude Dependence of the Variance Distribution Function for a 60 km Limb Under Nighttime Conditions in the SWIR Spectral Region	50
28. Diurnal Variation of the Altitude Dependence of MWIR Radiance for Subarctic and Equatorial Latitudes	52
29. Diurnal Variation of the Altitude Dependence of the SWIR Radiance for Subarctic and Equatorial Latitudes	53
30. Diurnal Variation of the Viewing Angle Dependence of the CO ₂ MWIR μ m Band Radiance for Subarctic and Equatorial Latitudes	53
31. Diurnal Variation of the Viewing Angle Dependence of the SWIR Radiance for Subarctic and Equatorial Latitudes	54
32. Comparison of the HIRS/2 Latitude Dependent Data with SHARC Calculations for NADIR Viewing	55
33. Diurnal Variation of the Altitude Dependence of the Horizontal Correlation Length for Subarctic and Equatorial Latitudes in the MWIR Spectral Region	56
34. Diurnal Variation of the Altitude Dependence of the Vertical Correlation Length for Subarctic and Equatorial Latitudes in the MWIR Spectral Region	57
35. Diurnal Variation of the Altitude Dependence of the Relative Standard Deviation for Subarctic and Equatorial Latitudes in the MWIR Spectral Region	57
36. Diurnal Variation of the Altitude Dependence of the Horizontal Correlation Length for Subarctic and Equatorial Latitudes in the SWIR Spectral Region	58
37. Diurnal Variation of the Altitude Dependence of the Vertical Correlation Length for Subarctic and Equatorial Latitudes in the SWIR Spectral Region	58
38. Diurnal Variation of the Altitude Dependence of the Relative Standard Deviation for Subarctic and Equatorial Latitudes in the SWIR Spectral Region	59
39. Diurnal Variation of the Viewing Angle Dependence of the Vertical Correlation Length for Subarctic and Equatorial Latitudes in the MWIR Spectral Region	60
40. Diurnal Variation of the Viewing Angle Dependence of the Horizontal Correlation Length for Subarctic and Equatorial Latitudes in the MWIR Spectral Region	60

LIST OF FIGURES (Continued)

41. Diurnal Variation of the Viewing Angle Dependence of the Relative Standard Deviation for Subarctic and Equatorial Latitudes in the MWIR Spectral Region 61
42. Diurnal Variation of the Viewing Angle Dependence of the Horizontal Correlation Length for Subarctic and Equatorial Latitudes in the SWIR Spectral Region 61
43. Diurnal Variation of the Viewing Angle Dependence of the Vertical Correlation Length for Subarctic and Equatorial Latitudes in the SWIR Spectral Region 62
44. Diurnal Variation of the Viewing Angle Dependence of the Relative Standard Deviation for Subarctic and Equatorial Latitudes in the SWIR Spectral Region 62

1. INTRODUCTION

The calculation of infrared (IR) radiance and transmittance spectra is an important ingredient in many areas of atmospheric science. These include modeling the atmospheric energy budget for global climate change predictions, analyzing data from remote sounding experiments, and understanding molecular excitation and production processes. Typically, a large number of calculations are required that span an extensive spectral/spatial domain. For the upper atmosphere, non-local thermodynamic equilibrium (non-LTE) effects must also be treated.

Available computer codes for atmospheric IR radiation that have gained wide use include several developed and maintained by the US Air Force. LOWTRAN¹ and MODTRAN² are rapid, LTE codes for low- to moderate-resolution spectra. FASCODE³ is a high-resolution, line-by-line code that can be used in both LTE and non-LTE applications; however, the non-LTE molecular state populations must be externally generated. Until recently, a rapid and unified standard code for first-principles calculations of non-LTE atmospheric background radiation has been lacking.

SHARC, the Strategic High-altitude Atmospheric Radiation Code,^{4,7} calculates emission and transmittance spectra in the 2-40 μm region for arbitrary line-of-sight (LOS) paths between 50 and 300 km with sufficient accuracy, speed, and resolution (0.5 cm^{-1}) to be useful for a wide range of applications. It incorporates the IR bands of NO, CO₂, O₃, H₂O, OH, CO, and CH₄ found in the quiescent atmosphere, including minor isotopic bands of CO₂ and H₂O. It also accounts for auroral production and excitation of CO₂, NO, and NO⁺ caused by the flux of energetic solar electrons.

To account for non-LTE effects, molecular vibrational state populations are calculated from first principles. As in other non-LTE atmospheric models (e.g., Wintersteiner et al.,⁸ Lopez-Puertas et al.^{9,10}), steady-state kinetics are assumed for the quiescent atmospheric processes of collisional excitation, de-excitation, energy transfer, radiative decay, illumination by the sun, earth and atmosphere, and chemical production. In SHARC, additional production and excitation mechanisms resulting from electron deposition are included using a time-dependent kinetic model. Rotation-translation equilibrium is assumed.

This final report describes the development of high-altitude infrared (IR) radiance models which are presented in Sections 2-6. Section 2 presents an overview of the basic structure and functionality of SHARC with brief comparison to data. Section 3 describes the atmospheric generator model, which was developed to provide atmospheric properties required to model radiance in the terminator region as illustrated in Section 4. Section 5 discusses the merging of SHARC with MODTRAN to extend the LOS radiance capability to the ground. Next, a model for atmospheric stochastic structure is derived and applied to assess atmospheric structure in the 2.7 μm and 4.3 μm spectral regions in Section 6. Finally, Section 7 gives a summary of the work performed under this contract.

2. OVERVIEW OF SHARC

The schematic in Figure 1 illustrates SHARC's module structure and overall calculational sequence. The input module queries the user for parameters needed to define the calculation. Atmospheric temperature and species density profiles are specified via an external file. Profiles are required for the IR-active species (NO, CO₂, H₂O, O₃, CO, OH, and CH₄), the major atmospheric species to which they are collisionally coupled (N₂, O₂, O), and atomic hydrogen, whose reaction

with O_3 provides the main source of $OH(v)$. Other input parameters include the LOS specifications and, if desired, the coordinates of a localized auroral region through which the LOS may pass.

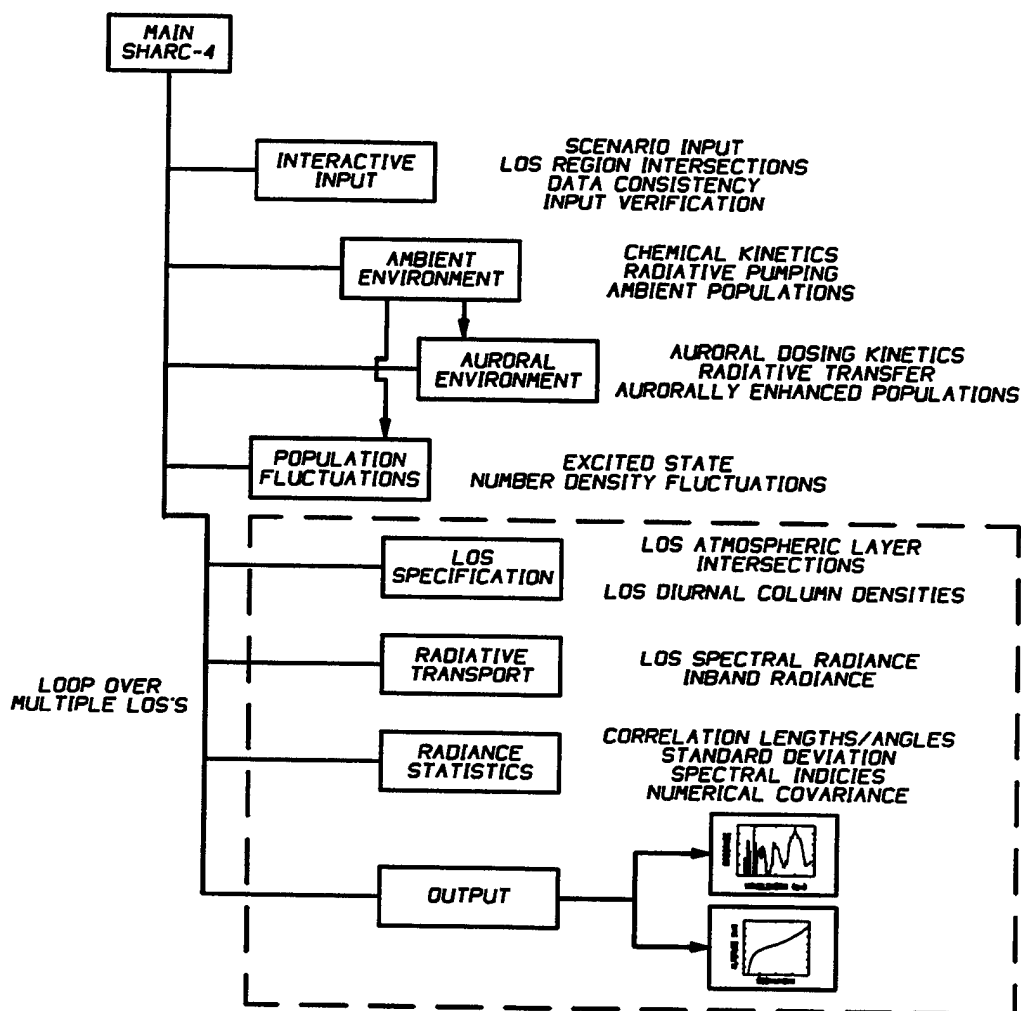


Figure 1. Calculational Sequence for SHARC-4.

Excited vibrational state populations are calculated in the chemical kinetics and radiative transfer modules and are saved in an output file for later use. For the quiescent atmosphere, steady-state conditions are assumed. If auroral excitation is specified, a time-dependent chemical model calculates the additional production of NO and NO^+ arising from interactions of auroral electrons. To generate the desired LOS spectrum, the vibrational state populations are fed to the spectral radiance module, which outputs radiance and transmittance spectra and in-band intensities.

Condensed descriptions of the chemical kinetics and radiation transport calculations are given below. Detailed descriptions of SHARC may be found in several technical reports.^{4-6,11} Code upgrades performed during this contract, which include provisions for LOS's through multiple distinct atmospheric regions for use in modeling terminator and atmospheric structure, are discussed in detail in Sections 5 and 6.

2.1 Quiescent Chemical Kinetics

The quiescent chemical kinetics are handled primarily through separate reaction sets for each IR-active molecule; the reaction sets can be solved selectively for the specific molecules under investigation. The reaction database files contain the list of vibrational states for each molecule, the chemical equations written in symbolic form, and the rate constant expressions. The equations include chemical formation of excited vibrational states, collisional deactivation and excitation (satisfying detailed balance), spontaneous emission, and the radiative excitation processes associated with absorption of radiation from the sun and from the atmosphere. The atmosphere is assumed to be horizontally uniform and is divided into altitude layers that are typically 2 km to 10 km in height.

The reaction files are read and the time-dependent differential rate equations are set up using a technique based on the Sandia CHEMKIN general-purpose chemical kinetics code.¹² Each quiescent vibrational state number density $[M^*]$ in each atmospheric layer is obtained from the solution to the steady-state equation

$$\frac{d[M^*]}{dt} = 0 = -A[M^*] + \sum_k S_k - \sum_k Q_k[M^*] + r_s + r_e + r_a \quad (1)$$

where A is the total spontaneous emission rate, the S_k are the source terms for production by collisional processes, and the Q_k are the collisional quenching rates. The production rates due to radiation from the sun, earth (i.e., from below the 50 km altitude boundary), and atmosphere (above 50 km), r_s , r_e , and r_a , respectively, implicitly depend on the densities of the lower-energy states of species M . Eq. (1) is solved for $[M^*]$ with the constraint that the total number density for the molecule equals that specified in the atmosphere input file.

While most of the excitation and de-excitation processes involve only a single vibrationally excited molecule, leading to uncoupled, linear equations, the species $\text{CO}_2(v)$, $\text{H}_2\text{O}(v)$ and $\text{OH}(v)$ are indirectly coupled to each other via resonant energy transfer processes involving $\text{N}_2(v=1)$, as discussed by Kumer and co-workers.¹³⁻¹⁵ The steady-state equations for these species are linearized by equating the ground vibrational state number densities with the total number densities, and are solved for the $\text{N}_2(v=1)$ population. The result is then inserted into the uncoupled Eq. (1) from which refined excited state populations are calculated. For energy transfer processes involving $\text{O}_2(v=1)$,¹⁰ O_2 is assumed to remain in LTE.

The collisional rate constants were obtained from the recent literature and from Taylor's review¹⁶ of measurements prior to 1974. The solar excitation rates k_s are derived from transmittance calculations using either MODTRAN² or the LOS radiance model discussed in Subsection 2.5. The earthshine rates k_e are expressed in terms of an effective blackbody temperature corresponding to the altitude where the vibrational band becomes optically thick in a nadir view.

The calculation of the excitation rate r_a due to atmospheric emission originating within the 50-300 km altitude range is considerably more complicated than for r_s and r_e , and briefly described below.

2.2 Radiative Excitation from Atmospheric Layers

The effect of the atmospheric excitation term r_a is to enhance the excited state number density within each atmospheric layer by an amount

$$\frac{r_a}{A+q} = [M^*] - [M^*]_o \quad (2)$$

Here q is the total quenching rate and $[M^*]_o$ is the steady-state solution with r_a set to zero, as obtained from an initial steady-state calculation. Re-excitation due to transfer from $N_2(v=1)$ is incorporated as a reduction in q rather than as a separate source term in Eq. (1).

The excited-state enhancement, and hence r_a , may be evaluated following the treatment of Kumer and co-workers.^{13,14} For a given vibrational band and atmospheric layer i we may write

$$[M_i^*] = [M_i^*]_o + \alpha_i \omega_i \sum_j P_{ji} \omega_j [M_j^*] \quad (3)$$

where α_i is the probability for absorption of a photon entering the layer, P_{ji} is the probability that a photon emitted from layer j will be absorbed in layer i , and ω_i is the branching ratio for re-emission,

$$\omega_i = \frac{A^*}{A+q_i} \quad (4)$$

where A^* is the Einstein coefficient for emission in the given band.

For a calculated probability matrix (P) and set of α_i , the set of Eq. (3) for all layers may be solved simultaneously. A physically instructive solution is provided by repeated substitution into Eq. (3) of the corresponding equation for the layers j . After collecting factors the result is the infinite series

$$[M_i^*] = [M_i^*]_o + \alpha_i \omega_i \sum_j (P_{ji}^{(1)} + P_{ji}^{(2)} + \dots) \omega_j [M_j^*]_o \quad (5)$$

Here, the $(P)^{(k)}$ matrices represent probabilities for k -th order photon scattering; $(P)^{(1)} = (P)$. Except in the case of the $CO_2(v_3)$ band, which is strongly trapped, the series converges in a small number of terms.

Both (P) and the α_i depend on the lower vibrational state populations. Therefore, the overall solution proceeds in stages for successively higher-energy states. The ground state populations $[M_i]$ and the initial excited state populations $[M_i^*]_o$ for transitions to the ground state are calculated assuming $r_a=0$. The results are then used to evaluate (P) and α_i and to compute the radiative excitation rates r_a for those transitions. The steady-state equations are then solved again including

r_a to generate the corresponding populations for the next set of vibrational transitions. This sequence is repeated until solutions for the highest-energy states are obtained. The major calculational effort is in computing the elements of the layer-layer excitation probability matrix (P). This involves a multidimensional integral over the location, direction, vibration-rotation line, frequency location within the line, and propagation distance of the radiation. The integral is evaluated with the aid of Monte Carlo sampling using trial "photons". The calculation assumes semi-infinite plane-parallel geometry and uses the exact temperature- and pressure-dependent Voigt lineshape.

Sample results for vibrational states excited by both atmospheric and solar radiation appear in Figure 2, which displays vibrational temperatures for selected states of CO₂ at a solar zenith angle of 82°. The states are labeled using the HITRAN convention;¹⁷ only the main isotopes are shown. This calculation was performed to simulate emissions observed near the dawn terminator during the SPIRE rocket experiment.¹⁸ The species number density and temperature profiles were obtained using the MSISE-90 model¹⁹ and an altitude-dependent CO₂ mixing ratio representative of rocket and satellite observations.^{8,20} Up to 10,000 Monte Carlo "photons" per band were used in the NEMESIS runs, which was sufficient to essentially converge the vibrational temperatures.

As seen in Figure 2, the ν_3 -excited states (00011), (01111), and (10011) depart from LTE around 60-70 km altitude. Very similar vibrational temperatures have been reported by Wintersteiner et al.^{21,22} using the "RAD" algorithm. The (01101) (ν_2) state has been treated theoretically in recent studies by Lopez-Puertas et al.²³ and Wintersteiner et al.⁸ The SHARC calculation for Figure 2 used the value $3 \times 10^{-13} / T \text{ cm}^3/\text{s}$ for the rate constant for collisional excitation of (01101) by O atoms, consistent with those studies, and consequently generates a similar vibrational temperature profile which remains close to LTE up to 100 km.

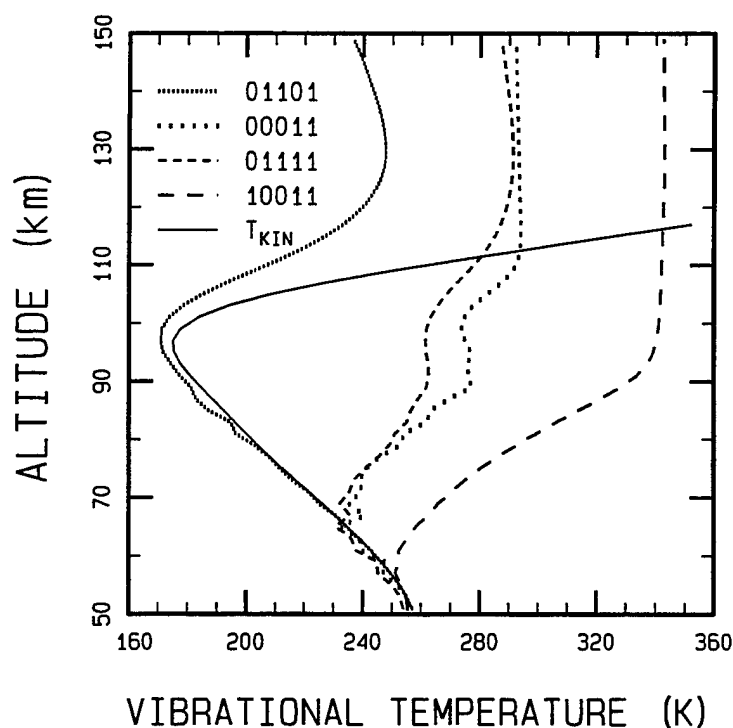


Figure 2. Vibrational Temperature Profiles for Selected CO₂ States.

2.3 Auroral Chemical Kinetics

The SHARC auroral kinetics model calculates the enhancements of CO_2 , NO , and NO^+ radiation resulting from energy deposited in the upper atmosphere by solar electrons. Approximately 600 time- and energy-dependent rate equations are used to calculate the secondary electron distribution and the subsequent reactive and energy-transfer processes. The energy deposition model for the primary electrons is based on work by Grün, Rees and Strickland²⁴⁻²⁶ as implemented in AARC.²⁷ The chemical reactions and energy transfer processes are described in detail in References 12 and 27. The integration of the time-dependent differential equations is accomplished using the Gear algorithm.¹² The use of time-dependent kinetics results in a significant improvement over the steady-state treatment used in AARC. For example, according to SHARC the $\text{NO}(v=1)$ production efficiency per ion pair increases with time during the aurora as the result of collisional excitation of the increasing concentration of ground state NO .

SHARC uses a discretized -local time-dependent Boltzmann equation approach to solve for the secondary electron distribution, neglecting electron-electron interactions. The features and altitude dependence of secondary electron distributions in the atmosphere have been discussed in detail elsewhere.²⁸ Secondary electrons are formed via collisional excitation of N_2 , O_2 , or O , and undergo further collisions with atmospheric species, resulting in relaxation of the electrons and production of ionic and electronically excited molecular states. In SHARC, the secondary electrons are divided into fourteen energy bins. The general features of the secondary electron spectra are in good agreement with existing auroral models.

When the electrons interact with ambient upper atmospheric species, ionization generates odd nitrogen in the form of $\text{N}(^2\text{P})$, $\text{N}(^2\text{D})$, and the ground state, $\text{N}(^4\text{S})$. The production mechanisms in SHARC are direct dissociation of N_2 by the primary electrons, recombination of ions (e.g., NO^+) with secondary electrons, and charge transfer reactions of the primary ionic products. Collisions between nitrogen atoms and O_2 create NO . The net production rate is highly sensitive to the ratio of $\text{N}(^2\text{D})$ to $\text{N}(^4\text{S})$ formed, as the NO is formed primarily by reaction with $\text{N}(^2\text{D})$ and destroyed by reaction with $\text{N}(^4\text{S})$. The vibrationally excited NO is quenched by O and O_2 and also undergoes radiative relaxation. NO^+ is assumed to be formed primarily via the ion-molecule reaction of N^+ with O_2 , which competes with the charge exchange reaction forming O_2^+ . $\text{NO}^+(v)$ is quenched by N_2 and by radiative relaxation.

$\text{CO}_2(v_3)$ is efficiently excited by direct electron impact, which is prompt, and by energy transfer from $\text{N}_2(v=1)$, which is delayed. The coupling of the chemical kinetics to the radiative transfer is treated via a modified escape function approximation based on the work of Kumer.²⁹ The vibrationally excited N_2 is presumed to arise from secondary electron excitation, the $\text{N}(^4\text{S}) + \text{NO}$ reaction and from the quenching of $\text{O}(^1\text{D})$, and is removed by relaxation with O atoms and transfer to $\text{CO}_2(v_3)$. In SHARC, the $\text{N}_2(v)$ density is calculated simultaneously with the secondary electron distribution.

Figure 3 shows the $\text{N}_2(v)$ excitation efficiency for a typical calculation. It is seen that direct electronic excitation of N_2 is almost as important as its chemical production, and there is only a slight altitude dependence to the efficiencies.

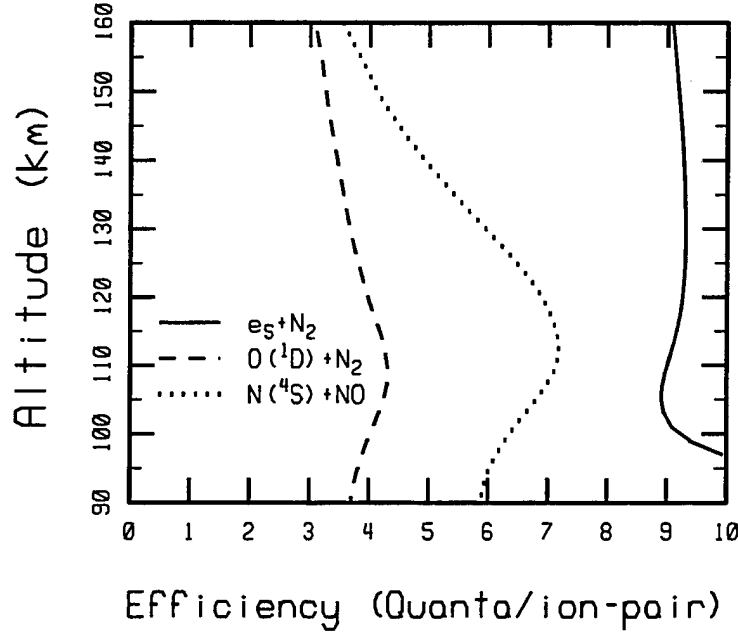


Figure 3. Prediction of the $N_2(v)$ Production Efficiency for Several Mechanisms.

2.4 Line-of-Sight Spectral Radiance Model

The LOS spectral radiance is calculated by numerically integrating the radiation transport equation along the LOS path. The approach in SHARC is based on an equivalent-width formulation for single lines. It is around 100 times faster than the usual line-by-line (LBL) grid method, which numerically integrates over the line shape. The spectral resolution of the calculation can be made as high as 0.5 cm^{-1} throughout the 50-300 km altitude range. Above 60 km, the lines are sufficiently narrow and optically thin that the resolution can be increased to 0.1 cm^{-1} .

The inhomogeneous LOS path is represented with a series of homogeneous atmospheric layers, and the equivalent width is calculated using an expression appropriate for Voigt line shapes. The mean line strength and width are derived from the Curtis-Godson approximation.^{30,31} After calculating the equivalent width for each line, the combined equivalent width for all lines within the spectral bin is calculated using an approximate (but typically small) correction for line overlap. Comparison to exact LBL calculations demonstrate that the overall errors in this approach are less than 10% for typical cases.

2.4.1 Calculation for a Single Line

With the atmosphere represented as a series of N homogeneous layers, the equation of LOS radiation transport for a single molecular line, j , is given by³²

$$I_j = \sum_{i=1}^N R_{ij}(\xi_{i+1} W_{(i+1)j} - \xi_i W_{ij}) \quad (6)$$

where the path is from the observer to the beginning of the i th layer, I_j is the observed radiance for the single emission line, i is the index for each atmospheric layer, R_{ij} is the molecular emission source function (in $\text{W}/\text{cm}^2/\text{sr}/\text{cm}^{-1}$), and W_{ij} is the cumulative equivalent width of the line for the path. The emission source function is given by

$$R_{ij} = \frac{C_1 v^3}{\pi} \frac{\gamma_{ij}}{1 - \gamma_{ij}} \quad (7)$$

where C_1 is the first radiation constant and γ_{ij} is the ratio of upper to lower state populations, defined by

$$\gamma = \frac{g_l \rho_u}{g_u \rho_l} \quad (8)$$

The subscript (l or u) denotes the lower or upper state, g is the degeneracy, and ρ is the number density. The states in Eq. (7) are defined by their vibrational, rotational and electronic labels, and the number densities in Eq. (8) are those calculated from the CHEMKIN and NEMESIS routines. For LTE conditions, $\gamma = \exp(-C_2 v/T)$, where C_2 is the second radiation constant, and R reduces to the standard Planck blackbody function. In the limit of no line overlap ($\xi=1$) Eq. (6) is exact provided that the equivalent widths are exactly determined. However, this is computationally time consuming. By using the approximations described below, a rapid evaluation of the equivalent width can be achieved with only a modest sacrifice of accuracy ($\sim \pm 10\%$).

For Voigt lineshapes, which apply to upper atmospheric conditions, the Rodgers-Williams approximation³³ to the single-line equivalent width provides a reasonable compromise between computational efficiency and accuracy. It is given by

$$W_{ij}^2 = W_v^2 = \alpha_D \frac{2}{\ln 2} [W_L^2 + W_D^2 - (\frac{W_L W_D}{W_W})^2] \quad (9)$$

where the subscripts V, D, L, and W refer to Voigt, Doppler, Lorentz, and weak-line limits, and α_D (cm^{-1}) is the Doppler linewidth. The equivalent widths are calculated using the approximations³²

$$W_W^2 = \frac{\ln 2}{2} \left[\frac{S u}{\alpha_D} \right]^2 \quad (10)$$

$$W_D^2 = \ln(1 + W_W^2) \quad (11)$$

where α (cm^{-1}) is the line width, S ($\text{cm}/\text{molecule}$) is the line strength, and u ($\text{molecules}/\text{cm}^2$) is the absorber column density. The errors in the computed W_v are comparable to the 8% peak errors in the approximations for W_D and W_L . These expressions for W_D and W_L are more quickly calculated than the more accurate polynomial series of Rodgers and Williams.

Since the above expressions apply to a homogeneous gas, and the atmosphere between the observer and each layer is inhomogeneous, Curtis-Godson^{30,31} path-averaged values of Su , α_D , and α_L are used. The line parameters (strengths and air-broadened half-widths) are tabulated in a file

$$W_L^2 = \frac{[Su]^2}{1 + \frac{Su}{4\alpha_L}} \quad (12)$$

generated from the HITRAN atlas¹⁷ that has been supplemented with lines for NO^+ and higher vibrational states of NO and O_3 .

In the absence of line overlap, the radiances for each line within the spectral bin would sum to form the total radiance and the equivalent widths for each line would sum to form the total equivalent width. The presence of overlap reduces these total quantities. A simple line overlap treatment is used which provides reasonable agreement with exact results for typical atmospheric conditions. The assumption, valid in the statistical limit, is made that the lines are randomly distributed within each bin. The overlap correction factor for the spectral interval Δv is given by

$$\xi_i = \Delta v [1 - \prod_j (1 - \frac{W_{ij}}{\Delta v})] / \sum_j W_{ij} \quad (13)$$

where the product and sum is over all lines in the interval. It is implicitly assumed that the spectral interval Δv is larger than the largest single-line equivalent width for the entire LOS. Within the altitude range of SHARC (tangent paths > 30 km), atmospheric linewidths are less than 0.01 cm^{-1} , and equivalent widths remain small enough over the entire spectrum that Δv can be set as low as 0.5 cm^{-1} .

2.4.2 Illustrative Calculations

The accuracy of the LOS radiance algorithm has been explored through comparisons to standard high-resolution LBL calculations for typical atmospheric conditions. A number of different regimes were investigated, including vertical and horizontal viewing geometries, optically thin and thick lines, multiple overlapping lines and bands, and LTE and non-LTE conditions. Below, we discuss representative results for the CO_2 $15 \text{ }\mu\text{m}$ region.

Evaluations of the Curtis-Godson and Rodgers-Williams approximations are illustrated by calculations on two individual $\text{CO}_2(\nu_2)$ lines, one strong (Q10, $\omega_0 = 667.494 \text{ cm}^{-1}$, $S = 3.35 \times 10^{-19} \text{ cm}^{-1}/\text{molec}/\text{cm}^2$ at 244 K) and one weak (R56, $\omega_0 = 713.134 \text{ cm}^{-1}$, $S = 8.24 \times 10^{-22} \text{ cm}^{-1}/\text{molec}/\text{cm}^2$

at 244 K). The 1976 US Standard Atmosphere³⁴ was used to define the kinetic temperature and species number densities. The atmosphere is layered into 2 km steps from 51 to 149 km and 10 km steps from 155 to 295 km. We consider two types of multi-segmented paths, zenith views from 60.5 km altitude to 65.5, 71.5, 81.5, and 101.5 km altitudes, and a 60 km limb path. The vertical paths thus have 3, 6, 11, and 21 segments along the LOS while the limb path has 121 segments along the LOS.

The calculated radiance values compared with "exact" LBL grid calculations typically result in errors ranging from 3.4 to 4.9% for strong lines and from 2.0 to 8.7% for weak lines. These errors are consistent with those expected for the equivalent width approximations. The limb calculation with the strong line is a good test since the temperature, pressure, and density vary considerably along the path.

A complete spectrum for the $\text{CO}_2(\nu_2)$ region is shown in Figure 4 for a 50 km full-limb view. This calculation provides a test of the line overlap treatment, since at this altitude there is significant overlap in the Q branch of the strong 667.380 cm^{-1} band. The agreement with an "exact" LBL calculation, carried out with FASCOD3, is seen to be excellent over virtually the entire 300 cm^{-1} spectral range and the six-order-of-magnitude range of radiance. The only major discrepancies are due to the omission in this SHARC version of three weak vibrational bands, which are responsible for the features around 508 , 582 , and 757 cm^{-1} .

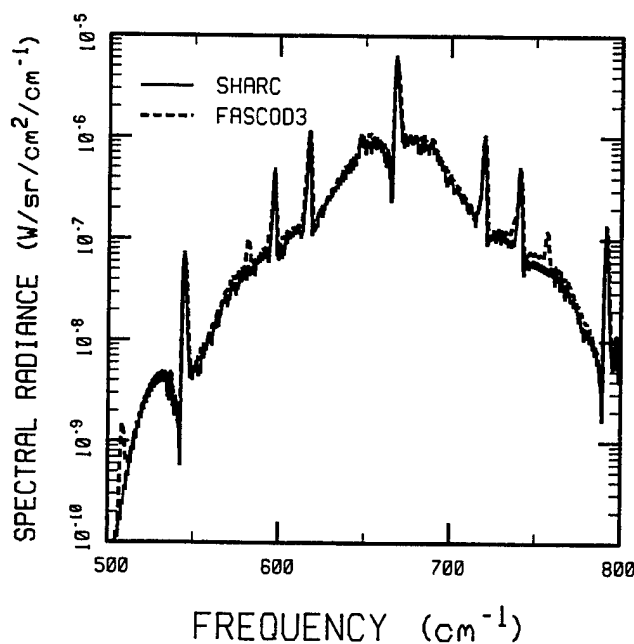


Figure 4. Comparison of SHARC and FASCOD3 Calculations of CO_2 Radiance for a 50 km Limb View.

2.5 Data Comparisons

While comparisons with other computer codes can validate the numerical procedures, comparisons with upper atmospheric IR data are needed to test the physical models in SHARC, including kinetic mechanisms, rate constants, and properties of the atmosphere. A comprehensive validation of these models will require a considerable effort and a very large measurement database. Here, we present illustrative comparisons of predictions and data from several rocket experiments sponsored by the Air Force Research Laboratory.

Figure 5 shows a predicted emission spectrum from the quiescent nighttime atmosphere in a near-limb view (4° elevation angle) from an altitude of 78 km. The spectral resolution has been degraded to 4 cm^{-1} FWHM. The 1400 to 3800 cm^{-1} region shown contains a varied assortment of molecular emission features, including resolved lines of the $\text{H}_2\text{O}(\nu_2)$ band (1400 - 1700 cm^{-1}), the $\text{NO } \Delta v=1$ band (1700 - 2000 cm^{-1}), which is emitted from thermospheric altitudes, several $\text{O}_3(\nu_1+\nu_3)$ bands (2000 - 2140 cm^{-1}) generated from chemiluminescent as well as collisional processes, the $\text{CO } \Delta v=1$ band (2100 - 2200 cm^{-1}), the $4.3\text{ }\mu\text{m}$ $\text{CO}_2(\nu_3)$ feature (2300 - 2400 cm^{-1}), consisting of a number of optically thick, radiatively trapped bands, and resolved $\text{OH } \Delta v=1$ nightglow lines (beyond around 2500 cm^{-1}). All of these emission bands are non-LTE.

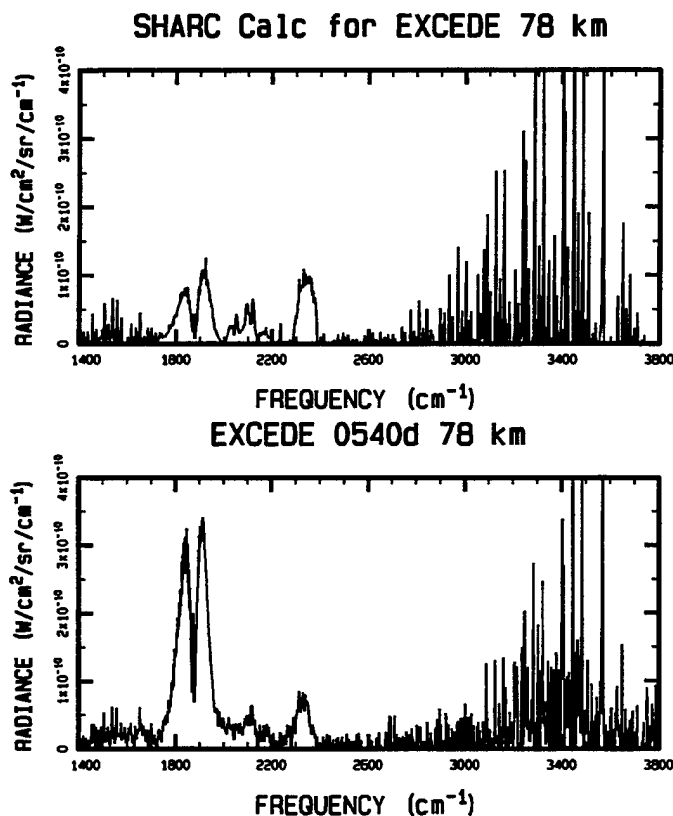


Figure 5. Comparison of SHARC Calculation (Top) and Observation (Bottom) of Quiescent Nighttime Emission in a Near-Limb View from an Altitude of 78 km.

The SHARC calculation simulates the quiescent atmospheric radiance during the recent EXCEDE III experiment,³⁵ which measured IR emissions induced by dosing the atmosphere with an electron beam. The experiment, flown in April 1990 from White Sands Missile Range, NM, collected both beam-on and beam-off data in a slant-viewing geometry using cryogenically-cooled Michelson interferometers that covered a wide spectral range (around 500-5000 cm^{-1}) with high resolution (approximately 2 cm^{-1}). Late in the flight, the sensor rolled towards the horizon, and during a beam-off period near 78 km altitude it obtained data, shown in the lower panel of Figure 5, in an average viewing geometry similar to that of the SHARC calculation in the top panel of Figure 5. All of the features predicted by SHARC appear to be present, and they generally agree very well in both shape and absolute intensity. An exception is the NO band, which is three times stronger than predicted, indicating too low a concentration in the SHARC model atmosphere. This discrepancy is not very disturbing considering the large variability of NO. The good quantitative prediction of the $\text{CO}_2(\nu_3)$ feature is quite satisfying, since it presents the most severe test of SHARC's atmospheric excitation and LOS radiation transport algorithms.

A more detailed examination of the $\text{CO}_2(\nu_3)$ feature is provided in Figure 6, which shows limb radiance profiles measured in another experiment, SPIRE,¹⁸ launched from Poker Flat near the dawn terminator. Different phenomena dominate the excitation in various altitude ranges, and this is reflected in the solar angle dependence. During the day, the primary isotope is solar-excited above 110 km, while at lower altitudes the radiance is enhanced by pumping of the 2.7 μm band and by emissions from hot bands and minor isotopes. As the density increases, the solar excitations are quenched, and single-quantum excitation of the primary isotope again dominates. The good agreement between the data and the SHARC calculations indicates that these processes are treated accurately.

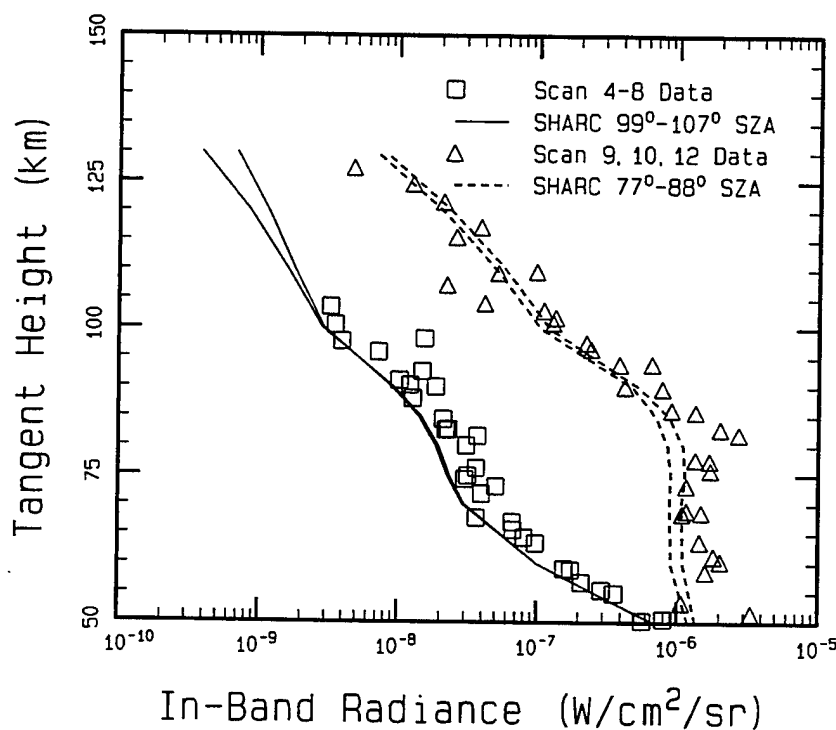


Figure 6. Comparison of SHARC Radiance Profile with SPIRE Data under Daytime and Nighttime Conditions.

An example of SHARC's auroral capability is shown in Figure 7. A nitric oxide spectrum from the 1973 Field-Widened Interferometer experiment,³⁶ which observed an IBC Class II aurora, is compared with a SHARC model calculation at a resolution of 1 cm^{-1} . The overall band shape, which includes strong aurorally-induced hot band contributions, is reproduced well by the calculation, except near the edges of the band where non-LTE rotational populations, not currently modeled in SHARC, yield enhanced high-J lines. The overall absolute radiance falls to a factor of four below the data; however, the results are quite promising for a first principles calculation that starts with electron dosing of the ambient atmosphere.

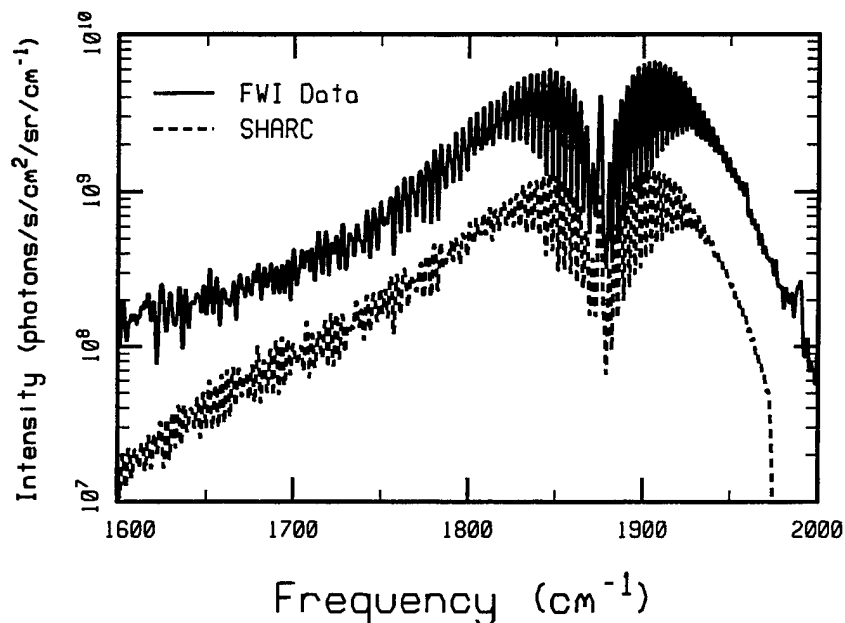


Figure 7. Calculated and Observed NO Spectrum for a 90 km Zenith View During a Class II Aurora.

3. DEVELOPMENT OF AN INTERACTIVE ATMOSPHERE GENERATOR MODEL

One of their most critical applications of radiance models is the prediction of radiance variations, which can occur over a wide range of spatial and temporal scales. Short-term and small-scale variations associated with random processes can be characterized statistically but cannot be predicted. On the other hand, systematic variations, which can be predicted, can be quite large and thus play an important role in setting the overall background radiance level for a given bandpass. In particular, at the solar terminator, large radiance variations can occur over a small (several-degree) range of solar angle due to photochemical processes in the atmosphere.

The SHARC Atmosphere Generator (SAG) has been designed to allow the major known systematic variabilities in the atmosphere, including terminator and other diurnal effects, to be practically incorporated in strategic IR radiance calculations. SAG is presently implemented as a stand-alone, interactive FORTRAN program which generates a file of species and kinetic

temperature profiles compatible with SHARC and SAMM, and an additional atmosphere file for use with MODTRAN and LOWTRAN. The profiles are customized for the geophysical and geographic information input by the user.

Using information on the day of the year, local time, solar activity indices, etc., SAG reasonably models the systematic variabilities in CO₂, O₃, OH, NO, H₂O, and O atom densities. For other species, diurnally-averaged profiles are taken from recent databases. To facilitate use without detailed inputs, defaults are provided so that simple designators, such as day/night, season, and latitude region (low, mid, or high), can be specified as desired.

SAG draws primarily on two existing empirical atmosphere models. MSISE-90³⁷ is used for the temperature and major species profiles. It provides profiles for species including N₂, O₂, O, and H as a function of altitude, latitude, longitude, universal time (UT), local solar time (LST), daily Ap index, and the F10.7 and F10.7A (30 day average) indices. The second atmosphere model is a new NRL climatology database³⁸ for altitudes up to 120 km. This database is used for the SHARC species CH₄ and CO, and for lower portions of the O₃ and O profiles, as well as for the additional species N₂O, NO₂, and HNO₃ used in SAMM. The NRL database contains mean monthly concentrations at 1 to 5 km increments and 10° latitude increments. SAG interpolates between these values and converts to number densities using the MSISE-90 total densities.

The remaining species profiles, including those for CO₂, NO, H₂O, OH, SO₂, and NH₃ are derived from a combination of standard concentrations³⁹ used in LOWTRAN and MODTRAN (SO₂, NH₃), photochemical or empirical models based on MSISE-90 inputs or outputs (CO₂), or some combination of these (NO, H₂O, OH), as described in this report.

3.1 Profile Computations

This section describes how the atmospheric profiles are generated. The N₂ and O₂ profiles are taken directly from MSISE-90 and have been discussed in detail in Hedin's³⁷ paper. Brief discussions are given in the following subsections on the profiles for temperature and the remaining species.

Diurnal variations in the CO₂, NO, O₃, O, and OH densities are handled in an empirical, analytical manner in SAG using an interpolation weighting factor, W, in combination with limiting daytime and nighttime profiles:

$$X(LST) = W(LST)X_d + [1 - W(LST)]X_n \quad (14)$$

Here X(LST) is the density of species X at time LST, X_d is the daytime (equilibrium) density and X_n is the nighttime (equilibrium) density. W approaches or equals 0 during the night and 1 during the day, and is set to 0 during continuous polar nighttime and 1 during continuous polar daytime. For CO₂ and NO, W is calculated with the assumptions that the approach to the daytime or nighttime equilibrium starts immediately at sunrise or sunset (SZA = 90°) and proceeds with a characteristic time constant, τ. An analytical solution to W(LST) exists in this case. In calculating the sunrise and sunset LST's, 0° longitude is assumed. This can lead to a small error, typically less than one minute, compared to the sunrise and sunset times at the actual longitude.

For O_3 , O , and OH , the chemical time constants are often comparable to or shorter than the sunrise or sunset duration. For these profiles, an alternative empirical interpolation factor is developed that is an explicit function of solar zenith angle (SZA) rather than LST. A detailed description is given in the subsection on O_3 .

3.1.1 CO_2

The CO_2 profile is computed from specified nighttime and daytime ratios relative to the argon number density, which is obtained from MSISE-90. Below 90 km, a fixed CO_2/Ar ratio is used, based on a ground level CO_2 mixing ratio of 340 ppm. Above, the ratio decreases, and separate daytime and nighttime equilibrium ratios are used. The relaxation time constant τ is taken as 8 hr.

Above 90 km, the daytime and nighttime CO_2/Ar ratios were obtained by combining the theoretical calculations of Rodrigo et al.⁴⁰ for sunrise (representing nighttime equilibrium) and sunset (representing daytime equilibrium) with mass spectrometric measurements. MSISE-90 was used to compute Ar densities corresponding to the conditions of Rodrigo et al.; using their CO_2 densities, the CO_2/Ar ratios were taken. These ratios were then systematically rescaled for overall consistency with measurements from the daytime Aladdin experiment⁴¹ and lower-altitude nighttime measurements.⁴² The resulting daytime and nighttime ratios are shown in Figure 8 along with the theoretical calculations and the Aladdin measurements.

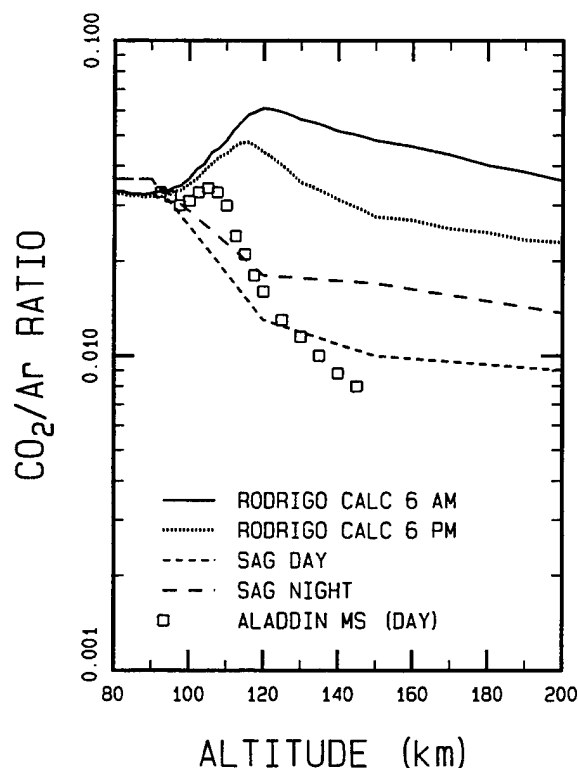


Figure 8. Comparison of Observed (Aladdin Mass Spectrometer), Calculated,⁴⁰ and SAG Model CO_2/Ar Density Ratios.

CO₂ concentration profiles generated by this model, such as the examples in Figure 9, are found to be consistent with measurements summarized in a recent review,⁴³ and are very similar to mid-latitude profiles used previously for IR radiation modeling.^{43,44} Very recently, new CO₂ concentrations have been derived from ATMOS data⁴⁵ at altitudes of up to 120 km. The model is found to provide an excellent representation of the average of these somewhat scattered measurements. From these comparisons, the SAG CO₂ profile is estimated to be accurate to within $\pm 30\%$ or better in the 100-150 km range.

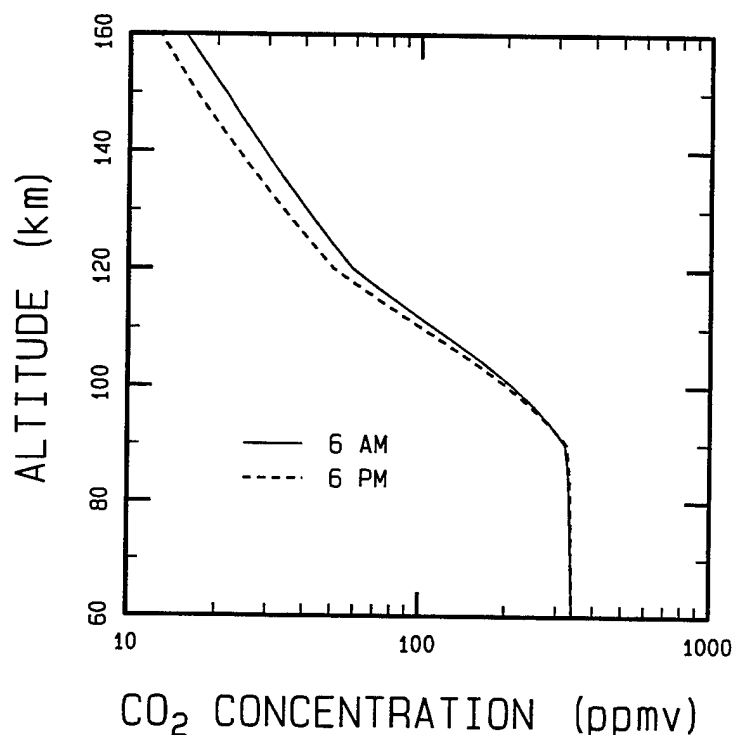


Figure 9. CO₂ Concentration Profiles for Autumn, Mid-Latitude, Moderate-Activity Conditions.

3.1.2 NO

Below 90 km, the NO concentration is taken from the AFGL Constituent Profiles tabulation.³⁹ While the actual concentration should have strong diurnal and latitude variations, little or no NO radiation is expected to be observable from this altitude range due to competing sources. At higher altitudes, NO emission is quite strong, so the variations need to be modeled. Above 100 km, separate daytime and nighttime profiles are calculated from the empirical latitude, temperature, and Kp-dependent models of Smith et al.,⁴⁶ as discussed below. The time constant τ is taken as 3 hours. The densities between 90 and 100 km are estimated by interpolation.

The daytime and nighttime profiles were chosen to give consistency with the latitude-dependent diurnal variation in NO reported by Smith et al. and with low-latitude satellite measurements⁴⁷ during daylight hours. The nighttime profile above 100 km is specified using a fitting parameter, the so-called equatorial night/day ratio $NO_e(n)/NO_e(d)$, which is given an altitude-dependent value of between 0 and 0.2. This ratio is a fictitious quantity since the minimum latitude absolute value

for the NO computation is taken to be 10^9 , to ensure that finite values of nighttime NO are obtained at the equator. For latitude absolute values $> 70^\circ$, the latitude is "folded back" (i.e., effective latitude $= 140 - \text{lat}$) to give better agreement with satellite data compiled by Barth.⁴⁸ Taking average nighttime and daytime NO densities as represented by LST = 0 and 12 hr respectively, the results at 110 km are in reasonable agreement with the data compiled by Smith et al. The time-dependent behavior of NO according to this empirical model is shown in Figure 10. The low-latitude simulation reasonably reproduces the increase in mesospheric NO at sunrise found in the Atmospheric Explorer C measurements.⁴⁷ However, it predicts the maximum to occur at sunset, whereas the observed maximum is somewhat earlier, in the mid-afternoon. The nighttime behavior of NO at low latitudes is not known from measurements, as the satellite data are from a solar fluorescence technique and there have been very few rocket measurements at low latitudes. Available IR measurements⁴⁶ show little diurnal variation at polar latitudes.

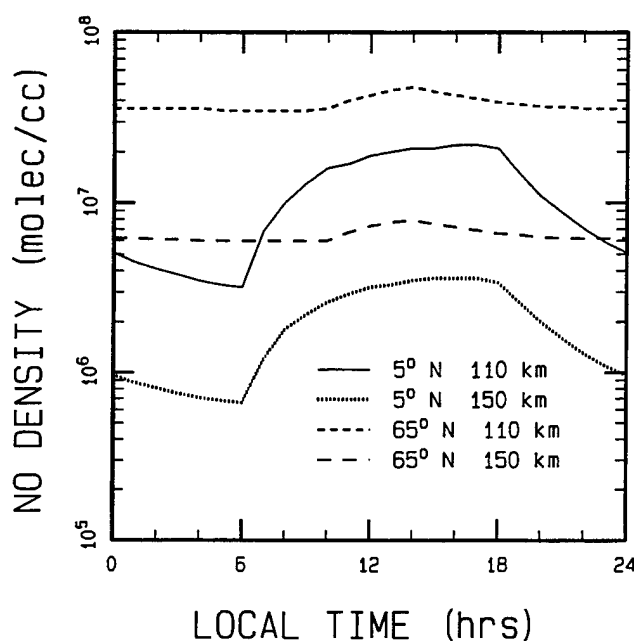


Figure 10. Diurnal Dependence of NO Densities for Autumn, Moderate-Activity Conditions.

3.1.3 O Atoms

The MSISE-90 O atom profile has been adopted above 86 km altitude. However, at lower altitudes it is unrealistic, as it lacks a diurnal variation. Alternative approaches were therefore used for the lower altitudes.

Daytime and nighttime profile shapes from 72 to 86 km (scaled to the MSISE-90 value at 86 km) were estimated from various measurements and calculations in the literature. The nighttime profile is essentially equivalent to that of MSISE-90 and the U. S. Standard Atmosphere. Below 72 km, the daytime O atom profile is computed from the daily average value from the NRL climatology database³⁸ under the assumption that the nighttime value is zero; the day length is accounted for. The result is rescaled to match the lower boundary of the 72-86 km region daytime profile. The scale factor is typically between 0.6 and 1.6. The O atom profiles are switched from day to night

using the linear interpolation scheme of the ozone terminator model, discussed in the following subsection.

The predicted O atom profiles should be reasonable at most altitudes during the day, when the concentration is nearly in steady state, but almost meaningless for altitudes below 80 km at night, when the concentration drops rapidly. Fortunately, such low O atom concentrations are believed to have little impact on atmospheric IR radiation.

3.1.4 O₃

The ozone profile is presently derived from a combination of the NRL database³⁸ and a photochemical equilibrium model. The NRL database contains daytime mixing ratios and night/day ratios, and is used below 72 km. The latitude range is restricted to $\pm 60^\circ$ to avoid difficulties during continuous polar day and night. The photochemical model is used at 80 km and above, and the two regions are connected by interpolation.

The photochemical equilibrium model accounts for ozone formation from O atoms and destruction via H atom and O atom reactions (the former yielding OH) and solar photolysis. Standard rate constants from the recent literature^{40,49} have been adopted. The inputs are the temperature, N₂, O₂, O, and H profiles and, if daytime, the photolysis rate. As discussed in the following subsection, uncertainty in the MSISE-90 H atom profile leads to a comparable uncertainty in the nighttime ozone. A two-body radiative association term is included as a formation mechanism, and has a significant and increasing impact above 100 km. The value of the rate constant, 8×10^{-21} cm³/molec/s, is estimated from rate constants for formation and relaxation of the O₂-O complex⁵⁰ and from ν_3 band Einstein coefficients. It is almost certainly an upper limit. However, for systems applications it is safer to overestimate the ozone than to underestimate it. Furthermore, any overestimation from this 2-body channel would be offset by the presence of certain O₂⁺ + O₂ reactions that have been proposed to form ozone⁴⁹ but which are not presently included in SAG.

A comparison of typical SAG and NRL ozone concentration profiles is provided in Figure 11. There is quite good agreement between the two, except at 80 km at night. This can probably be ascribed to a slight underestimation of the H atom density at that altitude by MSISE-90.

The transition between the day and night profiles is handled using a simple empirical model that approximates the terminator behavior in the time-dependent calculations of Rodrigo et al.,⁴⁰ which were performed for mid-latitude equinox conditions above 60 km. The transition is made by linearly interpolating over a 5° range of SZA computed for LST-0.075 hr; the 0.075 hr (4.5 min) difference accounts for the approximate photochemical lag time. The midpoint of the interpolation region is taken to vary linearly with altitude at the rate of 0.12° per km. Based on a comparison with the calculations of Rodrigo et al. This simple representation of the terminator location and width should be accurate to within around 1° in SZA in the 70-100 km altitude region. Typical time-dependent profiles generated by SAG for the dusk terminator are shown in Figure 12.

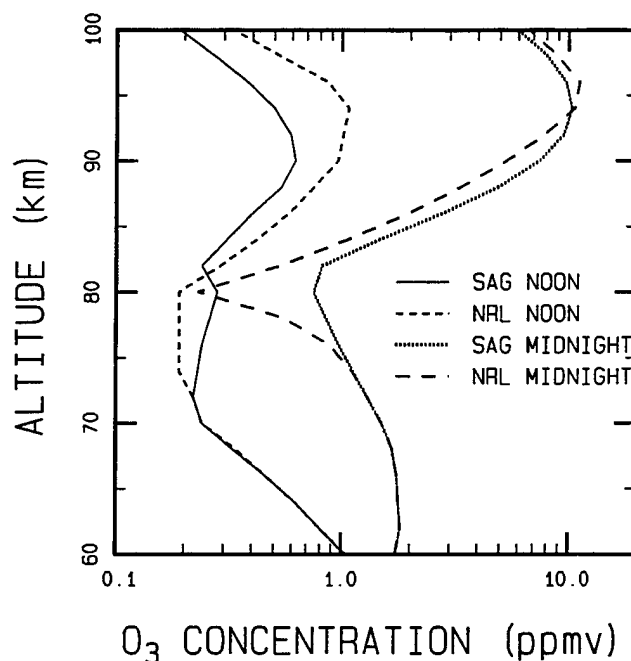


Figure 11. Comparison of SAG Model and NRL Climatology Ozone Concentrations for Fall Equinox, 45° N, Moderate-Activity Conditions.

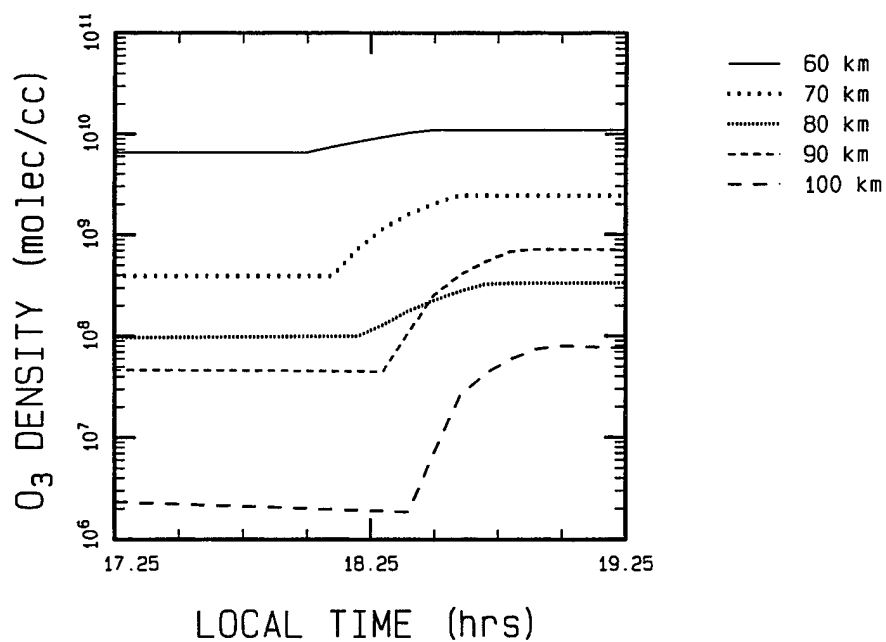


Figure 12. Time-Dependence of Ozone Concentrations at the Dusk Terminator for Fall Equinox, 45° N, Moderate-Activity Conditions.

3.1.5 OH

The OH profile is taken from a standard profile tabulation³⁹ below 72 km, a chemical equilibrium model above 80 km, and interpolated values in between. The chemical model, involving formation via the $\text{H} + \text{O}_3$ reaction and destruction via O atoms, insures that the H, O_3 , and O concentrations are self-consistent and thus accounts for diurnal variation. The standard profile neglects diurnal variation. Little or no sensitivity of atmospheric radiance to the ground state OH density is expected, since it neither contributes to nor significantly absorbs the dominant chemiluminescent (Meinel band) radiation from the higher vibrational states.

3.1.6 H Atoms

The H atom profile is taken from MSISE-90. As with the O atom profile, the H atom profile cuts off below 74 km, and its accuracy is suspect below 80 km due to the lack of diurnal variation. Compared with the nighttime H atom profiles derived by Thomas⁵¹ for the 80-93 km altitude range, the corresponding MSISE-90 predictions appear to average a factor of 2 to 4 lower. However, the uncertainty in Thomas' values is reportedly a factor of 2, and other experiments^{52,53} show better agreement with the MSISE-90 profile.

If the H atom profile were indeed too low, the photochemical model for ozone and OH, implemented at and above 80 km, would predict too much O_3 at night and too little OH during the day. There is some evidence for the first effect at 80 km (see Subsection 3.1.4). However, the daytime O_3 and nighttime OH densities are not affected by the H atom density.

3.1.7 CO and CH_4

These profiles are taken from the NRL database³⁸ for altitudes up to 120 km. Above 120 km the mixing ratios are set equal to the 120 km values; this should result in an upper limit to the expected IR radiances, which are extremely small, however.

3.1.8 H_2O

Due to problems in the current NRL database³⁸ for water vapor, an alternative empirical model has been developed for SAG which combines the LOWTRAN models in Reference 39 with the recommendation in Reference 18 for the upper troposphere. Between 0 and 8 km the profile is a linear fit to the LOWTRAN models for relative humidity, which indicate an average humidity of approximately 75% at the ground and 30% at 8 km. As recommended in Reference 54, above 8 km the mixing ratio is logarithmically interpolated to the value of 4 ppmv (2.5 ppmm) at the tropopause, which we take as the altitude of the MSISE-90 temperature local minimum. (In the unlikely event that the tropopause is below 9 km, it is assumed to be at 9 km for the purposes of this calculation.) At 40 km and above, the standard profile from Reference 39 is used. Between the tropopause (4 ppm mixing ratio) and 40 km (approximately 5 ppm mixing ratio) the mixing ratio is logarithmically interpolated.

3.1.9 Additional Species for SAMM

The species N_2O , HNO_3 , and NO_2 are taken from the NRL database.³⁸ These profiles include seasonal and latitude variabilities, but do not address the diurnal variability, which in the case of NO_2 is very large due to daytime depletion by the $\text{NO}_2 + \text{O}$ reaction and by photolysis. The species SO_2 and NH_3 are not covered by the NRL database, so the standard LOWTRAN/MODTRAN profiles³⁹ are used.

3.2 Temperature

The empirical MSISE-90 model developed by Hedin³⁷ provides a smooth extension of the widely-used MSIS upper atmospheric model to the lower atmosphere. The accuracy of the temperature profiles above 120 km, which are based on mass spectrometer, incoherent scatter and satellite drag data, has been discussed in Hedin's documentation for previous MSIS versions. The temperature profiles in MSISE-90 have been designed to follow standard lower atmosphere climatology compilations quite closely (to within several degrees) under most conditions.

The MSISE-90 temperature profiles are probably suitable for most SHARC applications. It should be noted, however, that IR radiances can be extremely temperature-sensitive, particularly at low temperatures. One altitude region where the temperature uncertainty may be significant is directly above the mesopause, where there is a steep gradient. To ensure that the best possible profiles are used, MSIS upgrades are expected to be incorporated in future versions of SAG.

4. DEVELOPMENT OF A TERMINATOR MODEL

One of the most critical applications of atmospheric radiance codes is in modeling spatial variability, which is an important effect in the solar terminator (earth shadow edge) region. Two types of effects can occur which lead to spatial radiance variations at the shadow edge. One is a change in molecular number densities due to photochemical processes, such as the photolysis of ozone (O_3). The other is a change in the vibrational excitation with the solar zenith angle. The net result in either case can be a substantial variation in the spectral radiance for many molecular bands, including O_3 (9.6 μm), CO_2 (4.3 μm and 2.7 μm), and OH (~1.9 μm and ~3.3 μm).

The section discusses an approach for the accurate modeling of the terminator region through the use of multiple atmospheric profiles corresponding to different solar angles in the SHARC code. The spectral radiance may be calculated for an arbitrary line-of-sight (LOS) passing through up to seven profiles. Interpolation is used to characterize the atmosphere between the solar angles assigned to each profile. The number of profiles is sufficient to accurately describe the characteristics of the shadow edge in any arbitrary view (parallel, perpendicular, or oblique).

In the current investigation, a new version of SHARC, SHARC-3, was used to simulate terminator limb radiances for CO_2 , O_3 , and OH that correspond to field observations. Dawn terminator data for the CO_2 4.3 μm band were selected from the 1977 SPIRE rocket measurements.¹⁸ New SHARC simulations were performed using an input atmosphere from the SHARC Atmospheric Generator (SAG) discussed in Section 3, a model that utilizes recent climatology databases, empirical models, and theoretical calculations to construct appropriate atmospheric profiles for any desired conditions. The calculated CO_2 radiances are in good agreement with the SPIRE data as well

as with simulations performed using GL's line-by-line code RAD.²¹ In addition, we have simulated dusk terminator emissions from O₃ and OH measured in the 1991 CIRRIS-1A space shuttle experiment.⁵⁵ The reasonable agreement obtained serves to validate both the SHARC code and the SAG solar angle-dependent model for O₃ concentration.

4.1 Calculation Methods

Two slightly different methods for performing SHARC terminator calculations were used in the current investigation. The CO₂ 4.3 μ m simulations for SPIRE were performed using a multiple-regions version of SHARC-3. Five atmospheric regions corresponding to different solar angles were defined with explicit geographic boundaries. For convenience, a transformed coordinate system was used in which the scan-center tangent point was placed on the equator and the solar angle served as the longitude coordinate. The atmospheric regions were stacked along the equator and bounded by longitude lines; the boundary longitudes were chosen as the mean of the solar angles assigned to the two regions on either side of the boundary. One of the five regions was "extended", i.e., had no boundary. This region was placed at one end of the stack.

For simplicity, the vehicle was regarded as stationary during each spatial scan (this is a good approximation for SPIRE and other rocket experiments). Since the azimuth angle was also fixed during the scan, the entire limb radiance profile for the scan could be mapped out by changing only the LOS tangent height.

The O₃ and OH simulations for CIRRIS-1A were performed using the multiple-profiles feature in the official release of SHARC-3. Seven atmosphere profiles, corresponding to a 92°-104° solar zenith angle (SZA) range, were specified in a single quiescent region. The actual latitudes and LOS azimuth angles for the experiment were used. The correct placement of the sun was achieved through the choice of input longitude.

The only real difference between using a single profile within multiple regions (in the CO₂ calculations for SPIRE) as opposed to multiple profiles within a single region (in the calculations for CIRRIS-1A) is that in the latter case the vibrational state populations are interpolated along the LOS, whereas in the former case they are constant within each region and change abruptly at the boundaries. For radiators such as CO₂ where the solar angle-dependence of vibrational state populations is gradual, the calculated limb radiances are similar with either approach. With O₃ and OH emissions, which change dramatically over a several-degree solar angle range, the interpolation provided in the multiple-profiles method should give smoother results.

4.2 Results and Comparisons

4.2.1 CO₂ 4.3 μ m

Calculations of the 4.19-4.49 μ m bandpass radiance were carried out to simulate the SPIRE "terminator/night" scans 1, 4 and 8 and the "day" scans 9 and 11. For the former, five layers at 2° SZA increments were used, for a total SZA range of 10° along the LOS. This is sufficient for coverage of tangent heights up to 150 km or greater. For scan 8, which looked much farther into the night than the other two, a low-solar-angle extended region was substituted for the daylit extended

region used in the scan 1 and scan 4 calculations. For the day scans 9 and 11, which have generally greater East-West ranges, the atmospheric regions were made three and four degrees wide.

4.2.1.1 CO₂ Vibrational Temperatures

To obtain some insight into the SZA-dependence of the CO₂ excitation and the convergence properties of the calculations, we tabulated the vibrational temperature of the main isotope (00011) state (associated with the ν_3 cold band) for each atmospheric region. As expected, there is a general decrease with increasing SZA (Figure 13). The temperatures for one set of altitudes, around 119 km, track one another closely. High temperatures in region 1 are followed by approximately level temperatures in the darker regions. A similar trend appears at lower altitudes around 91 km, but the temperatures do not track. The small fluctuations appearing at this altitude are statistical, stemming from the finite number of Monte Carlo "photons" used in the NEMESIS routine that calculates the vibrational populations.

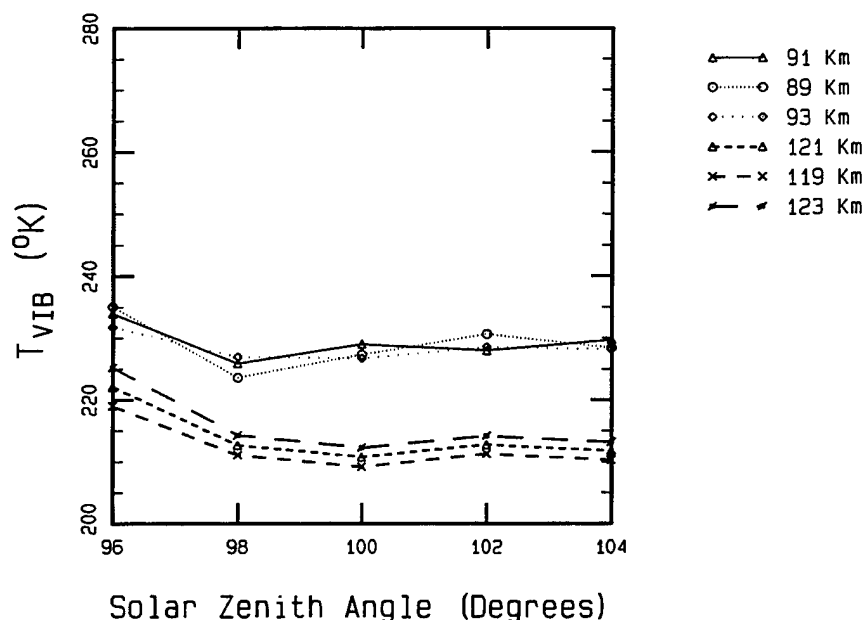


Figure 13. Solar-Angle Dependence of the CO₂ (00011) State Vibrational Temperature.

4.2.1.2 Radiance Profiles

The 4.3 μm radiance profiles from SHARC have already been shown in Figure 7 along with the SPIRE data. Since the data display significant scatter not correlated with SZA, data for similar angles have been collected into two sets, corresponding to day and night sides of the terminator. The scan 1 data are very limited and are not shown. Two SHARC profiles are shown for each set to indicate the sensitivity of the calculations to the SZA. No differences are found between the various nighttime calculations below 100 km, where strong atmospheric absorption of sunlight leads to total shadow. In other cases, minor differences are found. The agreement between the SHARC

calculations and the SPIRE data is seen to be within the data scatter. As can be seen in Figure 7, the SHARC calculations for 99 and 107 SZA are essentially nighttime except at the higher altitudes.

Preliminary SHARC calculations have also been performed to simulate CIRRIS 1A data, which have better signal-to-noise. The results, which will be reported in the future, indicate agreement to within a factor of 2 over the 50 to 125 km tangent height range. The SHARC radiances tend to be lower, particularly at the higher tangent heights. An underprediction of this magnitude has also been found by Wintersteiner and co-workers at nighttime using a different radiation code (RAD)²¹ with similar kinetic mechanisms.

4.2.2 O₃ 9.6 μ m

In contrast with CO₂, the variation in ozone radiance at the solar terminator is due to an abrupt change in concentration. Thus, the SHARC terminator results depend critically on how the ozone concentration profile changes with solar zenith angle in the model atmospheres. A discussion of the ozone profile derivation and validation has been presented in some detail in Section 3.1.4. Before we present the terminator results for O₃, the next section describes an upgrade to the O₃ chemical kinetics data base used in previous versions of SHARC.

4.2.2.1 An Improved O₃ Chemical Kinetics Model

This section discusses the modeling of non-LTE (non-local thermodynamic equilibrium) infrared emission from ozone in the upper atmosphere. Recent measurements from space platforms including CIRRIS-1A⁵⁵⁻⁵⁷ and SPIRIT-1⁵⁸ have provided new and detailed information on the atmospheric emission spectrum near the mesopause (80-100 km altitude region) in the 10-12 μ m window and nearby wavelengths. This region is dominated by non-LTE emissions from ozone (O₃) ν_3 high vibrational bands, solar-pumped CO₂ bands, and pure rotation lines of the hydroxyl radical (OH) at night. The data provide important benchmarks for the atmospheric radiation codes.^{7,21}

Prior versions of SHARC do not include a mechanism for exciting the recently discovered OH lines, and also uses a much earlier O₃ high- ν model based on the kinetic scheme and spectroscopic parameters of the older HAIRM code.⁵⁹ Recent analyses of the field data and laboratory measurements of quenching rate constants and vibrational energy levels indicated the need to upgrade the SHARC-2 O₃ model to include recent information on the location of the centers of the various hot bands and a more complete kinetic mechanism with additional emitting states.

The following subsection describes an upgraded O₃ model which has been implemented in SHARC-3. The new model provides an improved representation of the upper atmospheric ozone spectrum in the 10-12 μ m window, the ν_1 region near 9 μ m, and the $\nu_1+\nu_3$ region near 4.8 μ m. Comparisons are made with SHARC-2 results and with representative CIRRIS-1A data.

4.2.2.2 Overview of Ozone Models

The original HAIRM/SHARC-2 model for O₃ incorporates a number of one- and two-quantum states, but it considers only the (00N) (i.e., pure ν_3) states above three quanta. These states are assumed to be populated directly in the O + O₂ + M recombination and relax by $\Delta\nu_3 = -1$ radiative

and collisional processes. The high (00N) band centers are estimates based on a linear extrapolation from lower-lying states. This results in a structured spectrum of evenly-spaced bands that fall off rapidly towards lower wavenumbers, as shown in Figure 14. Using more recent estimates of the band centers, the (00N) bands are more widely spaced at high ν , making the predicted structure even more pronounced. In contrast with the SHARC-2 prediction, the CIRRIS-1A data near the mesopause show little obvious structure associated with the O_3 hot bands. Fine structure previously seen in SPIRIT-1⁵⁸ has been recently shown⁵⁷ to be due instead to the OH lines. The lack of O_3 hot band structure indicates that there are many more O_3 bands contributing to this spectral region than are present in SHARC-2.

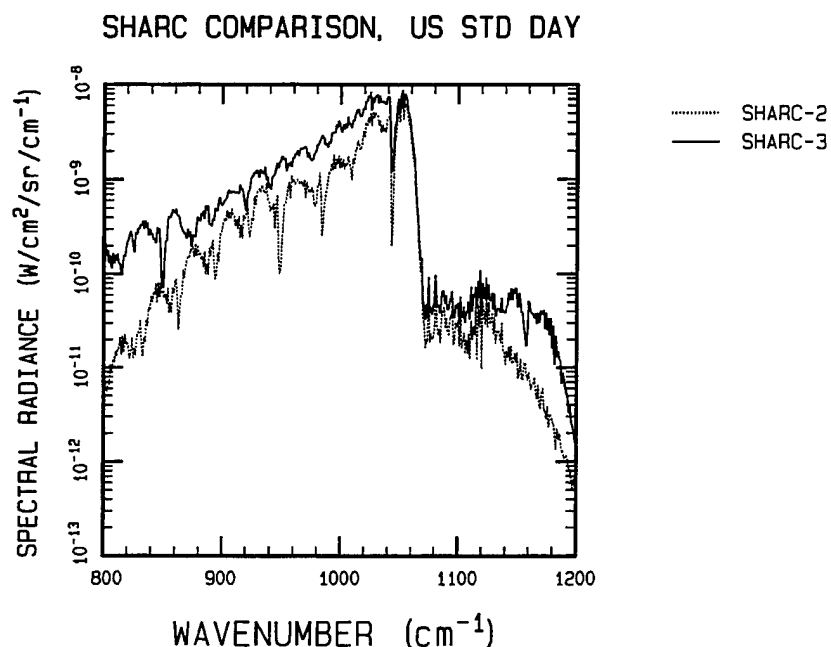


Figure 14. SHARC Calculations of 80 km Limb Radiance From Ozone Using the SHARC Daytime "U.S. Standard" Model Atmosphere.

To generate a sufficiently smooth spectrum, Adler-Golden and Smith⁶⁰ proposed that the populations of O_3 states having $\nu_1 > 0$ and $\nu_2 > 0$ are comparable to those of the (00N) states of similar energies or total vibrational quanta. This is in accord with results of detailed state-to-state kinetic model calculations.⁶¹⁻⁶³ In the COCHISE laboratory experiment⁶⁴ both the (00N) and (10N) states were detected, although ν_2 -excited states were not. However, Rawlins et al.⁶⁵ identified the (011)-(010) band in the atmospheric emission spectrum measured in the SPIRIT-1 experiment, and Green et al. (B. D. Green, unpublished data) have inferred high ν_2 -excited state populations from CIRRIS-1A spectra in both the ν_3 and $\nu_1 + \nu_3$ regions.

A fundamental difficulty for SHARC is that a complete state-to-state kinetic model for $O_3(\nu)$ would require a very large number of states. According to the established collisional relaxation pathways,⁶⁶ stretching quanta (ν_1 and ν_3) equilibrate among themselves and are also converted to bending quanta (ν_2), which relax primarily via V-T,R processes. This means that to calculate populations of even a limited subset of states such as (00N) all states having N total quanta must be

included in the kinetic scheme. For example, the state-to-state kinetic model of Manuilova and Shved⁶² for N of up to 3 includes all 20 vibrational states. Extension of their model to N=7, required to simulate the region near 800 cm⁻¹ (12.5 μm), would require 120 states. To implement this model in SHARC would entail a much larger and more complicated kinetics input file and around four times the number of vibrational bands compared to SHARC-2.

An alternative to such a complete kinetic model for ozone is an "effective" model employing a subset of states linked by fictitious relaxation pathways and rate constants. The HAIRM/SHARC-2 model is in this category, but as stated earlier it is incomplete. An alternative "effective" model that can account for all possible vibrational bands has been proposed by Adler-Golden and Smith.⁶⁰ We have implemented this model for 20 states having more than two quanta. While the work of Adler-Golden and Smith can be criticized for omitting the OH lines, making their band center assignments questionable, their basic hypothesis regarding the participation of bending-excited states is strengthened, rather than weakened, by this omission, since now the model must yield even less ozone spectral structure than before.

For the ten states having two quanta or less, SHARC-3 uses a complete state-to-state relaxation model similar to that of Manuilova and Shved⁶² and Joens et al.⁶⁷ Details of the kinetic model and its implementation are described in the next section. In the subsequent section, sample radiance calculations are presented and discussed.

4.2.2.3 SHARC-3 O₃ Model Description

4.2.2.3.1 *N > 2 Model*

The model proposed by Adler-Golden and Smith⁶⁰ (denoted AGS) is used to describe the kinetics of states whose total vibrational quanta, N, exceeds 2. The implicit physical assumptions are that, to first order, all states of a given N are equally populated, multiquantum relaxation is negligible, and the nascent ozone is formed entirely in states with N equal to or greater than the maximum in the model, N=7. In this situation, all vibrational states with a given N are assigned identical collisional and radiative relaxation rate constants which represent averages for the N manifold. The relaxation product states are not defined. Rather than letting relaxation feed the lower states, the formation rate for each state is specified by an "effective" rate constant which equals the total O₃ formation rate divided by the number of states with N quanta, which is $N^2/2 + 3N/2 + 1$. The N>2 states presently included in SHARC-3 are those having $v_1=0$ or 1 and $v_2=0$ or 1 (20 states).

The "effective" formation rate constants in the AGS model serve the same function as the "quasi-nascent" state distribution proposed by Rawlins and co-workers.⁶⁵ (A simpler, early version of the Rawlins model⁶⁸ involving only the (00N) states had been adopted for HAIRM and SHARC-2.) Besides the inclusion of bending states in the AGS model, another important difference is that the sum over all vibrational states of the "effective" rate constants exceeds rather than equals the net rate constant for O₃ formation. Together with the use of smaller, manifold-averaged radiative relaxation rates, the result is a larger overall radiance in the 11-13 μm window region.

Numerical values for the rate constants were derived as follows:

1. The manifold-averaged radiative relaxation rate is taken as $4N \text{ s}^{-1}$, representing approximately 1/3 of the Einstein coefficient for the (00N) states.

2. The rate constant for relaxation by N_2 and O_2 is taken as $1.3 \times 10^{-14} N \text{ cm}^3/\text{molec/s}$, and for reasons discussed by Adler-Golden et al.⁶⁹ the rate constant for O atoms is taken to be 400x larger. These values give the correct daytime hot-to-cold band intensity ratio when the recently measured relaxation rate constants of Menard et al.⁷⁰ are used to calculate the $N=1$ state populations. The scale factor of 1.3×10^{-14} is quite close to the measured (100),(001)→(010) and (010)→(000) relaxation rate constants for air at 200 K, the approximate atmospheric temperature in the altitude range of the hot band emissions.
3. To accurately model the $(1 \ v_2 \ v)/(0 \ v_2 \ v+1)$ state ratios, which are near thermal equilibrium, resonant exchange processes between these states are included. The rate constant values in the exothermic direction are taken as $1 \times 10^{-11} \text{ cm}^3/\text{molec/s}$ for N_2 and O_2 , consistent with the Menard et al. measurements of the (100)→(001) rate. The rate constants are assumed to be ten times larger for O atoms, in the absence of further information. The state populations are not expected to be sensitive to these precise values at most altitudes of interest.
4. The "effective" formation rates are computed as described above from the total formation rate constant. The latter is taken as $1.6 \times 10^{-27} T^{-2.6} \text{ cm}^6/\text{molec}^2/\text{s}$ based on literature measurements for standard air composition.⁶⁶

As mentioned earlier, in this model the relaxation processes do not feed the lower states. To implement this scheme in SHARC, the final states are specified as O_3 with no vibrational quantum numbers attached. As SHARC requires all vibrational radiative processes to be included in the kinetics scheme, the $\Delta v = -1$ transitions were listed in the kinetics file but their Einstein coefficients were set to zero.

4.2.2.3.2 $N \leq 2$ Model

The complete set of 10 states with $N \leq 2$ are included, along with best-guess estimates for their state-to-state collisional and radiative relaxation rates. The $N=2$ states are formed using the "effective" rate constants described above. The resonant v_1-v_3 exchange rate constants are identical to those used for $N > 2$. The other collisional relaxation rate constants are based on the measurements of Menard et al.⁷⁰ for N_2 and O_2 . Linear scaling is used when the mode losing a quantum has more than one initial quantum. Since both the N_2 and O_2 rate constants have similar temperature dependencies, to reduce the number of reactions in the input file the rates for O_2 are ratioed to those for N_2 . The ratio is taken as 0.8, in accord with the measurements near 200 K. As before, the O/N_2 rate constant ratios are taken as 400. This gives acceptable agreement with the measurements of West et al.⁷¹ if it is assumed that the O atom rates at room temperature and 200 K are similar. The actual temperature dependencies of the O atom rate constants are unknown. Detailed balance is included throughout.

4.2.2.3.3 Vibrational Energies and Spectroscopic Parameters

The vibration-rotation line parameters were taken from the 1992 HITRAN atlas¹⁷ where available. For bands not present on the atlas, such as those originating from states having four or more quanta, approximate line intensities and positions were generated by scaling and shifting corresponding bands of lower-energy vibrational states. The intensity scale factors assume harmonic

oscillator scaling of the transition dipoles. This approximation may overestimate the highest-energy band strengths [such as for (006)-(005)] by almost a factor of two, since it does not account for dilution due to the Darling-Dennison interaction.⁶⁰ Also, the postulated local resonance⁶⁰ between the (005) and (311) states has been neglected for the present.

The band center estimates are based on a recent semi-empirical energy level formula given in References 58 and 60. They are expected to be accurate to within several cm^{-1} for up to $N=5$ total quanta, where COCHISE data are available. Higher- N bands of ozone have yet to be identified in the IR. An extrapolation from $N=4$ was performed using the quadratic Darling-Dennison formula derived by Barbe et al.⁷² in 1974. The results are in good agreement with the $N=5$ band centers reported in COCHISE.⁶⁴ However, problems occur at higher energies. The dissociation energy of ozone is greatly overestimated,^{58,60} and even- v_3 states with six and seven quanta observed in recent resonance Raman spectra⁷³ are overpredicted as well. The discrepancy between the quadratic formula and the Raman data has been observed and discussed by several authors.^{74,75}

The improved energy level formula in References 58 and 60, adopted in the present work, gives a much better fit to Raman data for 6 and 7 quanta as well as the correct dissociation energy, although there is little difference at lower energies. It predicts that the (007) and (106) bands lie below 800 cm^{-1} . The bands originating from (006) and (105) are predicted to lie nearly on top of each other, in part due to the (311)-(005) resonance. However, even if they were well separated, they would still be unable to produce a spectrum as smooth as that observed in CIRRI-1A between 800 and 900 cm^{-1} . This has provided a major motivation, although not the only one, for including the additional bending-excited v_3 bands.

In addition, several other bands from the 1992 HITRAN atlas have been added to SHARC-3. One is the (200)-(001) crossover band, centered at 1159 cm^{-1} . As discussed below, it is clearly visible in the daytime simulations, when the total ozone concentration is low and the nearby v_1 cold band is weak. Two new two-quantum transitions have also been added, the (003)-(100) crossover band and the stronger (102)-(001) combination band. While we have not yet made comparisons with CIRRI-1A data in the region around $5 \mu\text{m}$ where these bands emit, we anticipate that the latter band at least should be observable, and that higher-energy combination bands (originating from states with $N>3$) that are not present in HITRAN might also be visible.

4.2.2.3.4 Results

The SHARC-3 model was run using the same input atmosphere (daytime "U.S. Standard") and view (80 km limb) as before; the result is shown in Figure 14. The smoother appearance of the window region is in better accord with the CIRRI-1A and SPIRIT-1 data, and the overall radiance is larger than before, especially at low wavenumbers. It should be noted that this model atmosphere contains atypically large O atom densities below 90 km, which results in higher O_3 formation rates. This, in turn, results in hot band radiation that is greater than normal.

The contribution from the (200)-(001) crossover band in SHARC-3 is observed above 1140 cm^{-1} . Intensity increases in the $1020\text{-}1140 \text{ cm}^{-1}$ region of the v_1 and v_3 cold bands are also observed. These probably result from the use of somewhat smaller $N=1$ deactivation rate constants.

SHARC-3 was also run using the SAG atmosphere for the nighttime conditions of the SPIRIT-1 experiment. Comparisons of the observed and predicted hot and cold band limb radiances between

80 and 100 km are shown in Figure 15. The hot bandpass is $930\text{-}976\text{ cm}^{-1}$ ($10.25\text{-}10.75\text{ }\mu\text{m}$), where the emission is mainly from four-quantum O_3 states. The SHARC radiances have nearly the observed ratio and are in good absolute agreement with the data up to around 90 km. Above that altitude the data fall off more rapidly, but this behavior is somewhat atypical as larger ozone radiances have been observed at these altitudes in other experiments including CIRRIS-1A and SPIRE. The cold band intensity would be reduced by nearly half at 100 km if the proposed two-body ozone formation reaction $\text{O} + \text{O}_2 \rightarrow \text{O}_3 + h\nu$ currently present in the SAG photochemical scheme were eliminated.

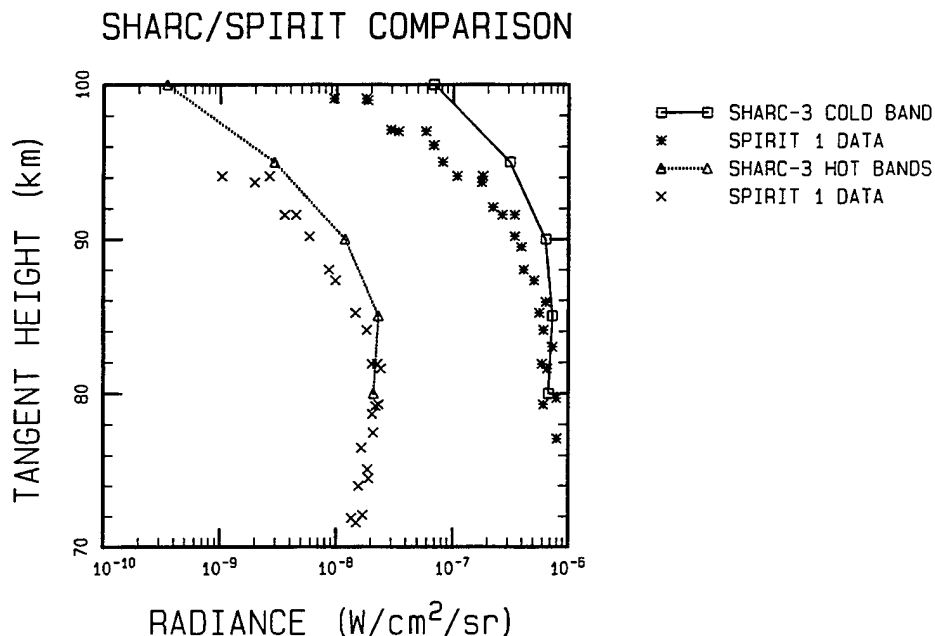


Figure 15. Predicted and Observed (SPIRIT-1) Nighttime Cold Band ($1000\text{-}1087\text{ cm}^{-1}$) and Hot Band ($930\text{-}976\text{ cm}^{-1}$) Limb Radiance Profiles. Input Atmosphere is from the SHARC Atmosphere Generator.

The ozone hot band spectrum for any representative atmosphere should be essentially the same except for differences in overall intensity. Comparisons of Figure 15 with CIRRIS-1A data suggest that the intensity envelope of the spectrum lies in between the two SHARC models. The SHARC-3 model may have somewhat overestimated the hot band strengths, as discussed earlier, and the linear scaling of the effective relaxation rate constants might have led to underestimates of the quenching at the highest vibrational energies ($N > 4$).

A "fix" that compensates for the likely hot band strength errors has been implemented in the latest SHARC-3 kinetics input file. In the new file, the "effective" formation rate constants are reduced by ratio of the AGS (Reference 60) theoretical transition dipoles (which take into account Darling-Dennison interactions and other anharmonic effects) to the harmonic oscillator-based transition dipoles used to generate the spectral lines for these bands. This results in essentially no change in the hot band structure, but a slightly steeper roll-off of intensity towards the red.

4.2.2.4 Terminator O₃ Radiance

SHARC calculations were performed to simulate selected data from the CIRRIS-1A experiment on O₃ v₃ radiance in the dusk terminator. The data were taken from a horizontal scan near 20° S latitude during Block PC11G, when a SZA range of 93° to 101° was covered with nearly constant elevation and azimuth angles. During this period, two radiometer detectors, numbered 1-4 and 1-6, acquired data at 89 km and 81 km tangent heights, respectively, in the 8.0-11.9 μm bandpass. The LOS was nearly parallel to the terminator.

The data and SHARC simulations are shown in Figure 16. The SHARC simulations show a smaller altitude dependence on the night side and slightly underestimate the day side radiance, but on the whole they agree reasonably with the data. The agreement is better at 81 km, which is closer to the peak of the ozone emission, than at 89 km. The differences on the night side may have to do with a mismatch between the calculated and actual ozone peak altitude, which averages around 83 km in CIRRIS-1A nighttime measurements but can fluctuate by several km. For these particular data, the peak appears to be several km lower than average. At 89 km, the scale height of the emission is very steep, so that a small change in the peak altitude can have a large effect on the radiance. Uncertainties in the CIRRIS-1A pointing could also explain some or most of the differences. The tangent height uncertainty is estimated to be 1 to 2 km for these data.

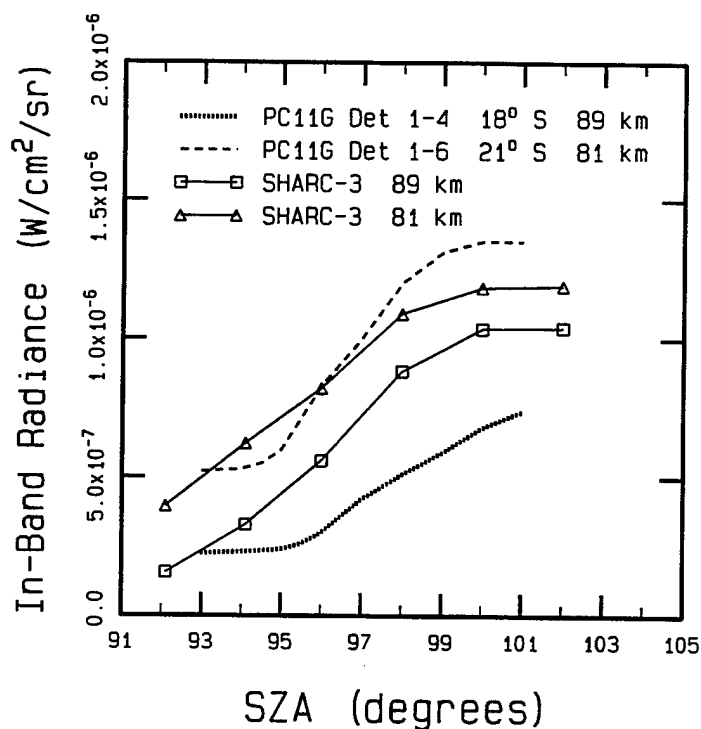


Figure 16. Calculated (SHARC-3) and Observed (CIRRIS-1A) O₃(v₃) Limb Radiances at the Dusk Terminator.

4.2.3 OH $\Delta V=1$

The OH $\Delta V=1$ Meinel band emission above 80 km is generated from the $H + O_3$ reaction. The H and O_3 concentration profiles have been discussed in Sections 3.1.4 and 3.1.6. The OH emission is expected to show a similar terminator behavior as the O_3 emission, since the H atom concentration should not vary across the terminator at these altitudes. Not surprisingly, we find the SHARC/CIRRIS-1A data comparison for OH to be similar to that for O_3 .

4.2.3.1 Terminator OH Radiance

Figure 17 shows 2.5-3.4 μm bandpass data from CIRRIS-1A that were taken simultaneously with the O_3 data of Figure 16. The small quantity of emission at the lowest SZA's is from a blend of OH($\Delta V=1$) and CO_2 2.7 μm bands; the increase starting around 94° is ascribed entirely to OH(V) formed from the increasing quantity of ozone. The SHARC calculation yields slightly more OH emission than observed, but the difference is well within the variability of the OH emissions and the pointing uncertainty. The solar angle dependence of the data is also reproduced quite well; the location of the terminator edge appears to be accurate to within 2° or less of SZA.

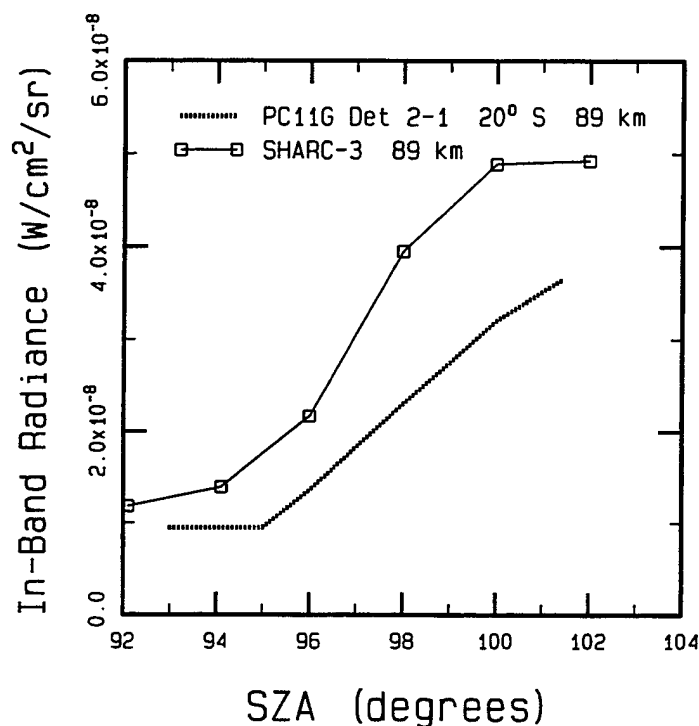


Figure 17. Calculated (SHARC-3) and Observed (CIRRIS-1A) OH($\Delta V=1$) Limb Radiances at the Dusk Terminator.

Since the concentration of ozone derived from the photochemical model is inversely proportional to the H atom concentration, the quantity of OH emission at night does not depend on the assumed H atom profile. However, it does depend on the O atom recombination rate, and hence on the O atom concentration as well as the mechanism and rate constants for OH(V) deactivation. Future refinements of the OH(V) kinetics in SHARC will provide a more precise relationship between the OH emissions and the recombination rate, so that these emissions could be used for deriving accurate O atom profiles in the mesopause region.

5. DEVELOPMENT OF SAMM

This section describes SAMM, a moderate spectral resolution (2 cm^{-1}) infrared (IR) atmospheric transmission and background radiance model applicable at altitudes from ground to space (300 km). SAMM,⁷⁶ SHARC⁶ And MODTRAN^{2,77} Merged, was developed by integrating the DOD standard lower atmosphere (2 cm^{-1} MODTRAN) and upper atmosphere (1 cm^{-1} SHARC) moderate spectral resolution models into a single, seamless code with a unified and correlated radiative transport algorithm. This section provides an overview of the SAMM model. A more detailed discussion which describes how to run SAMM by providing code implementation and execution instructions can be found in the SAMM User's Manual.⁷⁶ It also discusses the newly developed radiative transport algorithm which is applicable to both the low and high altitude regimes.

5.1 Overview

SAMM is a model for predicting spectral radiances for selected lines-of-sight (LOS) through the atmosphere. In SAMM, the earth's atmosphere from 0 to 300 km altitude is partitioned into a single extended ambient region and localized ambient and/or auroral sub-regions. The aurora are regions whose chemistry is influenced by the bombardment of solar electrons; specification of the incident electron energy spectrum and its duration is required for modeling these aurora. Both ambient and auroral localized regions are bounded by surfaces of constant altitude, latitude, and longitude. Within each region, the user may define/select either a single set of pressure, temperature, and total molecular density profiles or multiple sets, each one associated with a particular solar earth center angle (solar earth center angle is used rather than solar zenith angle, because the former is not affected by spherical refractive geometry and therefore is altitude independent at a fixed latitude and longitude).

In addition to generic atmospheric profiles supplied with SAMM, additional atmospheric profiles can be generated using the SAG program (see Section 3). Aerosol profiles are not defined in the atmospheric profile files, but instead are defined in an external file; these profiles use the MODTRAN/LOWTRAN 7 format, and they must be entered or modified by directly editing the aerosol file.

Solar position is specified either by directly entering solar latitude and longitude or by selecting year, month, day, and Greenwich mean time.

There are three basic LOS types: observer-to-source, observer-to-space, and limb viewing. For both the observer-to-source and the observer-to-space paths, the observer location is defined by entering the observer altitude, latitude, and longitude. There are five options for specifying source location; input (1) source altitude and observer zenith & azimuth, (2) path range and observer zenith

& azimuth, (3) source altitude, path range, and observer azimuth, (4) source altitude, path earth center angle, and observer azimuth, or (5) source altitude, latitude & longitude. For paths to space, the observer altitude, and either the observer zenith or the tangent altitude must be input. Limb viewing LOS are tangent paths extending from space to space; these paths are specified by entering the tangent point altitude, latitude, longitude & azimuth. For all paths, azimuth angles can be specified either by directly entering the angle (degrees East of North) or by entering a latitude and longitude in front of or behind the observer (tangent point for limb paths) location.

All spectral data are entered in wavenumber (cm^{-1}) units. The spectral range of SAMM is 250 to $10,000 \text{ cm}^{-1}$ and the minimum spectral resolution is 1 cm^{-1} .

5.1.1 Refractive Geometry

The refractive geometry model calculates all required refractive paths for SAMM. The basic refractive geometry equation is

$$n_R R \sin\theta = \text{constant} \quad (15)$$

where R is the earth center distance, n_R is the real part of the refractive index, and θ is the zenith angle at R . The assumption is made that the refractive path varies insignificantly with wavelength, and refractive geometry calculations are performed for the central frequency of the spectral bandpass only. A second assumption is that the refractive index is constant above 30 km i.e., at low pressures, and straight line geometry is used for the 30 to 300 km altitude region.

Refractive paths are tracked by marching along from the initial location to the termination point. It is necessary that the altitude, latitude, longitude, path zenith, and path azimuth at the initial location all be known. If this LOS starting point information is not actual input (e.g., if path range instead of zenith angle is used to specify an observer-to-source path), then the model solves for the required initial data, directly if possible and iteratively when necessary.

Output from the model includes column densities and layer averages for both optical and scattering point-to-sun paths below 30 km. A new algorithm has been developed to calculate these quantities directly from the layer path length and boundary zenith angles, altitudes, and densities.⁷⁶

5.1.2 Column Densities

The column density information is obtained from the relevant MODTRAN and SHARC algorithms. MODTRAN determines all the lower altitude ($< 30 \text{ km}$) total molecular column densities; for radiators common to both MODTRAN and SHARC (H_2O , CO_2 , CO , NO , O_3 & CH_4), densities must be partitioned into their vibrational states. At higher altitudes, the SHARC column densities are combined with the MODTRAN path amounts for HNO_3 , SO_2 , NO_2 , NH_3 , N_2O , O_2 , and the aerosols.

5.1.3 Radiative Transfer Model

The radiative transfer model is based on a modification to the MODTRAN radiative transport routines, and calculates and outputs spectral radiances. The spectral bandpass is sampled in 1 cm^{-1} steps. The resulting 1 cm^{-1} data is internally degraded using a digitized triangular slit function if the user requests a FWHM (Full Width at Half Maximum) in excess of 1 cm^{-1} .

For each frequency, there is a loop over the optical path layers to determine their contribution to the spectral radiance. Single scatter solar/lunar radiance is included in the layer radiances by considering the contribution from L-shaped paths from the sun/moon to the layer to the observer. The multiple scattering contribution to the spectral radiance is determined by initially performing a two-flux calculation at each frequency; the required upward and downward fluxes are calculated by looping over the atmospheric layers below 100 km using a vertical path from ground to space. Details of the radiance algorithm are presented in Section 5.2

5.2 Radiation Transport Algorithm

In the lower atmosphere, below 30 km altitude, collisional processes dictate the distribution of the dominant vibrationally excited species, i.e., LTE conditions prevail. At higher altitudes, where densities are much lower, radiative pumping and spontaneous emission processes can begin to compete with the collisional processes. The deviation from LTE depends on details of the excitation reactions and varies from one molecular band to another. When the ambient temperature no longer describes the distribution of vibrationally excited states, a molecular band is said to be in non-local thermodynamic equilibrium (non-LTE). Transmittances and radiances then depend explicitly on these vibrational distributions.

5.2.1 Line-of-Sight Radiance

Computation of the spectral radiance for an atmospheric line-of-sight (LOS) passing through both the LTE and non-LTE regimes requires detailed information about gas kinetic temperature, pressure, species column densities, vibrational populations, solar irradiance, and surface temperature. SHARC calculates these radiances by modeling non-LTE formation processes and then performing LBL calculations, while MODTRAN uses an LTE band model approach. SAMM has adopted a hybrid approach in which the SHARC radiators (CO_2 , H_2O , O_3 , CO , OH , CH_4 , NO , & NO^+) are treated LBL and all other emitters (N_2O , O_2 , SO_2 , NO_2 , NH_3 , HNO_3 , & continuum sources) are modeled using the MODTRAN band model techniques. The LOS is represented as a series of segments, and the radiance within each (1 cm^{-1}) spectral bin is calculated as the sum of emission I^0 , single scattering I^{ss} , and multiple scattering I^{ms} terms:

$$I = \sum_{\ell} I_{\ell}^0 + I_{\ell}^{\text{ss}} + I_{\ell}^{\text{ms}}, \quad (16)$$

where the sum is over the atmospheric layers traversed by the LOS. The emission from each layer is calculated as a product of the incremental transmittance $\tau_{\ell-1} - \tau_{\ell}$, one minus layer scattering albedo $1 - \omega_{\ell}$, and a source term R_{ℓ} :

$$I_{\ell}^0 = (\tau_{\ell-1} - \tau_{\ell}) (1 - \omega_{\ell}) R_{\ell} . \quad (17)$$

The τ_{ℓ} are the transmittances from the observer to the far side of layer ℓ . These calculations are done at each wavenumber or spectral bin increment. Since MODTRAN is an LTE model, its source term is simply the Planck blackbody function. SAMM models both LTE and non-LTE radiators by defining the source term as an average over the individual sources (j) weighted by their incremental spectral bin equivalent widths, $\Delta W_{\ell j}$ ($= W_{\ell j} - W_{\ell-1,j}$):

$$R_{\ell} = \frac{c_1 v^3}{\pi} \sum_j \Delta W_{\ell j} \left(\frac{\rho_{\ell j}'}{\rho_{\ell j} - \rho_{\ell j}'} \right) / \sum_j \Delta W_{\ell j} , \quad (18)$$

where c_1 is the first radiation constant ($c_1 = 2\pi h c^2$, h is the Planck constant and c is the speed of light), v is the spectral bin frequency, and $\rho_{\ell j}'$ & $\rho_{\ell j}$ are the densities of the upper & lower states, respectively. The sources of emission being summed over include SHARC molecular transitions, MODTRAN band model lines for non-SHARC species, and the MODTRAN continuum sources. This expression for the source term reduces to the blackbody function under LTE conditions, is exact in the weak line limit, and gives greatest weight to the strongest absorber in a given layer along the LOS. The equivalent width for each spectral bin is defined as a species' absorption within that bin and is given by

$$W_{\ell j} = \int_{\Delta v} dv \left[1 - \tau_{\ell j}(v) \right] , \quad (19)$$

where $\tau_{\ell j}$ is the spectral transmission through layer ℓ for absorber j and Δv is the width of the spectral bin.

The spectrally averaged transmission arising from an ensemble of absorbers centered randomly within the spectral interval is given by

$$\tau_{\ell} = \prod_j \left(1 - \frac{W_{\ell j}}{\Delta v} \right) . \quad (20)$$

This equation implicitly includes the statistical correction for random line overlap.⁷⁸ Both the single line and band model equivalent widths for a Voigt lineshape are evaluated using the Rodgers and Williams^{33,79} (RW) interpolation formula. This formula has been shown to give a peak error of 8%. The Lorentzian line tails are subtracted from the RW expression to obtain the Voigt equivalent width within a spectral bin.² This correction is important for lower altitudes where the total equivalent

width of a strong line can easily exceed the typical bin width of 1 cm^{-1} . The RW interpolation formula requires evaluation of equivalent widths in the Lorentz, Doppler, and weak-line limits. Standard approximations³² involving Curtis-Godson^{2,79} path averages are used to evaluate these widths. Curtis-Godson path averages are used to approximate paths through multiple layers by a single homogeneous path.

An upgraded formulation for the single scattering solar radiance has been integrated into both MODTRAN and SAMM. The single scatter component can be written

$$I_{\ell}^{ss} = \pi F^{sun} \int_{\tau_{sct \ell}}^{\tau_{sct \ell-1}} \frac{P_{\ell}}{4\pi} \tau_{abs}^L(\tau) \tau_{sct}^{sun}(\tau) d\tau. \quad (21)$$

F^{sun} is the extraterrestrial solar flux and P_{ℓ} is the scattering phase (angular cross-section) function. Since the variation in scattering angle along the LOS is negligible, a layer averaged phase function can be factored out of the integral. The question remains as to how the L shaped path (observer to scattering point to sun) transmittance from absorption varies with the LOS scattering transmittance. In deriving an expression for the layer thermal emission, Cornette⁸⁰ assumed that transmission from absorption and scattering both varied exponentially across a layer. This is equivalent to the assumption of equal effective absorption and scattering scale heights within a layer. We similarly assume that

$$\tau_{abs}^L(\tau) = \tau_{abs \ell-1}^L \left[\frac{\tau_{abs \ell}^L}{\tau_{abs \ell-1}^L} \right]^z \quad (22)$$

where

$$z = \frac{\ln [\tau / \tau_{sct \ell-1}]}{\ln [\tau_{sct \ell} / \tau_{sct \ell-1}]} \quad (23)$$

With this assumption, the single scatter solar integral can be evaluated analytically yielding

$$I_{\ell}^{ss} = \frac{F^{sun} P_{\ell}}{4} \ln\left(\frac{\tau_{sct \ell-1}}{\tau_{sct \ell}}\right) \frac{\tau_{\ell-1}^L - \tau_{\ell}^L}{\ln [\tau_{\ell-1}^L / \tau_{\ell}^L]}. \quad (24)$$

The first logarithm term equals the layer scattering optical depth, and the final term can be interpreted as an averaged L shaped path total transmittance divided by the extinction (absorption plus scattering) layer optical depth.

In MODTRAN and hence SAMM, the molecular and aerosol single scatter solar radiance contributions are treated separately. The total single scatter solar radiance is a sum of the two terms. Three choices are available for the aerosol phase function: user-supplied, Henyey-Greenstein, or Mie generated internal database.⁷⁷ The L shaped path transmission terms, τ_ℓ^L , are calculated for all the SHARC and MODTRAN absorbers, rigorously determining the column density through the multiple higher altitude regions.

The MODTRAN LTE treatment of multiple scattering

$$I_\ell^{ms} = (\tau_{\ell-1} - \tau_\ell) \omega_\ell \left[(1 - \beta_\ell) F_\ell^\mp + \beta_\ell F_\ell^\mp \right] / \pi, \quad (25)$$

has not been altered because multiple scattering is only significant at the lower altitudes where LTE conditions prevail. At each layer boundary, the upward and downward fluxes, F_ℓ^\pm , the scattering albedo, ω_ℓ , and the backscatter fraction, β_ℓ , are calculated. The two flux calculation, which uses a vertical path, is performed for the atmosphere defined at the observer's latitude and longitude and with its high altitude boundaries fixed at 30, 35, 40, 45, 50, 70, and 100 km; multiple scattering is not included above 100 km. When multiple scattering is not requested, the scattering albedo in Eqs. (17) and (25) is set to zero.

5.3 Low Altitude Solar Attenuation

Since SHARC-3, MODTRAN and SAMM calculate LOS radiances in the region of the solar terminator, solar zenith angles that are greater than 90° must be accommodated. Under these conditions, the solar irradiance passes through parts of the atmosphere that are below the lower boundary of the chemical kinetics module (50 km in SHARC-3, 30 km in SAMM). Since some of this radiation is absorbed by the lower atmosphere, its intensity, and spectral structure are modified. The amount of absorption at any wavenumber is a function of the solar zenith angle, or equivalently the minimum altitude through which the sunlight passes, and of the aerosol and molecular content of the lower atmosphere.

SHARC and SAMM distinguish the attenuation of solar irradiance by "line center" and "continuum" sources. Both codes model the line center attenuation of solar irradiance by performing LBL calculations for each vibrational transition. Curtis-Godson averages are used to define Doppler and collision broadened half-widths for the solar paths. The "continuum" sources here denote all sources of absorption other than the particular vibrational band under consideration.

5.4 Representative Calculations

SAMM has been validated by extensive comparisons with SHARC and MODTRAN and a database⁸¹ containing selected CIRRIS-1A radiance profiles and spectra. The CIRRIS-1A data base was assembled to assist in the validation of atmospheric IR radiation codes. The simulations using SAMM were based on model atmospheres are from SAG. Rather than reproduce the numerous comparisons here, we simply show two comparisons of SAMM with calculations from SHARC and MODTRAN. The more extensive comparisons can be found elsewhere.^{76,81}

The first example consists of a nighttime 80 km limb calculation including emission from all seven SHARC radiators, but with none of the MODTRAN only radiators. The SAMM and SHARC-3 results are compared at the same spectral resolution in Figure 18. A more detailed comparison illustrates that the only significant differences arise for the $7.65\text{ }\mu\text{m}$ CH_4 band. Since SHARC-3 and SAMM use different lower boundaries for solving the chemical kinetics equations (50 km in SHARC-3 and 30 km in SAMM), they predict different amounts of earthshine pumping. Generally these differences are small. The $7.65\text{ }\mu\text{m}$ CH_4 band is an exception in this case. Preliminary comparisons to CIRRIS data seem to indicate better agreement with SAMM, but these results are inconclusive due to uncertainties in the methane profile.

The second example is a low altitude daytime calculation (limb LOS tangent at 10 meters altitude) with all SHARC and MODTRAN radiators and aerosols. The SAMM combined LBL/band model results are compared to the MODTRAN band model only results in Figure 19. Solar and thermal single and multiple scattering is included in the calculations. Agreement is excellent in all regions except the center of the $4.3\text{ }\mu\text{m}$ band, where near field hot CO_2 significantly contributes to the spectral radiance.

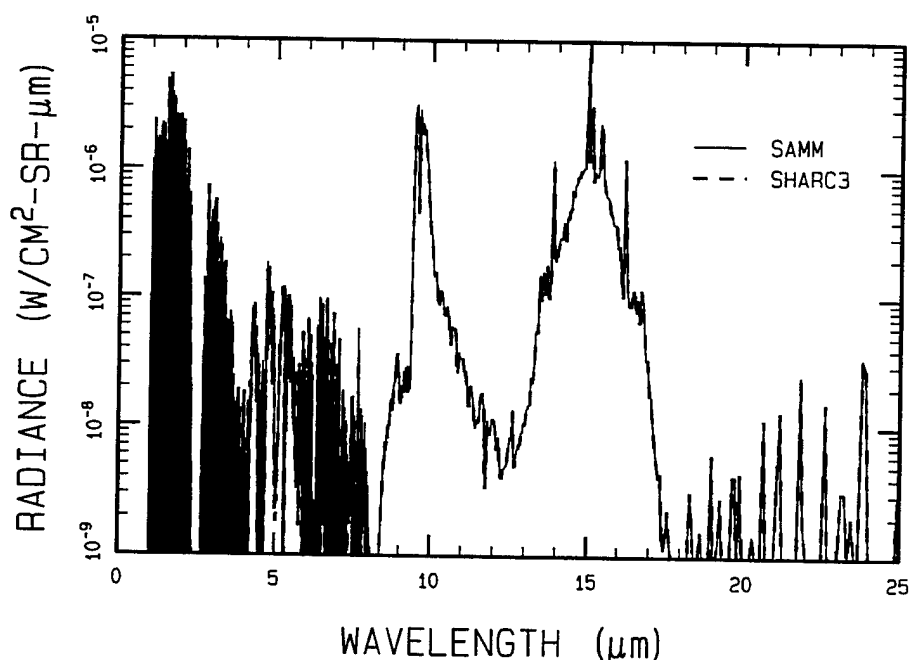


Figure 18. Comparison of SAMM with SHARC-3 for an 80 km Limb Path at Night.

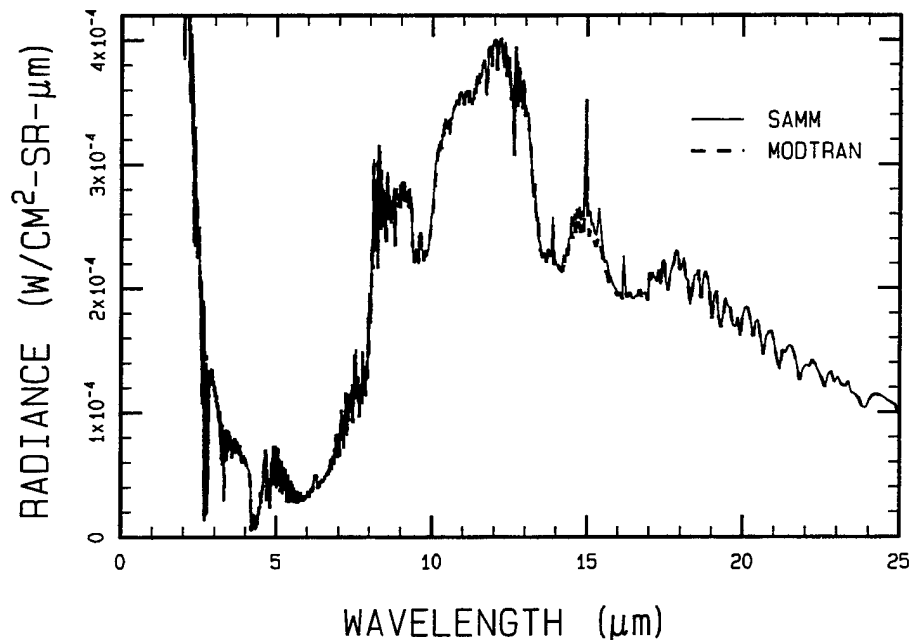


Figure 19. Comparison of SAMM with MODTRAN for a 10 km Limb Path.

6. DEVELOPMENT OF AN ATMOSPHERIC STOCHASTIC STRUCTURE MODEL

The calculation of infrared (IR) mean radiance, transmittance and their fluctuation statistics is important in many areas of atmospheric science, including the interpretation of satellite sensor measurements and understanding the effects of turbulence structures on molecular excitation processes. The atmospheric infrared radiance fluctuations depend on fluctuations in atmospheric species number densities, vibrational state populations, and the kinetic temperatures along the sensor line-of-sight (LOS). The standard SHARC model⁷ calculates mean LOS radiance and transmittance values. The SHARC structure model predicts the two-dimensional spatial covariance function of the radiance. The covariance function and its Fourier transform, the power spectral density (PSD), can be used directly in sensor models or in image synthesis modes to create realizations of the predicted structure. The radiance statistics and images are non-stationary and are explicitly bandpass and sensor FOV dependent.

This section describes the atmospheric stochastic structure model and investigates the effects of atmospheric variability due to diurnal and latitudinal conditions on the resultant radiance and radiance statistics for the SWIR (2.7 μm) and MWIR (4.3 μm) spectral regions. The results are summarized in terms of radiance statistical quantities, such as the correlation lengths, standard deviations, and the slope of the radiance power spectral density (PSD). Since the most important input to the SHARC-4 structure model is the temperature fluctuation model, additional variations to the input temperature statistical parameters were performed in an attempt to isolate any dominate effects. However, due to the uncertainties in the temperature model, any sensitivity study should be considered with several caveats.

First, the nominal values of the first- and second-order statistical parameters used in temperature fluctuation model were extracted from several sources. The uncertainties or error bars have not been

established. Most of the measurements were of density fluctuations or radiance fluctuations with temperature statistics inferred. There is large variability in the temperature fluctuation statistics in the lower altitudes which the current model does not capture as it was not extended down below 10 km altitude. Furthermore, there is no diurnal, latitudinal, or seasonal variation included in the temperature fluctuation model. It is not at all clear that doubling or halving quantities such as correlation lengths or variances brackets actual values. The study should provide insight into the role each parameter has on basic predictions of radiance statistics, but by no means can be considered completely inclusive.

An additional assumption of the base line temperature model is that the underlying stochastic process is a Gaussian Markov process with a Gaussian PDF and exponential covariance. Further, for image generation, random phases are explicitly assumed. Different stochastic processes with the same overall first- and second-order statistics (means, variances, correlation lengths) could differ widely in terms of gradient or clutter properties. Gravity waves, which are believed to be a principal source of structure, are known to break, and hence contribute structure at multiple scales; the large amplitude, large length scale non-turbulent mode, and the turbulent mode, where length scales are much shorter than in the non-turbulent mode. The assessment of these issues await analysis of future measurements of atmospheric structure.

6.1 Stochastic Structure Overview

For atmospheric altitudes less than 50 km, collisional quenching of excited vibrational states is generally fast compared to radiative decay. Species tend to be in local thermodynamic equilibrium (LTE) and state populations can be determined from a Boltzmann distribution at the gas-kinetic temperature. At higher altitudes, there are an insufficient number of collisions to equilibrate vibrational energy before radiative decay occurs and the vibrational states can no longer be characterized by the kinetic temperature. Under these conditions, the vibrational states are in nonlocal thermodynamic equilibrium (NLTE). Models extending into the higher altitudes must describe these deviations from local thermodynamic equilibrium. SHARC assumes steady state kinetics for the atmospheric processes of collisional excitation, energy transfer, radiative decay, chemical production and illumination by the sun, earth and atmosphere. The model treats seven species which radiate in the 2-40 μm wavelength region, including NO, CO₂, O₃, H₂O, OH, CO, and CH₄, as well as the isotopes of CO₂ and H₂O. The number densities of the excited vibrational states are predicted and can be described in terms of a Boltzmann distribution with state dependent vibrational temperatures. Under LTE conditions, the response of the vibrational states to a kinetic temperature fluctuation can be described by a Boltzmann distribution corresponding to the new kinetic temperature. The emission from a small volume in the atmosphere depends only on the gas-kinetic temperature in that volume and is determined using the Planck blackbody emission source term at the new fluctuated temperature. Under NLTE conditions, the response of population changes to fluctuations in temperature and density are determined for each state by a perturbation model which uses the same steady state chemical-kinetics schemes that are used for the quiescent atmosphere. Fluctuations in the kinetic temperature can result in correlated or anti-correlated responses in vibrational state population. The magnitudes of the responses depend on the local chemical environment. NLTE emission depends on the vibrational temperatures of all species involved, as well as, the gas-kinetic temperature.

Fluctuations in atmospheric temperature and density have been measured directly using balloon, rocket, and satellite experiments. These experiments provide in-situ measurement of density, temperature and species concentrations. Ground based techniques used to determine atmospheric structure statistics include radar, lidar and airglow emission measurements. Taken together these measurements begin to provide the necessary structure statistics which characterize the atmosphere. Current estimates of these quantities have been summarized, in a 3-D non-stationary statistical model (NSS).⁸² The NSS model provides a covariance function, PSD description of atmospheric temperature and density fluctuations. Horizontal altitude layers are assumed to be isotropic and stationary, while the vertical variations are treated as non-stationary. Model parameters (variance, vertical correlation length, and horizontal correlation length) are described as a function of altitude. The NSS model currently assumes a 1-D PSD spectral slope of -2 for all altitudes.

A simulation of the radiance fluctuations observed by a sensor array can be calculated by using a three-dimensional realization of the atmospheric temperature and density fluctuations and by intersecting a LOS for each pixel with the 3-D realization to determine the LOS radiance for each pixel in the sensor.⁸³ Alternatively, the radiance statistics for the sensor FOV can be derived directly. The radiance statistical functions can be incorporated into sensor models, or image syntheses models, to create scenes consistent with the radiance statistics. The model described here proceeds with the later approach although the former approach is being used to evaluate the algorithms. The radiance statistics predicted by SHARC explicitly include radiance fluctuation contributions along the entire LOS and not just the tangent point. The inputs to the calculation are altitude dependent temperature and density profiles, which can be obtained from the standard atmosphere generator code (SAG), the local temperature and density statistical quantities obtained from the NSS model and an atlas of molecular line parameters based on HITRAN-92.¹⁷ The SHARC model calculates the non-stationary LOS radiance covariance by performing LOS integrations over the products of radiance fluctuation amplitude functions,⁸⁴ and the local kinetic temperature covariance. A key quantity derived by the model is a LOS radiance variance distribution function which determines the contribution to radiance variance of each portion of the LOS. The radiance variance distribution function acts as a weighting function, revealing the contributions of temperature and density fluctuations to the radiance variance along the LOS.

6.2 Radiance Structure Calculation Technique

The radiance structure of atmospheric backgrounds is induced by local temperature and density fluctuations in the atmosphere. The radiance in a pixel of an image plane $L_{\Delta\lambda}(\vec{p})$ in a bandpass $\Delta\lambda$, is given by

$$L_{\Delta\lambda}(\vec{p}) = \int d\lambda \int dr S(\vec{r}, \lambda) \partial\tau(\vec{r}, \lambda) / \partial r \quad . \quad (26)$$

where \vec{p} is a vector in the sensor plane defining the pixel location and the LOS from the observer is defined by the vector \vec{r} . The quantities $S(\vec{r}, \lambda)$ and $\tau(\vec{r}, \lambda)$ are the emission source term and the atmospheric transmittance, respectively, at wavelength λ and scalar distance r from the observer along the LOS. In the LTE approximation the source term is the Planck blackbody function at the

local atmospheric gas kinetic temperature, T_k . In The NLTE regime the source term is dependent on the non-equilibrium number densities of the molecular vibrational states involved in the bandpass.⁷ The populations of rotational states involved in the bandpass transitions are assumed to be in LTE. The non-equilibrium number densities can equivalently be expressed in terms of vibrational state temperatures, T_{vib} , whose deviation from the local kinetic temperature is a convenient measure of NLTE. Implicit in Eq. (26) is a sum over all species and their molecular vibrational/rotational states which emit in the bandpass, $\Delta\lambda$.

6.2.1 Vibrational State Temperature Fluctuations

The local temperature and density fluctuations specified in the NSS model induce fluctuations in the local vibrational state number densities. The influence of temperature and density enter into the chemical kinetic rate equations in a non-linear fashion. The collision rates are affected by temperature variations which alter rate constants and density variations which influence the number of collisions. The model predicts fluctuations in local vibrational state densities as a function of local temperature and density fluctuations. Temperature fluctuations cause two effects, a simple expansion or compression which changes state populations induced by local heating or cooling respectively, and the adjustment of vibrational/rotational state populations due to chemical kinetic mechanisms. The latter effect can be expressed in terms of fluctuations in vibrational and rotational state temperatures. In this work, the rotational states are considered to be LTE, so rotational temperatures and fluctuations map exactly with kinetic temperature fluctuations.

The fluctuation in local vibrational temperature for a particular vibrational state (say the j^{th} state) can be approximated as

$$\Delta T_{vib}^j = (\partial T_{vib}^j / \partial T_k) \Delta T_k + \dots \quad (27)$$

The proportionality constants, $(\partial T_{vib}^j / \partial T_k)$, are strongly dependent on altitude and are also far from the LTE value of unity when NLTE effects are important.

As an example, we illustrate the results of the NLTE kinetics model for determining the nighttime estimates of vibrational temperature and its response to temperature fluctuations for the CO_2 v_2 and v_3 fundamental transitions (see Figures 20 and 21). NLTE effects in vibrational state populations, and their linear response to fluctuations in temperature, occur for these states above 40 to 50 km. The NLTE effects in vibrational temperature are consistent with previous NLTE models and has been presented previously.⁷ Although vibrational temperature fluctuations have not been computed using other models, the fluctuations can be understood in terms of the same atmospheric processes determining the vibrational temperatures. In particular, the $\text{CO}_2(v_2)$ vibrational state involves collisional excitation by N_2 and O_2 which is dominate below 50 km in the LTE regime, and diminishes in importance above 100 km. Radiative pumping is important above 50 km and dominates between 80 km and 100 km corresponding to the minimum in $\partial T_{vib} / \partial T_k$ around 80 km, as shown in Figure 21. Above 90 km, O atom excitation of $\text{CO}_2(v_2)$ becomes increasingly important until ~150 km where again radiative excitation dominates. The behavior of the $\text{CO}_2(v_3)$ state is quite different than $\text{CO}_2(v_2)$. $\text{CO}_2(v_3)$ is LTE up to approximately 30 km, and becomes completely dominated by radiative excitation by 50 km up to an altitude of 100 km. Although

vibrational-to-vibrational energy transfer between CO_2 and N_2 is the most important mechanism between 110 and 170, there are not sufficient collisions to provide significant variations in the vibrational temperature in this altitude regime. Clearly, the altitude variations of the vibrational temperatures in response to temperature fluctuations will have a profound effect on the radiance fluctuations.

As mentioned earlier, a convenient description of the temperature fluctuation statistics is provided by the NSS model,⁸² which is used in the present work. The parameters which characterize the model are the temperature variance, vertical correlation length, and horizontal correlation length, as well as the slope of the PSD. These parameters (excluding the PSD slope) describing the temperature statistics are all altitude dependent, and are shown in Figures 22 - 24. The horizontal correlation length is greater than 10 km above an altitude of 30 km, increasing with altitude to a value of ~ 70 km above 150 km. However, the vertical correlation length varies from 1 km to 2.5 km in the altitude regime of 10 km to 120 km, illustrating that the radiance statistics are expected to be highly non-stationary in the vertical direction. The relative standard deviation varies from approximately 2% to 20 % over the altitude regime of 10 km to 120 km, indicating that the largest temperature variability will affect the higher altitude radiance.

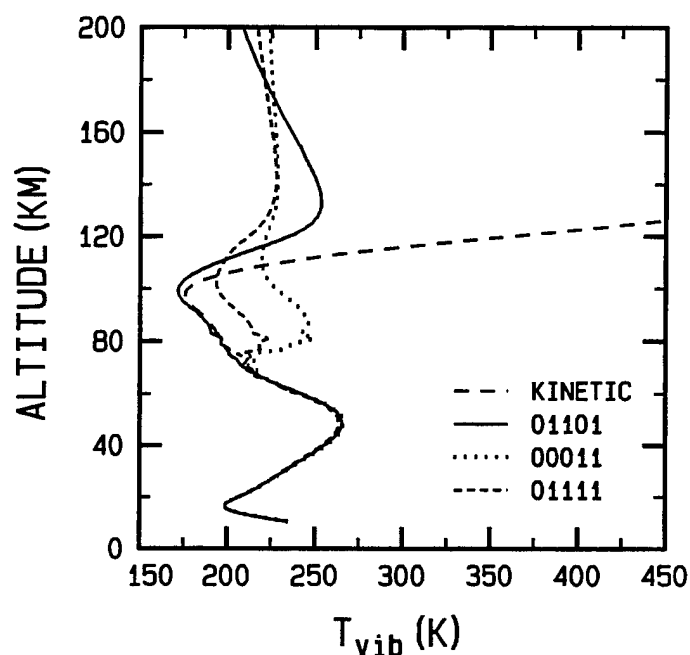


Figure 20. Altitude Profile of the Atmospheric Kinetic Temperature and Vibrational Temperatures of Selected States of CO_2 for Nighttime Conditions.

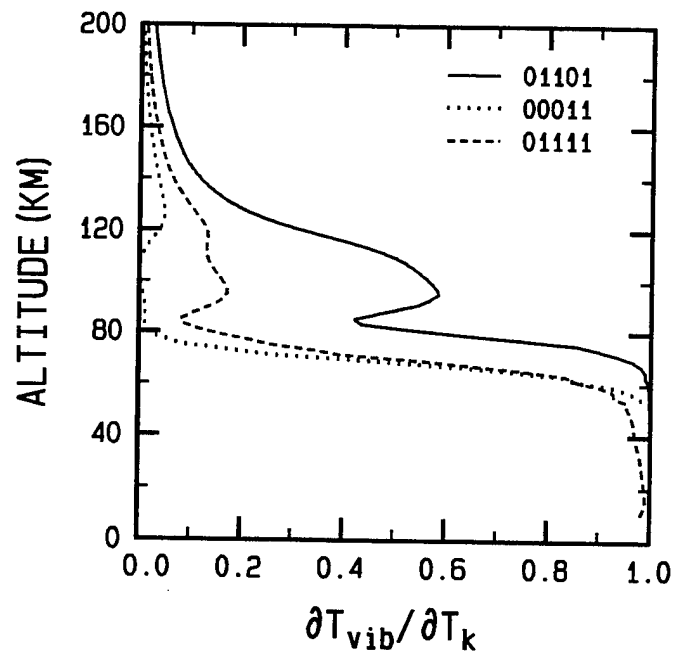


Figure 21. Partial Derivatives of Vibrational Temperature with Respect to Kinetic Temperature as a Function of Altitude for Selected States of CO₂ for Nighttime Conditions.

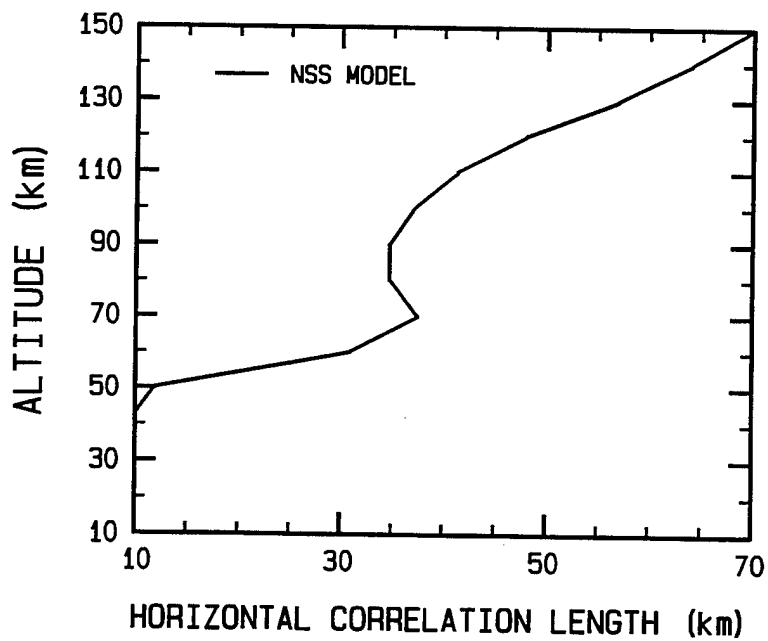


Figure 22. Altitude Dependence of the Temperature Horizontal Correlation Length for the NSS Stochastic Model.

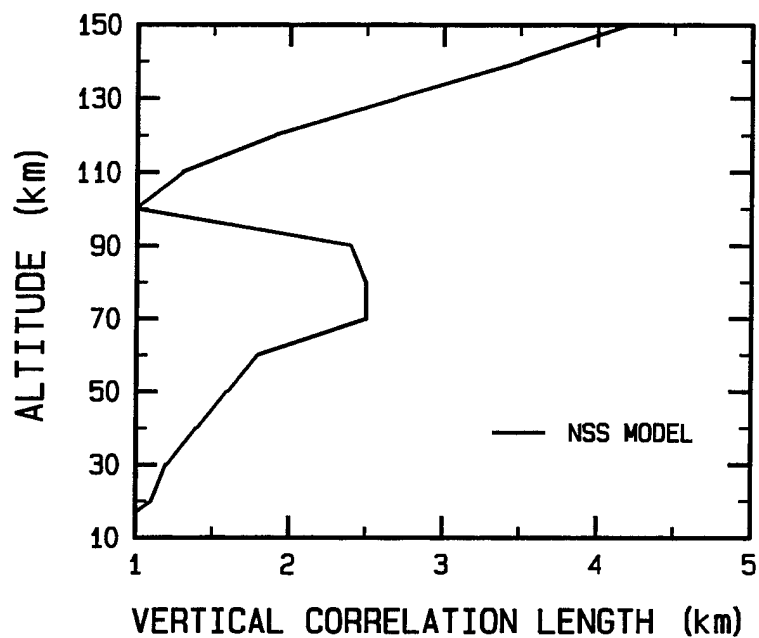


Figure 23. Altitude Dependence of the Temperature Vertical Correlation Length for the NSS Stochastic Model.

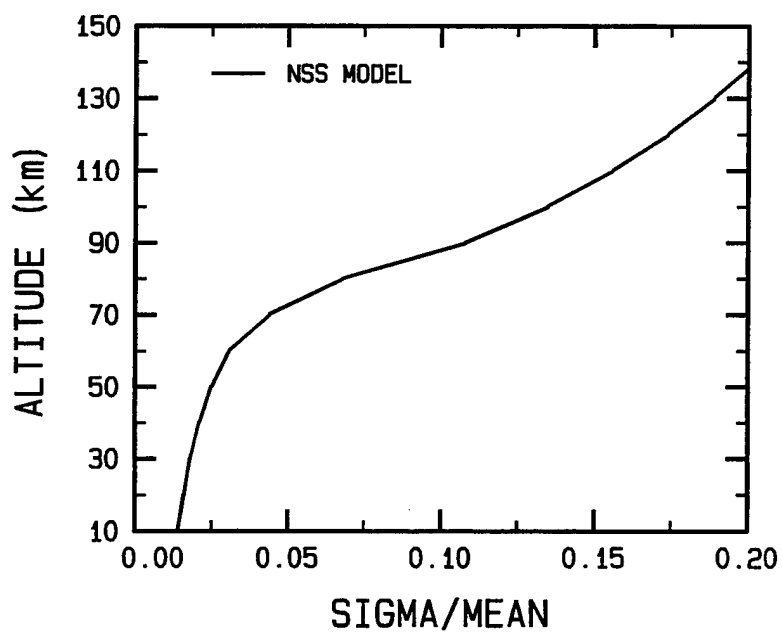


Figure 24. Altitude Dependence of the Temperature Relative Standard Deviation for the NSS Stochastic Model.

6.2.2 Radiance Covariance

A fluctuation in radiance is approximated using the leading terms of a Taylor series expansion in terms of the vibrational state temperatures and the atmospheric temperature.

$$\Delta L_{\Delta\lambda}(\vec{p}) = \int d\vec{z} \left\{ \sum_j F_{\Delta\lambda}^j(\vec{r}) \Delta T_{vib}^j + F_{\Delta\lambda}^0(\vec{r}) \Delta T_k \right\} + O[(\Delta T_k)^2] \quad (28)$$

The $F_{\Delta\lambda}^j$ and $F_{\Delta\lambda}^0$ are local LOS fluctuation amplitude functions. The radiance fluctuations induced by the rearrangement of population among the molecular vibrational states, j , is given by

$$F_{\Delta\lambda}^j(\vec{r}) = \int d\lambda \partial[S(\vec{r}, \lambda) \partial\tau(\vec{r}, \lambda)/\partial\vec{r}] / \partial T_{vib}^j \quad (29)$$

The radiance fluctuation induced by population shifts among rotational states, which are assumed to be in LTE, and the expansion or compression of the gas is given by

$$F_{\Delta\lambda}^0(\vec{r}) = \int d\lambda \partial[S(\vec{r}, \lambda) \partial\tau(\vec{r}, \lambda)/\partial\vec{r}] / \partial T_k \quad (30)$$

Only the linear terms in Eqs. (27) and (28) are retained to make a direct estimate of the radiance statistics.⁸⁵ The present work is an extension of a previous LTE approach (where it is assumed that $\partial T_{vib}^j / \partial T_k = 1$) used to determine atmospheric radiance statistics in the lower atmosphere.⁸⁴ For conditions under which NLTE effects are expected to be important (see Figures 20 and 21), the present approach properly incorporates the collisional and radiative effects. In particular, as the altitude increases to the point where collisions are no longer important, $F_{\Delta\lambda}^j \rightarrow 0$ since $\partial T_{vib}^j / \partial T_k \rightarrow 0$. Clearly, this limit can only be treated using the NLTE approach.

The expression for a radiance fluctuation can be simplified in the linear approximation to

$$\Delta L_{\Delta\lambda}(\vec{p}) = \int d\vec{r} F_{\Delta\lambda}(\vec{r}) \Delta T_k \quad , \quad (31)$$

where $F_{\Delta\lambda}(\vec{r})$ includes radiance fluctuation contributions from both vibrational state temperature fluctuations and kinetic temperature fluctuations,

$$F_{\Delta\lambda}(\vec{r}) = \sum_j F_{\Delta\lambda}^j(\vec{r}) \partial T_{vib}^j / \partial T_k + F_{\Delta\lambda}^0(\vec{r}) \quad . \quad (32)$$

The fluctuation amplitude is a linear response model for radiance fluctuations in terms of gas kinetic temperature fluctuations. This model can be coupled with a statistical model for non-stationary atmospheric temperature fluctuations to obtain a statistical non-stationary description of radiance fluctuations.

The basic quantity computed in the present approach is the radiance covariance function, which is a measure of the correlation of fluctuations about the mean at two points in space. The radiance covariance $Cov_L(\vec{p}_1, \vec{p}_2)$, where \vec{p}_1 corresponds to point 1 and \vec{p}_2 to point 2 in the sensor plane (as illustrated in Figure 25), can be expressed as

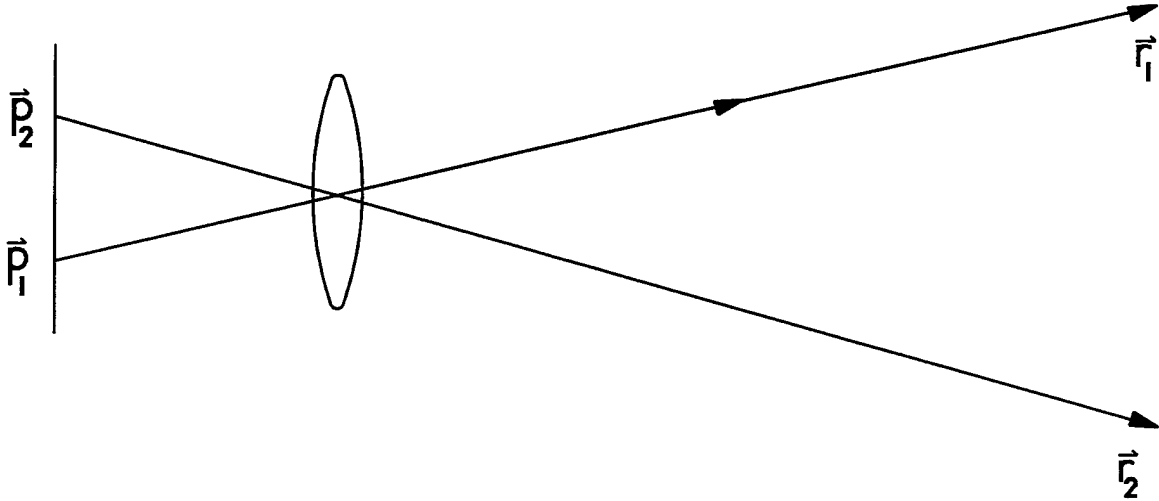


Figure 25. Schematic of Sensor Image Plane, Optics, and Two LOS Extending into the Atmosphere.

$$Cov_L(\vec{p}_1, \vec{p}_2) = E[\Delta L_{\Delta\lambda}(\vec{p}_1) \Delta L_{\Delta\lambda}(\vec{p}_2)] \quad , \quad (33)$$

where E is the expectation (average) value of the product (i.e., correlation) of the fluctuations about the mean at \vec{p}_1 times the fluctuations about the mean at point \vec{p}_2 . Substituting Eq. (31) into Eq. (33) yields

$$Cov_L(\vec{p}_1, \vec{p}_2) = \int d\vec{r}_1 \int d\vec{r}_2 F_{\Delta\lambda}(\vec{r}_1) F_{\Delta\lambda}(\vec{r}_2) Cov_T(\vec{r}_1, \vec{r}_2) \quad (34)$$

where the quantity $Cov_T(\vec{r}_1, \vec{r}_2)$ is the temperature covariance function given by the NSS model. The radiance variance, $\sigma_L^2(\vec{p})$, is determined by setting $\vec{p}_1 = \vec{p}_2$ (and therefore \vec{r}_1 and \vec{r}_2 are colligned) in Eq. (34)

$$\sigma_L^2(\vec{p}) = \int d\vec{r} \int d\vec{r}' F_{\Delta\lambda}(\vec{r}) F_{\Delta\lambda}(\vec{r}') Cov_T(\vec{r}, \vec{r}') \quad (35)$$

Eq. (35) shows the dependence of the radiance variance on the atmospheric temperature covariance along the LOS direction. Integration over one of the variables in Eq. (35) leads to a LOS variance distribution function, or weighting function, $w_{\Delta\lambda}(\vec{r})$,

$$\sigma_L^2(\vec{p}) = \int d\vec{r} w_{\Delta\lambda}(\vec{r}) \quad (36)$$

where

$$w_{\Delta\lambda}(\vec{r}) = \int d\vec{r}' F(\vec{r}') F(\vec{r}) Cov_T(\vec{r}, \vec{r}') \quad (37)$$

The variance distribution function determines how contributions to the radiance structure are distributed along the LOS through the atmosphere. The area under the distribution curve is the radiance variance at the pixel location \vec{p} . The variance distribution function, $w_{\Delta\lambda}$, can be evaluated numerically or it can be estimated by an approximation suggested by Lindquist, Kwon, and Nagy.⁸⁶ If the radiance fluctuation amplitude is a slowly varying function of location along the LOS, the product $F(\vec{r}_1)F(\vec{r}_2)$ can be replaced by the product of the radiance fluctuation amplitudes, $F(\vec{r})^2$, at the midpoint location, \vec{r} , and taken outside of the integral yielding

$$w_{\Delta\lambda}(\vec{r}) = \sigma_T^2 F_{\Delta\lambda}(\vec{r})^2 l_r(\vec{r}) \quad (38)$$

where the integral of the temperature covariance function yields the temperature variance, σ_T^2 , times the temperature correlation length along the LOS direction, $l_r(\vec{r})$. For this approximation to be valid, the local bandpass LOS weighting functions, F , must be slowly varying over the range of a temperature correlation length. Current estimates for the LOS weighting function are slowly varying compared to LOS temperature correlation lengths estimated using the NSS model. As a second test of Eq. (38), numerical integration of Eq. (37) using assumed functional forms for the temperature covariance suggest that the integral is independent of the functional form of the covariance and provides results within a few percent of Eq. (38). The covariance weighting functions, $w_{\Delta\lambda}$, is evaluated numerically by SHARC. The role of the spatial statistics of the 3-D temperature structures is revealed through the radiance variance distribution function. The temperature correlation length along the LOS direction controls the extent to which temperature fluctuations are averaged by LOS radiation transport. The temperature correlation lengths perpendicular to the LOS determine the spatial radiance statistics in the sensor plane. The statistical properties of the radiance fluctuations such as correlation angles or lengths can be determined directly from the covariance function, or they can be approximated using the variance distribution function.⁸⁵

The variance distribution function, Eq. (37), contains the information on the atmospheric response to the kinetic temperature fluctuations along the LOS. As an example, consider the latitude and diurnal variability of the variance distribution function in MWIR and SWIR spectral regions, respectively. To investigate the effects of latitude variability, high latitude subarctic and equatorial atmospheres were generated using the SAG model for moderate geophysical conditions. The major difference in the atmospheric profiles are in the kinetic temperatures in the stratopause and mesopause, with the subarctic atmosphere displaying a warmer stratopause (~ 20 K) and a cooler mesopause (~ 50 K). This effect is illustrated in Figure 26 in the MWIR spectral region for 100 km limb, which shows that the radiance statistics for the subarctic atmosphere is strongly dependent on altitudes greater than 100 km (the tangent point), while for the equatorial atmosphere the tangent point at 100 km determines the statistics. Interesting diurnal effects are also reflected in the variance distribution function, as shown in Figure 27 in the SWIR spectral region for a 60 km limb. For nighttime conditions, this bandpass is dominated by the radiance distribution function between 80 and 90 km corresponding to the OH layer. During the day, a contribution from the tangent point at 60 km results from H_2O , in addition to the OH contribution near 80 km. These examples clearly show the strength of the linear response approach to atmosphere structure, in that the variance distribution functions indeed provide an interpretation of atmospheric radiance structure.

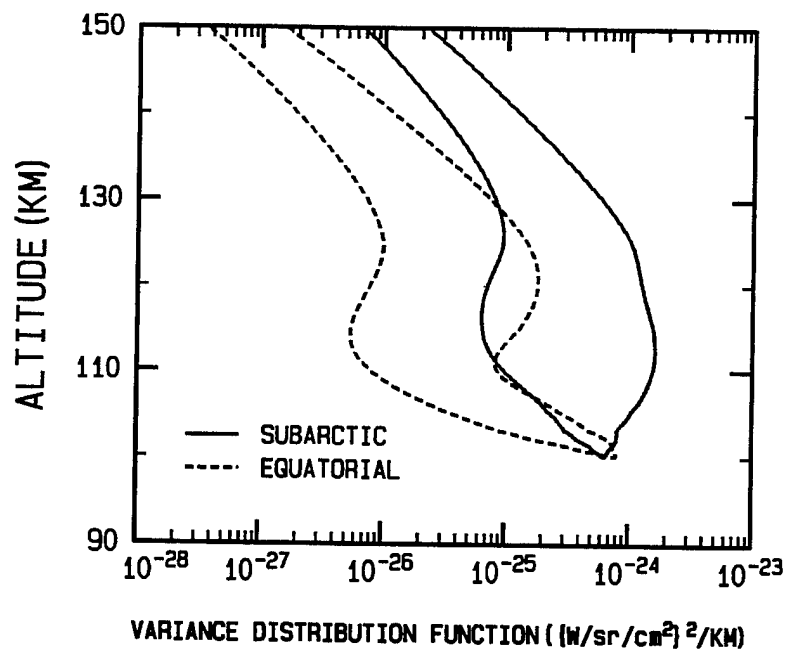


Figure 26. Effect of Latitude on the Altitude Dependence of the Variance Distribution Function for a 100 km Limb Under Nighttime Conditions in the MWIR Spectral Region.

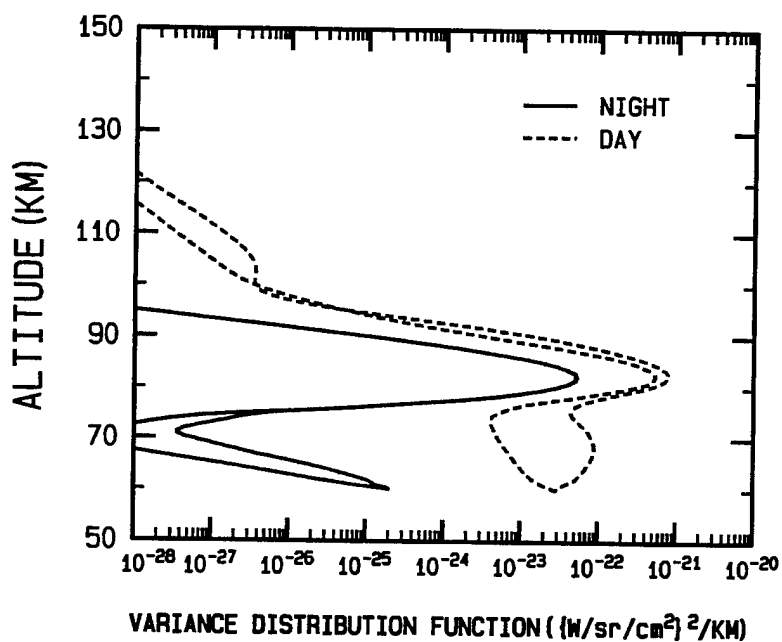


Figure 27. Diurnal Variation of the Altitude Dependence of the Variance Distribution Function for a 60 km Limb Under Nighttime Conditions in the SWIR Spectral Region.

6.2.3 Image Synthesis

The bandpass dependent simulation of the radiance fluctuations observed by an imaging sensor is calculated by generating a three-dimensional realization of the atmospheric temperature and density fluctuations and by intersecting a LOS for each pixel with the 3-D realization to determine the LOS radiance for each pixel in the sensor.⁸³ The model uses Fourier techniques to generate (isotropic) horizontal correlations and an auto-regressive (AR) method to synthesize vertical non-stationary correlations. The input temperature power spectral density (PSD) function is assumed to have a vertical slope of -3 and a horizontal slope of -5/3, consistent with the present understanding of atmospheric structure due to gravity waves. These values of the temperature PSD slope differ somewhat from the value of -2 used in the NSS, although the remaining temperature statistics parameters (variance and correlation lengths) are based upon the NSS model. The resultant data base of temperature and density fluctuations has been used to generate temperature images which have been shown to be consistent with the input temperature statistical model.⁸³

The fluctuation amplitudes, which give the response of the radiance to temperature and density fluctuations, are computed by SHARC as a function of limb altitude from 50 to 300 km in the bandpass of interest. The structured radiance field can then be constructed from the fluctuation amplitudes and 3-D realization of the temperature and density fluctuations. Line-of-sight integrations are then performed to generate an image corresponding to the sensor specifications. This approach has been incorporated into an imaging code, SIG (SHARC Image Generator), by Brown and Grossbard (AFRL/VSBM) and has been used to generate synthetic images for both MSTI-3 and MSX.

6.3 Limb and Nadir Radiance

There have been several studies of the $\text{CO}_2(\nu_3)$ limb radiance for both day and night conditions. The radiance mechanisms are fairly well understood and accepted in the community. Furthermore, there have been several model validation studies for day/night conditions using Air Force Research Laboratory observations. These mechanisms have been incorporated into the SHARC code⁷ since its inception. For completeness, mean radiance profiles for both limb and nadir viewing geometries are presented here for both the subarctic and equatorial atmospheres. The limb radiance profile for $\text{CO}_2(\nu_3)$ indicating day/night and latitude variations is shown in Figure 28. There are strong diurnal effects with the day mean radiance being two orders of magnitude larger than the night radiance, above about 60 km. Below 50 km, conditions approach LTE and there is little day/night difference. These results are in excellent agreement with previous calculations. The relative importance of different vibrational transitions and isotopes have been discussed previously for daytime and nighttime conditions. Solar pumping of the CO_2 hot bands is the major mechanism contributing to the limb radiance between 50 and 90 km, where the fundamental is self-absorbed. Emission from the fundamental transition is the major mechanism at other altitudes. The nighttime radiance is also complicated, with virtually all hot bands and the minor isotopes making an important contribution to the limb radiance below 100 km. Above 110 km, the fundamental transition is again dominate. These results indicate that a proper description of the 4.3 μm radiance must include a detailed description of the chemical kinetics as well as an accurate treatment of the radiation transport.

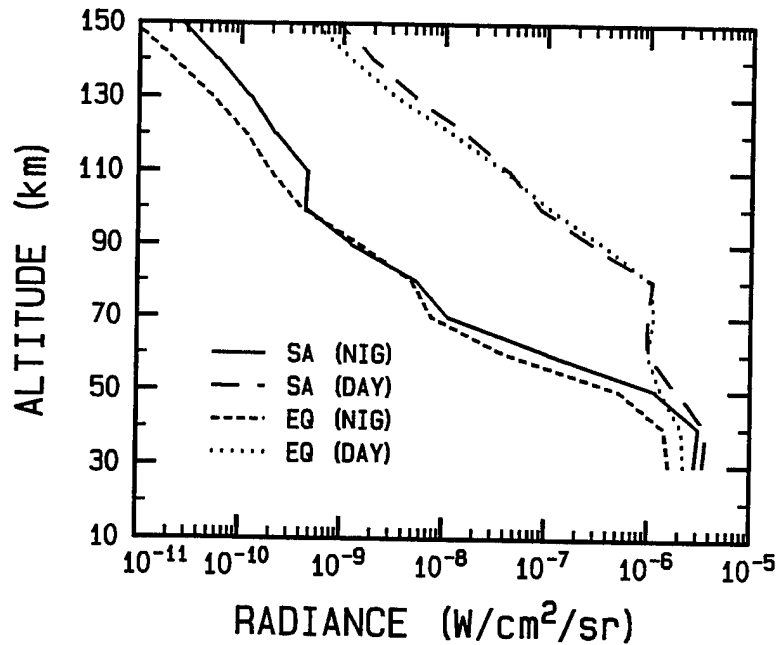


Figure 28. Diurnal Variation of the Altitude Dependence of MWIR Radiance for Subarctic and Equatorial Latitudes.

The limb radiance profiles for the $2.7 \mu\text{m}$ are shown in Figure 29. In this spectral region, the OH emission in the 80 to 90 km altitude region must be included in addition to the emission from H_2O . Again for this spectral region, the daytime profile is larger than nighttime for all altitudes, except in the vicinity of the OH airglow layer. In contrast to the $4.3 \mu\text{m}$ spectral region, the H_2O limb profile does not exhibit LTE behavior below 50 km which will have interesting consequences for low altitude structure calculations in this band.

A similar set of calculations were carried out for BTH viewing as a function of the off-nadir viewing angle. Figures 30 and 31 present the results for the MWIR AND SWIR spectral regions, respectively. For the MWIR, there is only a minor diurnal variability with a more significant latitude dependence. This result is consistent with the limb results, which indicate LTE conditions below 30 km where most of the emission originates in the BTH scenario. Also, since the region below 30 km is LTE and the most important radiating region, any difference in the temperature profiles in this region will have a significant effect on the observed radiance. The radiance in the SWIR shows the direct opposite behavior to the MWIR. In this band, there is little dependence on temperature, and therefore significant (\sim factor of three) diurnal variability. Again, these results are consistent with the NLTE effects observed in the limb calculations.

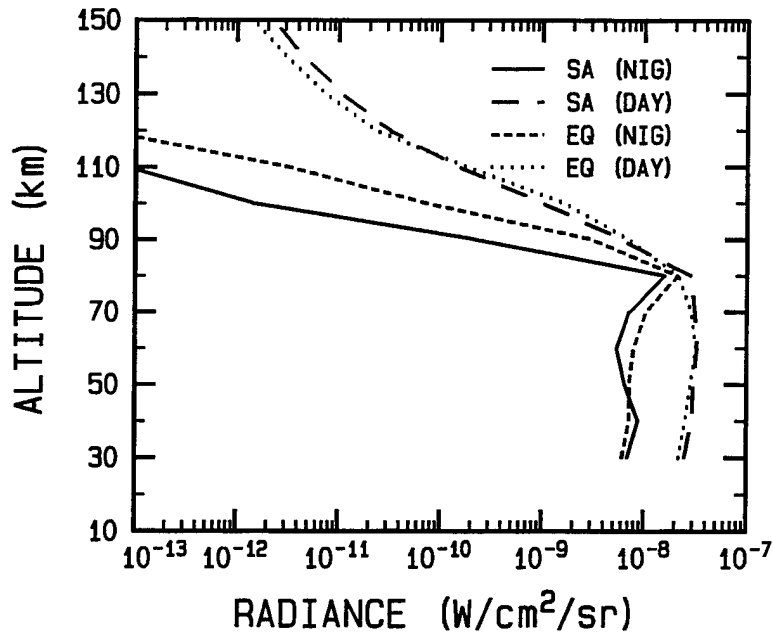


Figure 29. Diurnal Variation of the Altitude Dependence of the SWIR Radiance for Subarctic and Equatorial Latitudes.

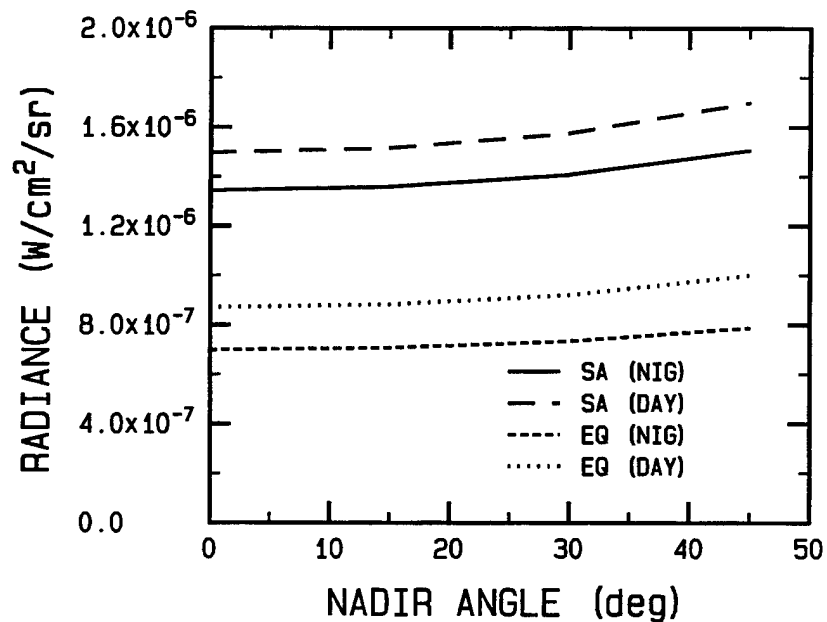


Figure 30. Diurnal Variation of the Viewing Angle Dependence of the CO₂ MWIR μm Band Radiance for Subarctic and Equatorial Latitudes.

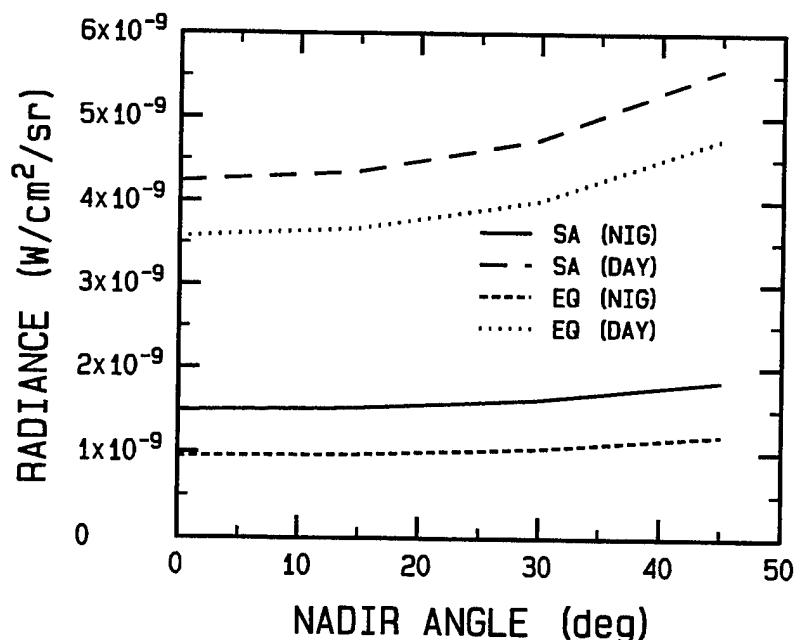


Figure 31. Diurnal Variation of the Viewing Angle Dependence of the SWIR Radiance for Subarctic and Equatorial Latitudes.

Finally, it was mentioned earlier that SHARC has been validated against other radiance models and AFRL data (e.g., SPIRE and CIRRIS-1A), which has been discussed earlier in this report. In general, the agreement between data and SHARC is quite good. Although extensive comparisons have been done for the limb geometry, to our knowledge no comparisons have been performed for nadir viewing geometry. However, recent work at Lincoln Laboratory [Burke et al., Private Communication, 1996] has established a data base for nadir viewing in the $\text{CO}_2(\nu_3)$ band for several seasons using data from HIRS/2. The data base contains not only seasonal variation, but latitude variation as well. Figure 32 shows data for both nadir and 45° off-nadir from one HIRS/2 orbit taken during May 1995. SHARC calculations were carried out for several latitudes. Again, the model atmospheres were generated using SAG. SHARC quantitatively predicts the orbital (or diurnal) variation of the radiance. Similar agreement is observed for the data sets examined from summer, fall, and winter. Although in general the agreement between the SHARC model and the HIRS/2 data is excellent, the effect of HIRS off-nadir viewing for daylight conditions (approximately 20 % increase in the radiance) is consistently underpredicted by SHARC by as much as 25 %. This appears to result from a mesopause temperature which is too hot, therefore more efficiently absorbing radiation from the stratosphere.

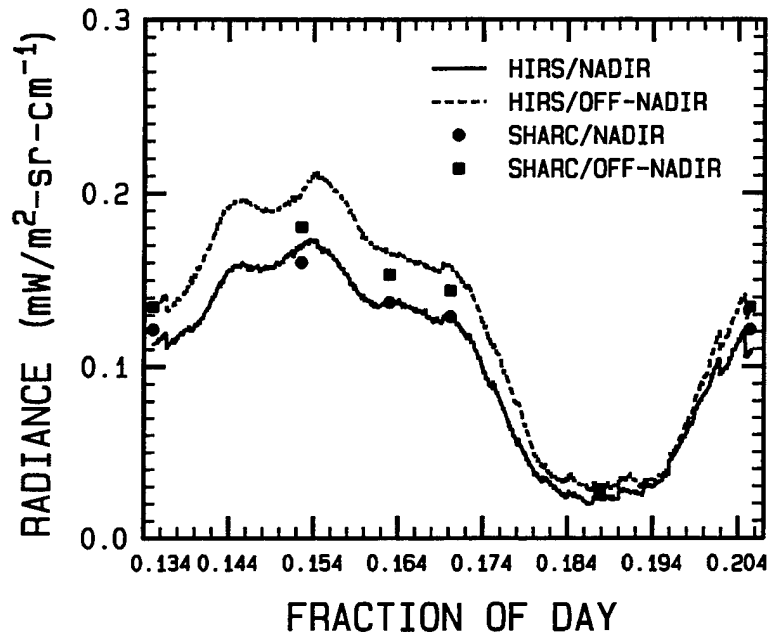


Figure 32. Comparison of the HIRS/2 Latitude Dependent Data with SHARC Calculations for NADIR Viewing.

6.4 Radiance Structure Statistics

The model described in this report has been applied to calculate the radiance structure for selected bands in the $4.3 \mu\text{m}$ $\text{CO}_2(\nu_3)$ spectral region and in the $2.7 \mu\text{m}$ (H_2O and OH) spectral region for two representative latitudes (i.e., temperature profiles) under day and night conditions. In addition, the sensitivity of the radiance statistics to variations in the temperature fluctuation model parameters has been investigated for these conditions. As discussed previously, the magnitude of the variance distribution function determines the extent to which a particular portion of the atmosphere contributes to the radiance structure at the sensor. For example, consider a LOS along which there is a maximum (or maxima) in the radiance distribution function at an altitude greater than the tangent point altitude. The effect of these maxima is that the local atmospheric structure at the maxima altitudes strongly affect the structure along the LOS with lower tangent point altitudes. The important point is that contributions to the LOS radiance structure must be considered along the complete LOS path, and not necessarily a single region along the LOS (such as the tangent point). In the following sections, the radiance statistical parameters are presented for both ATH and BTH viewing scenarios.

6.4.1 Effects of Latitudinal and Diurnal Variations

6.4.1.1 Above the Horizon (ATH) Limb Viewing

The radiance statistics at the sensor can be compared to the temperature statistics at the tangent point altitude by projecting the radiance values to the tangent point range. This corresponds to converting a distance in the image plane to the corresponding distance at the tangent point. The resulting radiance correlation lengths at the tangent point are shown in Figures 33 and 34 for the 4.3

μm band and Figures 36 and 37 for the $2.7 \mu\text{m}$ band. In general, for the $4.3 \mu\text{m}$ band, the radiance correlation lengths track the temperature correlation lengths (see Figures 22 and 23) for all examples except the nighttime subarctic atmosphere. In this case, the radiance correlation lengths between 50 km and 120 km are determined by the higher altitudes (see Figure 26). This behavior results from dominance of the variance distribution function in the high altitude region of the LOS path over the lower altitude portions of the LOS path, as shown in Figure 26 for the nighttime subarctic atmosphere. For the $2.7 \mu\text{m}$ band in all cases, the radiance correlation lengths track the temperature correlation lengths (again, see Figures 22 and 23) at all altitudes greater than 50 km. Below 50 km, the correlation lengths are determined by the variance distribution function in the 50 to 90 km range, showing approximately a 30% variability with atmospheric temperature and little diurnal variation. The relative standard deviation, the absolute standard deviation divided by the absolute mean radiance, as a function of altitude is illustrated in Figures 35 and 38 for the $4.3 \mu\text{m}$ band and the $2.7 \mu\text{m}$ band, respectively. The nighttime relative standard deviations are greater than the corresponding daytime values for both bands and atmospheres above 50 km (a factor of two for the $4.3 \mu\text{m}$ band and a factor of three for the $2.7 \mu\text{m}$ band. Below 50 km, the relative standard deviation for the $4.3 \mu\text{m}$ band is independent of any variation due to the dominance of LTE conditions, while the $2.7 \mu\text{m}$ band results show significant NLTE effects with the nighttime conditions again having a larger relative standard deviation.

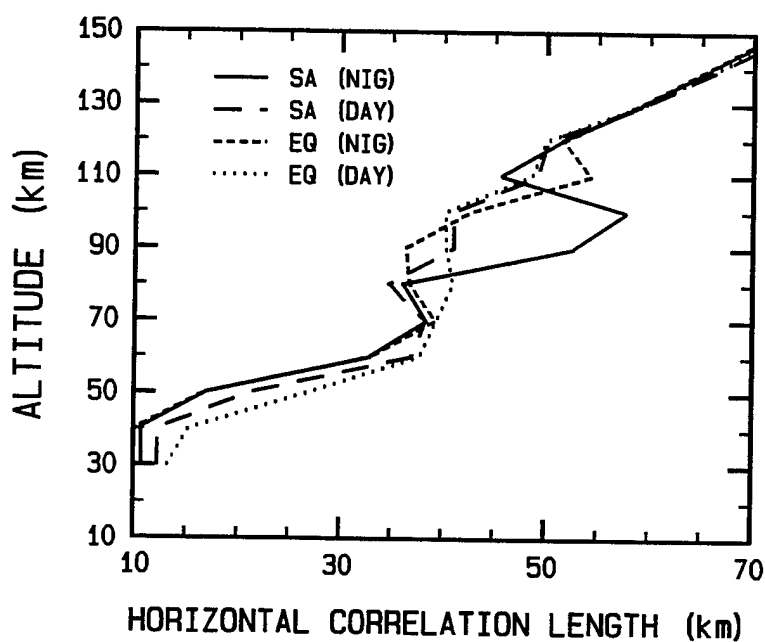


Figure 33. Diurnal Variation of the Altitude Dependence of the Horizontal Correlation Length for Subarctic and Equatorial Latitudes in the MWIR Spectral Region.

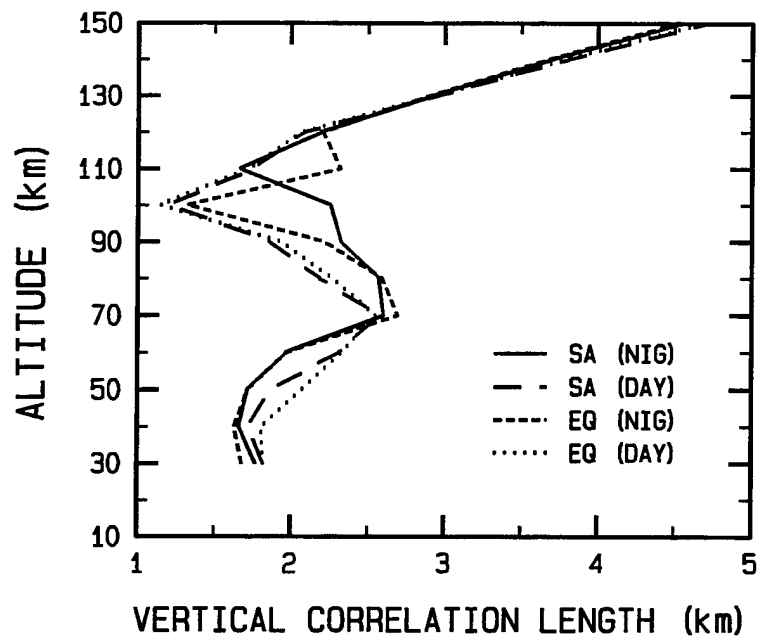


Figure 34. Diurnal Variation of the Altitude Dependence of the Vertical Correlation Length for Subarctic and Equatorial Latitudes in the MWIR Spectral Region.

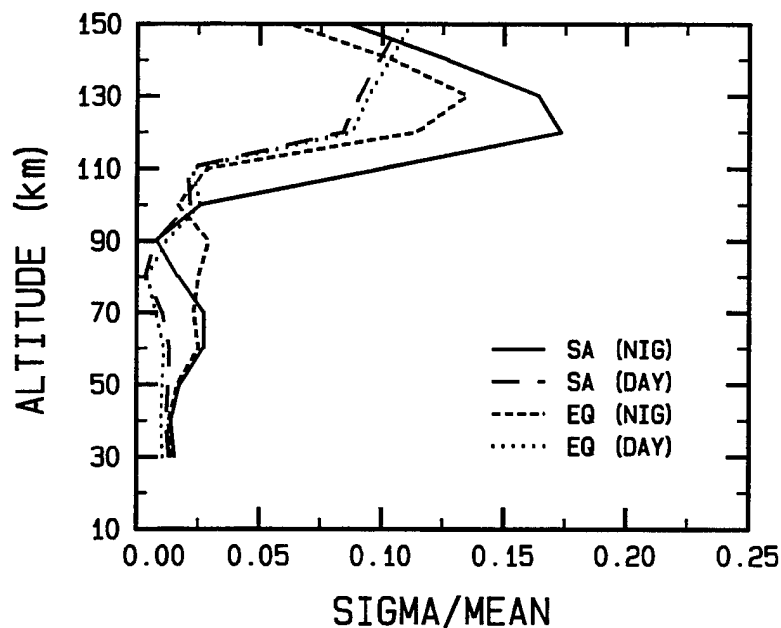


Figure 35. Diurnal Variation of the Altitude Dependence of the Relative Standard Deviation for Subarctic and Equatorial Latitudes in the MWIR Spectral Region.

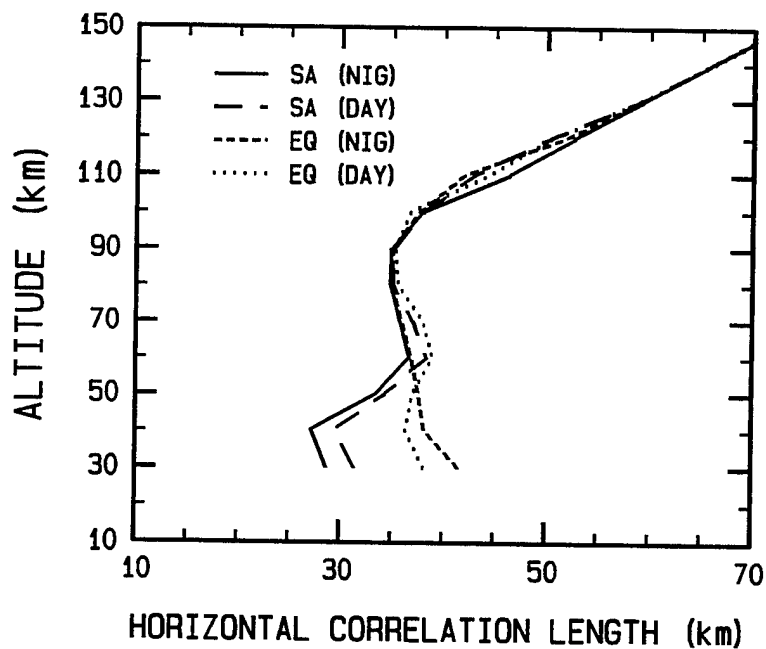


Figure 36. Diurnal Variation of the Altitude Dependence of the Horizontal Correlation Length for Subarctic and Equatorial Latitudes in the SWIR Spectral Region.

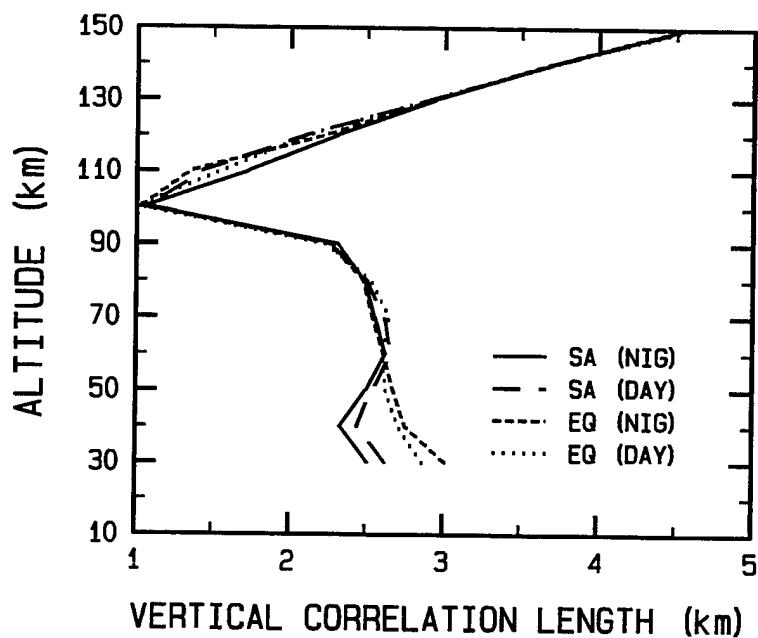


Figure 37. Diurnal Variation of the Altitude Dependence of the Vertical Correlation Length for Subarctic and Equatorial Latitudes in the SWIR Spectral Region.

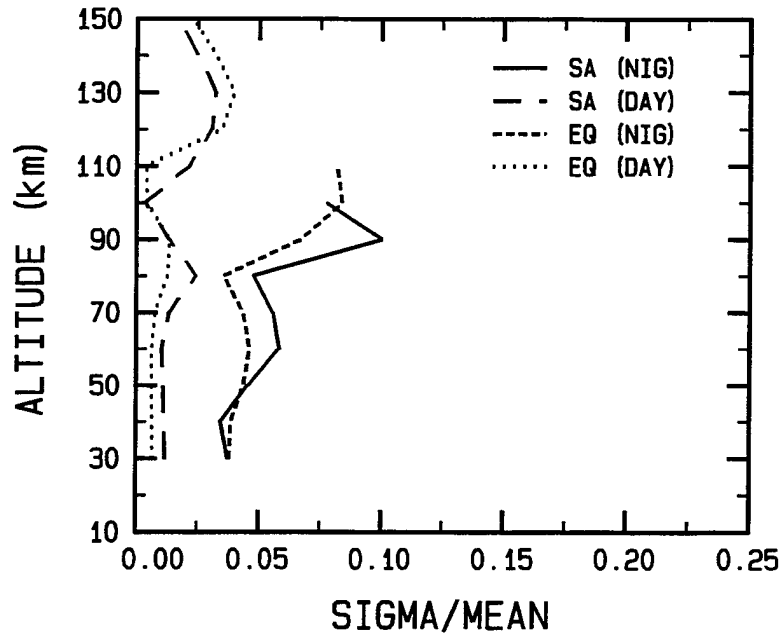


Figure 38. Diurnal Variation of the Altitude Dependence of the Relative Standard Deviation for Subarctic and Equatorial Latitudes in the SWIR Spectral Region.

6.4.1.2 Below the Horizon (BTH) Nadir Viewing

A similar set of calculations were performed for the BTH scenario as a function of viewing angle from nadir (looking straight down) to 45° off-nadir. Here, the altitude profile of the variance distribution function determines the extent to which a particular region of the atmosphere contributes to the radiance structure at the sensor. The resulting radiance correlation lengths as a function of viewing angle are shown in Figures 39 and 40 for the 4.3 μm band and Figures 42 and 43 for the 2.7 μm band. For nadir viewing in the 4.3 μm band, the radiance correlation lengths are determined by altitudes less than 30 km with a small diurnal variation for the subarctic atmosphere and a 30% diurnal variation for the equatorial atmosphere. In the 2.7 μm band, there is no sensitivity to temperature at night, but a rather large variation (~50%) to temperature during the day. For both bands, as the off-nadir angle is increased, there is little relative change in the horizontal correlation lengths, and the variability of the vertical correlation lengths becomes less important. The relative standard deviation as a function of viewing angle is illustrated in Figures 41 and 44 for the 4.3 μm band and the 2.7 μm band, respectively. There is only a minor viewing angle dependence of the relative standard deviations for both bands. For the 4.3 μm band, there is virtually no dependence on the temperature variability, and only a 20% diurnal variation. Of more interest is the 2.7 μm band which shows some temperature variability but a factor of 3 diurnal variation.

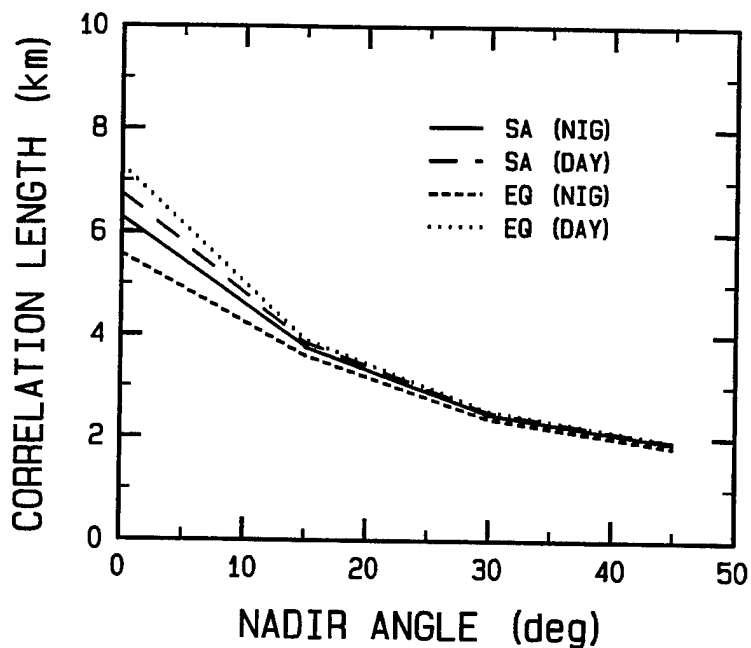


Figure 39. Diurnal Variation of the Viewing Angle Dependence of the Vertical Correlation Length for Subarctic and Equatorial Latitudes in the MWIR Spectral Region.

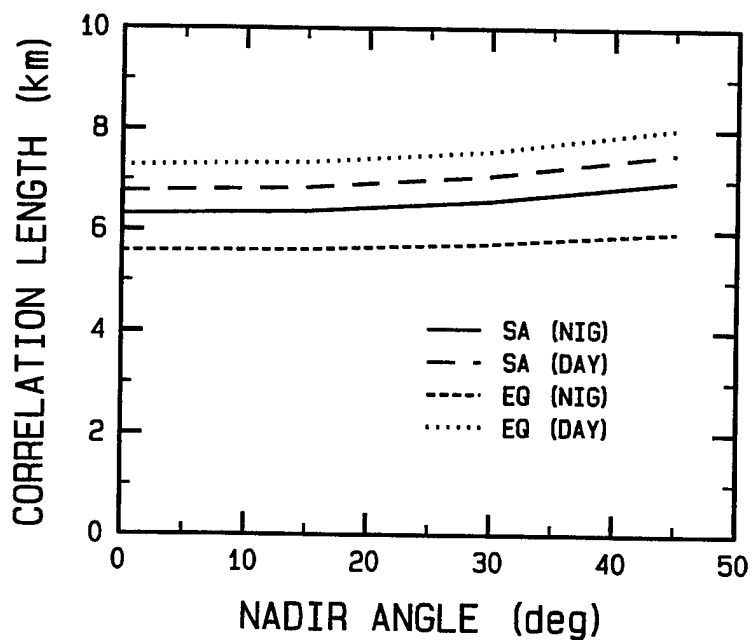


Figure 40. Diurnal Variation of the Viewing Angle Dependence of the Horizontal Correlation Length for Subarctic and Equatorial Latitudes in the MWIR Spectral Region.

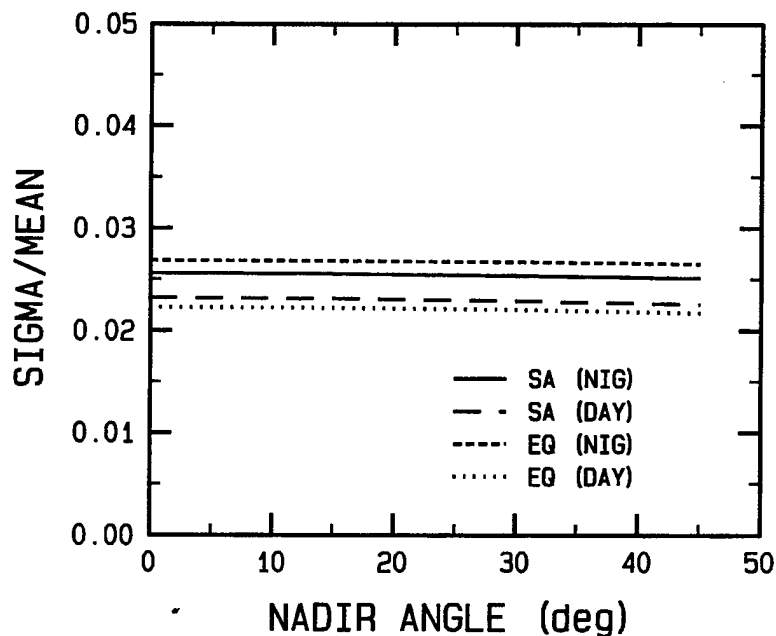


Figure 41. Diurnal Variation of the Viewing Angle Dependence of the Relative Standard Deviation for Subarctic and Equatorial Latitudes in the MWIR Spectral Region.

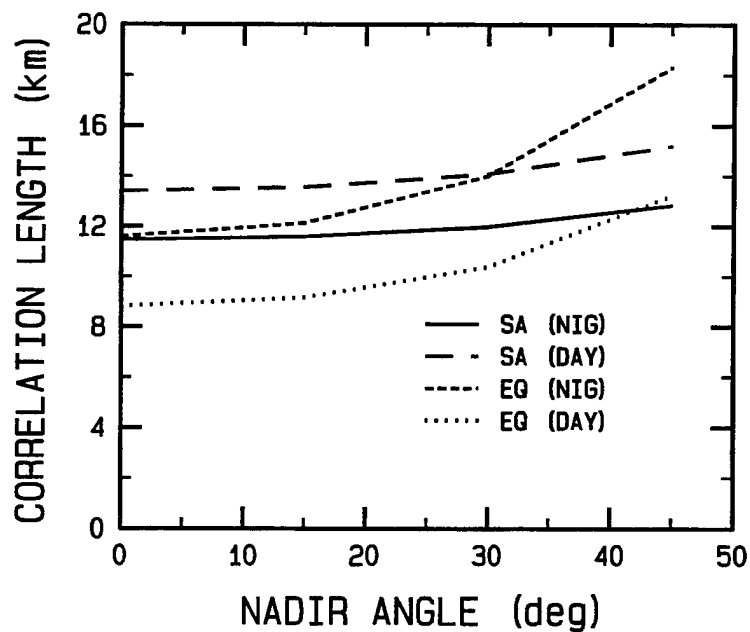


Figure 42. Diurnal Variation of the Viewing Angle Dependence of the Horizontal Correlation Length for Subarctic and Equatorial Latitudes in the SWIR Spectral Region.

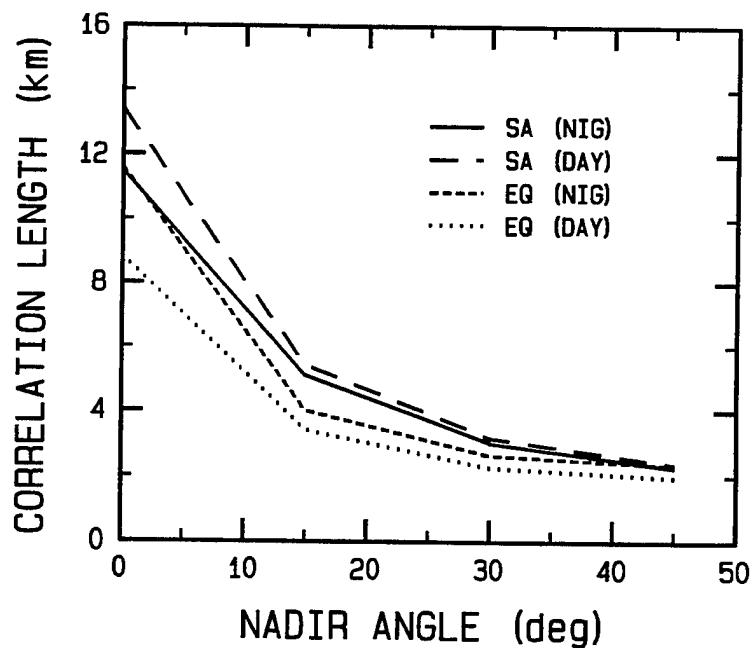


Figure 43. Diurnal Variation of the Viewing Angle Dependence of the Vertical Correlation Length for Subarctic and Equatorial Latitudes in the SWIR Spectral Region.

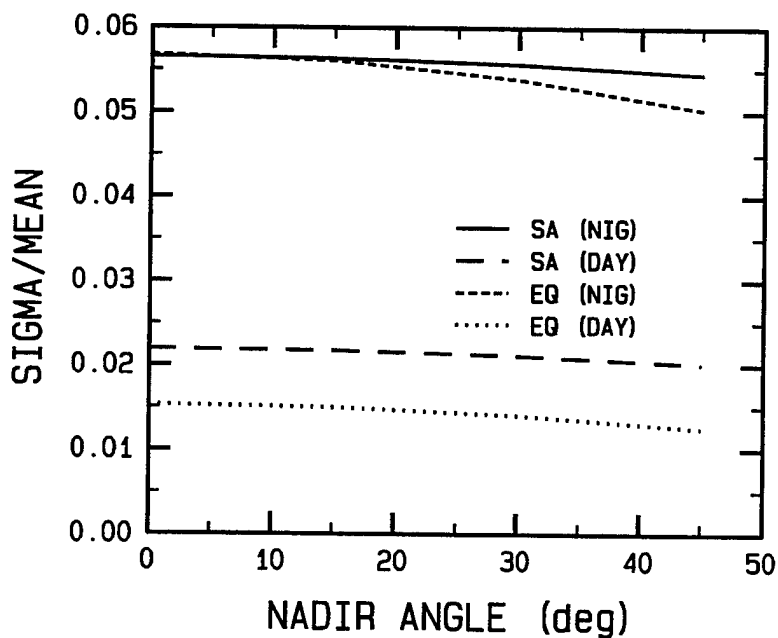


Figure 44. Diurnal Variation of the Viewing Angle Dependence of the Relative Standard Deviation for Subarctic and Equatorial Latitudes in the SWIR Spectral Region.

6.4.2 Variation of Temperature Statistical Parameters for ATH Limb Viewing

The NSS temperature fluctuation model is described by the temperature correlation lengths, the temperature variance, and the slope of the temperature PSD function. The baseline values for the correlation lengths and variance as a function of altitude are shown in Figures 22 - 24. The slope of the temperature PSD is assumed to be altitude independent with a value of -2 for both vertical and horizontal directions. The effect of using values of the PSD slope derived from gravity wave theory on the radiance statistics is discussed later in this section.

The simplest NSS parameter variation investigated in the sensitivity study is the temperature standard deviation, σ_T . From Eqs. (36) and (38), one would expect that a variation in the temperature standard deviation (or variance) would result in an equal variation in the radiance standard deviation (σ_L) which is exactly what is observed. The same behavior is observed in the SWIR bandpass. Thus, one can conclude that not only are σ_T variations directly reflected in the radiance standard deviation, but the relative σ_L variability is independent of bandpass. Of course, if the magnitude of variations are altitude dependent, then the variations in the relative radiance standard deviation would be dependent on bandpass.

The other quantities varied in the sensitivity study are the horizontal and vertical temperature correlation lengths, L_{ch}^T and L_{cv}^T . The effect of variations in L_{ch}^T and L_{cv}^T on the radiance horizontal and vertical correlation lengths L_{ch}^L and L_{cv}^L is quite simple, again based on Eq. (38) for the weighting function. The radiance correlation lengths are computed by multiplying the weighting functions by the temperature correlation lengths and integrating that quantity along the LOS. Therefore, since the weighting function depends directly on the correlation length along the LOS, any variation in the vertical or horizontal temperature correlation length is directly reflected in the corresponding radiance quantity. Therefore, a factor of 2 increase or decrease in L_{ch}^T and/or L_{cv}^T would result in a factor of 2 increase or decrease in L_{ch}^L and/or L_{cv}^L . Although dependence of the σ_L on variations in L_{ch}^T and L_{cv}^T is in general not quite as simple, maximum and minimum variations of σ_L can be established quite easily. Consider the case where both L_{ch}^T and L_{cv}^T are increased or decreased by a factor A, then from Eqs. (36) and (38), σ_L is increased or decreased by \sqrt{A} . For other combinations, the variation of L_{ch}^T has the dominate effect on σ_L , while variations in L_{cv}^T are much less important. The dominance of variations of L_{ch}^T on σ_L results from the horizontal correlation length making the major contribution to the correlation length along the LOS, $l_r \bar{r}$ in Eq. (38), for limb views. The influence of variations of L_{ch}^T and L_{cv}^T on the relative σ_L is independent of atmospheric temperature (i.e., latitude), diurnal conditions, and spectral bandpass.

The final variation studied considers variation of the temperature PSD slope in the NSS model from -2 for all directions to a -3 in the vertical directions and -5/3 in the horizontal direction, values consistent with gravity wave theory. The effects on the radiance correlation lengths is rather insignificant with the largest variability of less than 20 % shown for the horizontal correlation lengths. The PSD spectral slope has no effect on the radiance relative standard deviation.

7. SUMMARY

The research program conducted under the present contract has provided new first-principles approaches for the development of NLTE kinetic and radiance models for the solar terminator and atmospheric stochastic structure. These models have been incorporated into new versions of the Air Force non-LTE upper atmospheric IR radiance code, SHARC. In addition, related efforts have developed a capability to generate model atmospheres given the geographic location and parameters characterizing the solar and geomagnetic activity. Finally, a new computer model, based on the merging of SHARC and MODTRAN (SAMM), has been developed and extensively validated by comparisons with existing atmospheric models and field data. The remainder of this section summarizes in more detail the development of these models.

The SHARC Atmosphere Generator, which utilizes a combination of empirical models to generate atmospheric profiles that properly account for solar terminator and other systematic variability effects, was developed for IR radiance calculations appropriate for particular experimental scenarios. The goal in developing SAG has been to provide reasonably accurate temperature and species profiles with an easy-to-use, rapid-executing program. Comparisons of available field data with radiance predictions has provided valuable tests of the radiation codes, the atmospheric profile models and, in a larger sense, our overall understanding of atmospheric processes.

A model for ozone vibrational bands has been incorporated into SHARC, resulting in improved predictions for radiation in the ν_1 and ν_3 regions (8-12 μm) near the mesopause. An "effective" kinetic scheme was adopted for the high-lying $\text{O}_3(\nu)$ states to reduce complexity and computation time, while maintaining a sufficient number of vibrational states for an accurate representation of the ν_3 hot band spectrum. The lower vibrational states are handled using a complete state-to-state kinetic model. The model parameters are consistent with the recent literature, and the predicted spectral radiances are in good accord with the SPIRIT-1 and CIRRIS-1A data. Improved values of the ozone band centers and quenching rate constants at the highest vibrational energies and the incorporation of even more bands might result in further improvements in accuracy.

The atmospheric IR radiance terminator model has been used to simulate limb radiances for CO_2 , O_3 , and OH in the solar terminator region that correspond to observations from the 1977 SPIRE and 1991 CIRRIS-1A experiments. These calculations represent the first direct comparisons with field data using the new multiple-profiles and multiple-atmospheres features in SHARC. The good agreement between the calculations and the data provide substantial validation of the kinetic and radiation transport models in SHARC as well as the O_3 and H atom profiles from the SHARC Atmosphere Generator.

SAMM, a new moderate spectral resolution (2 cm^{-1}) infrared (IR) atmospheric transmission and background radiance model applicable at altitudes from ground to space (300 km), was developed by integrating the Air Force standard lower atmosphere (2 cm^{-1} MODTRAN) and upper atmosphere (1 cm^{-1} SHARC) moderate spectral resolution models into a single, seamless code with a unified and correlated radiative transport algorithm. A new radiative transport algorithm was developed which is applicable to both the low and high altitude regimes. SAMM contains the majority of features of both MODTRAN and SHARC, providing the scientific and DOD community with the capability to treat both low altitude ($<30\text{ km}$) and high altitude phenomena in a self-consistent manner. The model has been extensively validated in the 2-40 μm spectral region by comparisons with both MODTRAN and SHARC, as well as the CIRRIS-1A data base.

The NLTE infrared radiance fluctuations in the atmosphere depend on the fluctuations in the density of atmospheric species, individual molecular state populations, and kinetic temperatures and pressures along the sensor line-of-sight. An algorithm to predict the non-equilibrium dependence of molecular state number density fluctuations on kinetic temperature and density fluctuations has been developed to predict the line-of-sight mean radiance, radiance derivatives, and the resultant radiance statistics. Calculations were performed to investigate the effects of diurnal, climatological, and temperature statistics variability on the LOS radiance statistics.

8. ACKNOWLEDGEMENTS

The authors gratefully acknowledge many useful discussions and comments from Dr. Ramesh Sharma and Mr. James Brown, AFRL/VSBM, concerning many technical aspects of this work. Thanks are also due to W. Cornette (Photon Research Associates) for numerous improvements to the SAG code, R. Rodrigo (Instituto de Astrofisica de Andalucia) for providing theoretical species profiles, R. Healey and J. Vail (Mei Technology Corp.) for code testing, and D. Smith, G. P. Anderson, and J. Chetwynd (AFRL) for valuable discussions and providing various data bases used in this work. Finally, we are indebted to Drs. William Blumberg and Liali Jeong (AFRL) for their continuing support and interest during this contract.

9. REFERENCES

1. F. X. Kneizys, E. P. Shettle, W. O. Gallery, J. H. Chetwynd, Jr., L. W. Abreu, J. E. A. Selby, S. A. Clough, and R. W. Fenn, "Atmospheric Transmittance/Radiance: Computer Code LOWTRAN 6," AFGL-TR-83-0187, Air Force Geophysics Laboratory, Hanscom AFB, MA (1983). ADA137796.
2. A. Berk, L. S. Bernstein, and D. C. Robertson, "MODTRAN: A Moderate Resolution Model for LOWTRAN 7," Rpt. No. GL-TR-89-0122, Geophysics Laboratory, Hanscom AFB, MA (1989). ADA214337.
3. S. A. Clough, F. X. Kneizys, E. P. Shettle, and G. P. Anderson, "Atmospheric Radiance and Transmittance: FASCOD2". Proceedings of the Sixth Conference on Atmospheric Radiation, pp. 141-144, American Meteorological Society, Boston, MA (1986).
4. R. D. Sharma, A. J. Ratkowski, R. L. Sundberg, J. W. Duff, L. S. Bernstein, P. K. Acharya, J. H. Gruninger, D. C. Robertson, and R. J. Healey, "Description of SHARC, The Strategic High-Altitude Radiance Code," GL-TR-89-0229 (1989). ADA206236.
5. R. D. Sharma, J. W. Duff, R. L. Sundberg, L. S. Bernstein, J. H. Gruninger, D. C. Robertson, and R. J. Healey, "Description of SHARC-2, The Strategic High-Altitude Radiance Code," PL-TR-91-2071 (1991). ADA239008.
6. R. D. Sharma, J. H. Gruninger, R. L. Sundberg, L. S. Bernstein, D. C. Robertson, J. H. Brown, S. M. Adler-Golden, J. W. Duff, M. W. Matthew, and R. J. Healey, "User's Manual for SHARC-3, Strategic High-Altitude Radiance Code," PL-TR-96-2104 (1996). ADA313523
7. R. L. Sundberg, J. W. Duff, J. H. Gruninger, L. S. Bernstein, M. W. Matthew, S. M. Adler-Golden, D. C. Robertson, R. D. Sharma, J. H. Brown, and R. J. Healey, "SHARC, a Model

- for Calculating Atmospheric Infrared Radiation under Non-Equilibrium Conditions," in *The Upper Mesosphere and the Lower Thermosphere: A review of Experiment and Theory, Geophysical Monograph Series*, **87**, 287 (1995).
8. P. P. Wintersteiner, R. H. Picard, R. D. Sharma, J. R. Winick, and R. A. Joseph, "Line-by-Line Radiative Excitation Model for the Non-Equilibrium Atmosphere: Application to CO₂ 15- μ m Emission," *J. Geophys. Res.*, **97**, 18083 (1992).
 9. M. Lopez-Puertas, R. Rodrigo, A. Molina, and F. W. Taylor, "A Non-LTE Radiative Transfer Model for Infrared Bands in the Middle Atmosphere, I, Theoretical Basis and Application to CO₂ 15 μ m Bands," *J. Atmos. Terr. Phys.*, **48**, 729 (1986).
 10. M. Lopez-Puertas, R. Rodrigo, J. J. Lopez-Moreno, and F. W. Taylor, "A Non-LTE Radiative Transfer Model for Infrared Bands in the Middle Atmosphere, II, CO₂ (2.7 and 4.3 μ m) and Water Vapor (6.3 μ m) Bands and N₂(1) and O₂(1) Vibrational Levels," *J. Atmos. Terr. Phys.*, **48**, 749 (1986).
 11. D. C. Robertson, P. K. Acharya, S. M. Adler-Golden, L. S. Bernstein, F. Bien, J. W. Duff, J. H. Gruninger, R. L. Sundberg, R. J. Healey, J. M. Sindoni, P. M. Bakshi, A. Dalgarno, and B. Zygelman, "Investigations into Atmospheric Radiative Processes in the 50-300 km Regime," PL-TR-91-2137 (1991). ADA251588.
 12. R. J. Kee, J. A. Miller, and T. H. Jefferson, "CHEMKIN: Problem-Independent, Transportable, Fortran Chemical Kinetics Code Package," Sandia Rpt. No. SAND80-8003, Sandia National Laboratory, Livermore, CA 94550 (1980).
 13. J. B. Kumer and T. C. James, "CO₂ (001) and N₂ Vibrational Temperatures in the 50 \leq Z \leq 130 km Altitude Range," *J. Geophys. Res.*, **79**, 638 (1974).
 14. J. B. Kumer, "Atmospheric CO₂ and N₂ Vibrational Temperatures at 40- to 140-km Altitude," *J. Geophys. Res.*, **82**, 16 (1977).
 15. J. B. Kumer, A. T. Stair, Jr., N. Wheeler, K. D. Baker, and D. J. Baker, "Evidence for an OH \dagger -N₂ \dagger -CO₂(v₃)-CO₂+hv(4.3 μ m) Mechanism for 4.3- μ m Airglow," *J. Geophys. Res.*, **83**, 4743 (1978).
 16. R. L. Taylor, "Energy Transfer Processes in the Stratosphere," *Can. J. Chem.*, **52**, 1436 (1974).
 17. L. S. Rothman, R. R. Gamache, A. Goldman, L. R. Brown, R. A. Toth, H. M. Pickett, R. L. Pynter, J. -M. Flaud, C. Camy-Peyret, A. Barbe, N. Husson, C. P. Rinsland and M. A. H. Smith, "The HITRAN Molecular Database. Editions of 1991 and 1992," *J. Quant. Spectrosc. Radiat. Transfer*, **48**, 469 (1992).
 18. A. T. Stair, Jr., R. D. Sharma, R. M. Nadile, D. J. Baker, and W. F. Grieder, "Observations of Limb Radiance with Cryogenic Spectral Infrared Rocket Experiment," *J. Geophys. Res.*, **90**, 9763 (1985).
 19. A. E. Hedin, "Extension of the MSIS Thermosphere Model Into the Middle and Lower Atmosphere," *J. Geophys. Res.*, **96**, 1159 (1991).
 20. C. P. Rinsland, M. R. Gunson, R. Zander, and M. Lopez-Puertas, "Middle and Upper Atmosphere Pressure-Temperature Profiles and the Abundances of CO₂ and CO in the Upper Atmosphere From ATMOS/Spacelab 3 Observations," *J. Geophys. Res.*, **97**, 20479 (1992).

21. P. P. Wintersteiner, R. A. Joseph, and A. J. Paboojian, "High-Altitude Non-Equilibrium Infrared Emission Models," ARCON Corporation, GL-TR-90-0311 (1990). ADA232503.
22. H. Nebel, P. P. Wintersteiner, R. H. Picard, J. R. Winick, and R. D. Sharma, "CO₂ non-local Thermodynamic Equilibrium Radiative Excitation and Infrared Dayglow at 4.3 μ m: Application to Spectral Infrared Rocket Experiment Data," *J. Geophys. Res.*, **99**, 10409 (1994).
23. M. Lopez-Pertas, M. A. Lopez-Valverde, C. P. Rinsland, and M. R. Gunson, "Analysis of the Upper Atmosphere CO₂(v₂) Vibrational Temperatures Retrieved From ATMOS/Spacelab 3 Observations," *J. Geophys. Res.*, **97**, 20469 (1992).
24. A. E. Grün, "Lumineszenz-photometrische Messungen der Energie-absorption im Strahlungsfeld von Elektronenquellen Eindimensionaler Fall im Luft," *Z. Naturforsch.*, **112a**, 89-95 (1957).
25. M. H. Rees, "Auroral Ionization and Excitation by Incident Energetic Electrons," *Planet. Space Sci.*, **111**, 1209-18 (1964).
26. D. J. Strickland, J. R. Jasperse, and J. A. Whalen, "Dependence of Auroral FUV Emissions on the Incident Electron Spectrum and Neutral Atmosphere," *J. Geophys. Res.*, **88**, 8051-62 (1983).
27. J. P. Winick, R. H. Picard, R. A. Joseph, R. D. Sharma, and P. P. Wintersteiner, "AARC: The Auroral Atmospheric Radiance Code," AFGL-TR-87-0334 (1987). ADA202432.
28. O. Ashihara and K. Takayanagi, "Velocity Distribution of Ionospheric Low-Energy Electrons," *Planet. Space Sci.*, **22**, 1201 (1974).
29. J. B. Kumer, "Theory of the CO₂ 4.3 μ m Aurora and Related Phenomena," *J. Geophys. Res.*, **82**, 2203 (1977).
30. A. R. Curtis, "A Statistical Model for Water Vapour Absorption," *Q. J. R. Meteorol. Soc.*, **78**, 638-640 (1952)
31. W. L. Godson, "The Evaluation of Infrared-Radiative Fluxes due to Atmospheric Water Vapour," *Q. J. R. Meteorol. Soc.*, **79**, 367 (1953).
32. C. B. Ludwig, W. Malkmus, J. E. Reardon, and J. A. Thomson, *Handbook of Infrared Radiation From Combustion Gases*, NASA SP-3080, Scientific and Technical Information Office, NASA, Washington, DC (1973).
33. C. D. Rodgers and A. P. Williams, "Integrated Absorption of a Spectral Line with the Voigt Profile," *J. Quant. Spectrosc. Radiat. Transfer*, **14**, 319 (1974).
34. "U. S. Standard Atmosphere 1976," National Oceanic and Atmospheric Administration, NOAA-S/T 76-1562, U.S. Govt. Printing Office, Washington DC (1976).
35. R. E. Murphy, "EXCEDE III Catalog of Corrected Spectra and Corrected Interferograms," Rpt. Nos. 12-15, Research Sciences Corp., Lexington, MA (1992-3).
36. P. J. Espy, C. R. Harris, A. J. Steed, J. C. Ulwick, R. H. Haycock, and R. A. Straka, "Rocketborne Interferometer Measurement of Infrared Auroral Spectra," *Planet. Space Sci.*, **36**, 543 (1988).
37. A. E. Hedin, "Extension of the MSIS Thermospheric Model into the Middle and Lower Atmosphere," *J. Geophys. Res.*, **96**, 1159 (1991).

38. M. E. Summers, W. J. Sawchuck, and G. P. Anderson, "Model Climatologies of Trace Species in the Atmosphere," Annual Review Conference on Atmospheric Transmission Models, Phillips Laboratory, Hanscom AFB, MA, June, 1992.
39. G. P. Anderson, J. H. Chetwynd, S. A. Clough, E. P. Shettle and F. X. Kneizys, "AFGL Atmospheric Constituent Profiles (0-120 km)," AFGL-TR-86-0110 (1986). ADA175173.
40. R. Rodrigo, M. J. Lopez-Gonzalez, and J. J. Lopez-Moreno, "Variability of the Neutral Mesospheric and Lower Thermospheric Composition in the Diurnal Cycle," *Planet. Space Sci.*, **39**, 803 (1991).
41. H. Trinks and K. H. Fricke, Carbon Dioxide Concentrations in the Lower Thermosphere," *J. Geophys. Res.*, **83**, 3883 (1978).
42. D. Offermann, V. Friedrich, P. Ross, and U. von Zahn, "Neutral Gas Composition Measurements Between 80 and 120 km," *Planet. Space Sci.*, **29**, 747 (1981).
43. R. D. Sharma and P. P. Wintersteiner, "Role of Carbon Dioxide in Cooling Planetary Atmospheres," *Geophys. Res. Lett.*, **17**, 2201 (1990).
44. M. Lopez-Puertas and F. W. Taylor, "Carbon Dioxide 4-3- μ m Emission in the Earth's Atmosphere: A Comparison Between Numbus 7 SAMS Measurements and Non-Local Thermodynamic Between Equilibrium Radiative Transfer Calculations," *J. Geophys. Res.*, **94**, 13045 (1989).
45. C. P. Rinsland, M. R. Gunson, R. Zander, and M. Lopez-Puertas, "Middle and Upper Atmosphere Pressure-Temperature Profiles and the Abundances of CO₂ and CO in the Upper Atmosphere From ATMOS/Spacelab 3 Observations," *J. Geophys. Res.*, **97**, 20479 (1992).
46. D. R. Smith, P. De, S. Adler-Golden, and C. Roth, "Empirical Correlations in Thermospheric NO Density Measured From Rockets and Satellites," *J. Geophys. Res.*, **98**, 9453 (1993).
47. D. W. Rusch, J.-C. Gerard, and C. G. Fesen, "Diurnal Variation of NO, N(²D), and Ions in the Thermosphere: A Comparison of Satellite Measurements to a Model," *J. Geophys. Res.*, **96**, 11331 (1991).
48. C. A. Barth, "Reference Models for Thermospheric NO," *Adv. Space Res.*, **10**, 103 (1990).
49. J. I. Steinfeld, S. M. Adler-Golden, and J. W. Gallagher, "Critical Survey of Data on the Spectroscopy and Kinetics of Ozone in the Mesosphere and Thermosphere," *J. Phys. Chem. Ref. Data*, **16**, 911 (1987).
50. H. Hippler, R. Rahn, and J. Troe, "Temperature and Pressure Dependence of Ozone Formation Rates in the Range 1-1000 Bar and 90-370 K," *J. Chem. Phys.*, **93**, 6560 (1990).
51. R. J. Thomas, "Atomic Hydrogen and Atomic Oxygen Density in the Mesopause Region: Global and Seasonal Variations Deducted from Solar Mesosphere Explorer Near-Infrared Emissions," *J. Geophys. Res.*, **95**, 16457 (1990).
52. W. E. Sharp and D. Kita, "In situ Measurement of Atomic Hydrogen in the Upper Mesosphere," *J. Geophys. Res.*, **92**, 4319 (1987).

53. S. M. Adler-Golden, J. Gruninger, and D. R. Smith, "Derivation of Atmospheric Atomic Oxygen and Hydrogen Profiles From Ozone ν_3 Band Emission," *J. Geophys. Res.*, **97**, 19509 (1992).
54. D. D. Grantham, I. I. Gringorten, and A. J. Kantor, Chapter 16.1 in "Handbook of Geophysics and the Space Environment," A. S. Jursa, ed., Geophys. Lab., Hanscom AFB, MA (1985). ADA167000.
55. M. Ahmadjian, R. M. Nadile, J. O. Wise, and B. Bartschi, "CIRRIS-1A Space Shuttle Experiment," *J. Spacecr. Rockets*, **27**, 669 (1990).
56. R. M. Nadile, M. A. Ahmadjian, J. Jacavano, J. R. Griffin, D. A. Dean, S. D. Price, A. J. Steed, B. Y. Bartschi, J. G. Blakely, R. E. Hegblom, G. S. Bluford, and C. L. Veach, "Observations of Infrared Atmospheric Emissions with the Cryogenic Infrared Radiance Instrumentation for Shuttle (CIRRIS 1A) from STS-39," AGU Fall Meeting, San Francisco, CA (December 1991).
57. D. R. Smith, W. A. M. Blumberg, R. M. Nadile, S. J. Lipson, E. R. Huppi, N. Wheeler, and J. A. Dodd, "Observation of High-N Hydroxyl Pure Rotation Lines in Atmospheric Emission Spectra by the CIRRIS-1A Space Shuttle Experiment," *Geophys. Res. Lett.*, **19**, 593 (1992).
58. S. M. Adler-Golden, M. W. Matthew, D. R. Smith, and A. J. Ratkowski, "The 9- to 12- μ m Atmospheric Ozone Emission Observed in the SPIRIT 1 Experiment," *J. Geophys. Res.*, **95**, 15243 (1990).
59. T. C. Degges and H. J. P. Smith, "A High-Altitude Infrared Radiance Model," AFGL-TR-77-0271 (1977). ADA 059242
60. S. M. Adler-Golden and D. R. Smith, "Identification of 4- to 7-Quantum ν_3 Bands in the Atmospheric Recombination Spectrum of Ozone," *Planet. Space Sci.*, **38**, 1121 (1990).
61. M. G. Mlynczak and S. R. Drayson, "Calculation of Infrared Limb Emission by Ozone in the Terrestrial Middle Atmosphere 1. Source Functions," *J. Geophys. Res.*, **95**, 16497 (1990).
62. R. O. Manuilova and G. M. Shved, *J. Atmos. Terr. Phys.*, **54**, 1149 (1992).
63. S. M. Adler-Golden, "Analysis of SPIRIT LWIR Emission: An Ozone ν_3 Model," Report No. SSI-TR-122, Spectral Sciences Inc. (1987).
64. W. T. Rawlins, G. E. Caledonia, and R. A. Armstrong, "Dynamics of Vibrationally Excited Ozone Formed by Three-body Recombination, II, Kinetics and Mechanism," *J. Chem. Phys.*, **87**, 5209 (1987); W. T. Rawlins and R. A. Armstrong, "Dynamics of Vibrationally Excited Ozone Formed by Three-body Recombination, I, Spectroscopy," *J. Chem. Phys.*, **87**, 5202 (1987).
65. W. T. Rawlins, A. M. Woodward, and D. R. Smith, "Aeronomy of Infrared Ozone Fluorescence Measured During an Aurora by the SPIRIT 1 Rocketborne Interferometer," *J. Geophys. Res.*, **98**, 3677 (1993).
66. J. I. Steinfeld, S. M. Adler-Golden, and J. Gallagher, "Critical Survey of Data on the Spectroscopy and Kinetics of Ozone in the Mesosphere and Thermosphere," *J. Phys. Chem. Ref. Data*, **16**, 911 (1987).

67. J. A. Joens, J. B. Burkholder, and E. J. Bair, "Vibrational Relaxation in Ozone Recombination," *J. Chem. Phys.*, **76**, 5902 (1982).
68. W. T. Rawlins, "Chemistry of Vibrationally Excited Ozone in the Upper Atmosphere," *J. Geophys. Res.*, **90**, 12283 (1985).
69. S. M. Adler-Golden, J. Gruninger, and D. R. Smith, "Derivation of Atmospheric Atomic Oxygen and Hydrogen Profiles for Ozone ν_3 Band Emission," *J. Geophys. Res.*, **97**, 19509 (1992).
70. J. Menard, L. Doyonette, and F. Menard-Bourcin, "Vibrational Relaxation of Ozone in O_3-O_2 and O_3-N_2 Gas Mixtures from Infrared Double-Resonance Measurements in the 200-300 K Temperature Range," *J. Chem. Phys.*, **96**, 5773 (1992).
71. G. A. West, R. E. Weston, Jr., and G. W. Flynn, "Deactivation of Vibrationally Excited Ozone by $O(^3P)$ Atoms," *Chem. Phys. Lett.*, **42**, 488 (1976).
72. A. Barbe, C. Secroun, and P. Jouve, "Infrared Spectra of $^{16}O_3$ and $^{18}O_3$: Darling and Dennison Resonance and Anharmonic Potential Function of Ozone," *J. Molec. Spectrosc.*, **49**, 171 (1974).
73. D. Imre, "Reaction Dynamics Studied by Photoemission Spectroscopy," Ph.D. Thesis, Massachusetts Institute of Technology (1984); D. Imre, J. L. Kinsey, R. W. Field, and D. H. Katayama, "Spectroscopic Characterization of Repulsive Potential Energy Surfaces: Fluorescence Spectrum of Ozone," *J. Phys. Chem.*, **86**, 2564 (1982).
74. K. K. Lehmann, "Comment on 'High Lying Levels of Ozone via an Algebraic Approach'," *J. Phys. Chem.*, **88**, 1047 (1984).
75. M. Kellman, "Algebraic Resonance Dynamics of the Normal/Local Transition from Experimental Spectra of ABA Triatomics," *J. Chem. Phys.*, **83**, 3843 (1985).
76. R. D. Sharma, J. H. Brown, A. Berk, P. K. Acharya, J. Gruninger, J. W. Duff, and R. L. Sundberg, "User's Manual for SAMM, SHARC and MODTRAN Merged," PL-TR-96-2090 (1996). ADA310349
77. F. X. Kneizys, E. P. Shettle, L. W. Abreu, J. H. Chetwynd, Jr., G. P. Anderson, W. O. Gallery, J. E. A. Selby, and S. A. Clough, "Users Guide to LOWTRAN 7," AFGL-TR-88-0177 (1988). ADA206773
78. G. N. Plass, "Models for Spectral Band Absorption," *J. Opt. Soc. Am.*, **48**, 690 (1958).
79. R. M. Goody and Y. L. Yung, "Atmospheric Radiation: Theoretical Basis," 2nd ed., (New York, Oxford University Press, 1989).
80. W. M. Cornette, "Robust Algorithm for Correcting the Layer Problem in LOWTRAN," *Appl. Opt.*, **31**, 5767 (1992).
81. S. Adler-Golden, J. Vail, D. Smith, L. Jeong, and R. Sharma, "Initial Survey of Model-Data Comparisons for the CIRIS-1A Experiment," SSI-TR-241 (1994).
82. L. A. Strugala, R. D. Sears, J. E. Newt, and B. J. Herman, "Production of Statistically Nonstationary Stochastic Structure Realizations for Infrared Background Scene Simulations," *Optical Engineering*, **32**, 993, 1993.

83. J. H. Brown, "Synthetic 3-D Atmospheric Temperature Structure: A Model for Known Geophysical Power Spectra Using a Hybrid Autoregression and Fourier Technique," PL-TR-94-2150, May 1994. ADA289058.
84. J. H. Gruninger, R. L. Sundberg, and P. De, "A Model for Atmospheric Radiance Clutter with Applications to Advanced BMD Interceptor Scenarios," *Proceedings of the IRIS Meeting on Targets, Backgrounds, and Discrimination*, February 1994.
85. R. L. Sundberg, J. H. Gruninger, and J. H. Brown, "Infrared Radiance Fluctuations in the Upper Atmosphere," *SPIE Proceedings of the International Symposium on Optical Engineering in Aerospace Sensing*, **2223**, Orlando FL, April 1994.
86. G. H. Lindquist, H. Kwon, and A. R. Nagy, Jr., "Model for Atmospheric Clutter as Seen from a Satellite Platform," *Proceedings of the Infrared Technology Conference, SPIE*, **430**, 24 - 31, 1983.